UiT The Arctic University of Norway

Faculty of Science and Technology, Department of Geoscience

Palaeoceanographic and climate changes during the Holocene in Hinlopen Strait, northern Svalbard

Mehdi Hosseini

Master's thesis in Geology-GEO-3900- June 2023

1.Introduction

Abstract

This study investigates the paleoceanographic changes in the Hinlopen Strait, situated between Spitsbergen and Nordaustlandet, through a multi-proxy analysis of sediment core HH15-1280-GC (439 m water depth). Located near the Polar Front, this region is highly sensitive to even minor alterations in the ocean circulation and climate, which can be reconstructed from marine sediment records. The core was examined using a combination of foraminiferal and sedimentological parameters to elucidate the historical and pre-historical changes during the last 8000 years in the study area. This research aims to enhance our understanding of the region's paleoceanographic evolution and a better understanding of the factors controlling factors them.

Acknowledgements

I am profoundly grateful to my supervisor, Professor Tine Lander Rasmussen, and co-supervisor, PhD candidate Christine Joanne Lockwood-Ireland, for their invaluable guidance and unwavering support throughout the course of my Master Thesis. My passion for Paleoclimate reconstruction took root during the GEO-3111 (Reconstructing Quaternary Environments) course, where I first met Professor Tine L. Rasmussen, ultimately leading me to pursue this topic for my thesis.

My heartfelt appreciation goes out to the dedicated laboratory staff, particularly Karina Monsen, Trine Dahl, and Ingvild Hald. Their assistance with laboratory equipment and techniques played a crucial role in the successful completion of this project, and I am grateful for the time we spent working together in the lab.

A special thanks goes to my love, Sara, who has been a constant source of motivation and support throughout these two years. Your encouragement and assistance have been invaluable in helping me navigate the challenges of this academic journey.

Lastly, I would like to express my gratitude to my fellow students, friends, and family members for their constant encouragement and support throughout this academic journey. Your contributions have been instrumental in helping me achieve this significant milestone.

Table of Contents

1.Introduction

1. Introduction

1.1 Objectives

The Svalbard margin in the northern Barents Sea is a key area for the evolution of paleoceanography and the influx of Atlantic Water at greater depths from the last deglaciation to the present day (Hald and Vorren, 1987). This project aims to illuminate these topics by employing a multi-proxy approach, focusing on foraminiferal and sedimentological records derived from a marine sediment core, collected at a depth of 439 meters in the Hinlopen Strait. To reconstruct the paleoceanographic shifts in the study area over time, we will examine an array of proxies, encompassing concentration of benthic and planktonic foraminifera, ice-rafted debris (IRD), magnetic susceptibility, XRD imaging, grain size distribution and distribution of dominant benthic foraminiferal species, AMS-^{14}C dates, stable isotopes (^{18}O and ^{13}C), sortable silt, and other sedimentological data. Through the analysis of these data, we aim to enhance our understanding of the paleoceanographic variations in the region.

Additionally, we intend to correlate our findings with data from other studies to provide a broader regional perspective. This method will enable us to construct a comprehensive picture of the Hinlopen Strait's paleoceanographic history, its connections to larger climatic shifts, and ocean circulation patterns. Ultimately, this project aspires to contribute to the understanding of the Hinlopen shelf's paleoceanographic history and its significance within the broader context of the Nordic seas' evolution during the Holocene period.

1.2 Background

The Holocene period, spanning from around 11.700 years ago to the present day (Walker et al., 2009), represents a critical period in Earth's history marked by the end of the last ice age and the establishment of modern climatic and oceanographic conditions. The study of paleoceanographic changes during this period provides valuable insights into the complex interplay between climate, ocean circulation, and their impacts on marine ecosystems. The Hinlopen Strait, situated between Spitsbergen and Nordaustlandet in the Svalbard archipelago, offers a unique opportunity to investigate the paleoceanographic history of the region due to its sensitivity to environmental changes (Ślubowska et al., 2005; Bartels et al., 2018).

The Hinlopen Strait is located in the Arctic region, where the inflow of warm Atlantic Water and cold Arctic Water influences the local and regional climate, ocean circulation patterns, and marine ecosystems (Fig 1). This area is particularly important for understanding the evolution of paleoceanography and the Atlantic Water influx at subsurface depths during the Holocene

period. The proximity of the Hinlopen Strait to the Polar Front (Fig 1) makes it an ideal location to study the impact of even minor shifts in the current system and their corresponding signals in paleoceanographic parameters.

Recent environmental changes in the Arctic, such as rapid sea ice decline and increasing temperatures, have highlighted the urgency of understanding the region's natural variability to better predict and prepare for future changes. Investigating the paleoceanographic history of the Arctic helps contextualize these recent changes and provides insights into the potential consequences of continued environmental shifts.

Previous research in the Nordic Seas has focused on the reconstruction of paleoceanographic conditions during the Holocene, utilizing various proxies such as foraminiferal and sedimentological records, magnetic susceptibility and other data and proxies (Hald and Vorren, 1987; Jennings et al., 2002; Mangerud et al., 2004; Ślubowska et al., 2005; Ślubowska-Woldengen et al., 2008). These studies have significantly contributed to our understanding of the region's paleoceanographic history, including its connections to larger climatic shifts and ocean circulation patterns.

Rasmussen and colleagues have conducted several studies that have shed light on the paleoceanographic changes in the Nordic Seas during the Holocene. For instance, Rasmussen et al. (2007) analyzed the paleoceanographic evolution of the southwestern Svalbard margin since 20.000 ^{14}C years BP, providing valuable insights into the region's climatic and oceanographic history. Furthermore, Kristensen et al. (2013) investigated the oceanographic changes in the Nordic Seas during the last deglaciation, highlighting the intricate relationship between climate and ocean circulation in the region.

2. Geological and oceanographical setting

2.1 Geological setting

The Svalbard Archipelago is a group of islands situated in the high Arctic, spanning from 76° to 81°N (Fig 1). Despite its northern location, the archipelago's climate is affected by the West Spitsbergen Current (WSC), the northernmost extension of the North Atlantic Current. The WSC's influence on climatic conditions over the western coast of the high-latitude archipelago is apparent, with an average annual winter temperature of minus 12°C and an average July temperature of 5°C (Hisdal, 1998).

Currently, sixty percent of the Svalbard archipelago is covered by glaciers and ice caps, including a significant portion of Svalbard (Ślubowska et al., 2005). The presence of these ice formations can significantly impact the marine environment by influencing ocean currents, sea levels, and sedimentation patterns. As such, studying the geological setting of the Svalbard region is essential to understand the area's paleoceanography.

The Hinlopen Strait, which separates the largest island in the archipelago, Spitsbergen, from Nordaustlandet Island, is a crucial component of the region's geological setting. This strait is approximately 170 km long and is characterized by strong tidal currents that flow along its axis in a northerly direction with the rising tide and a southerly direction with the falling tide. At the northern mouth of the strait lies the Hinlopen Trough, a 400-meter-deep depression that extends north to the edge of the shelf (Ślubowska et al., 2005).

The depression formed by the Hinlopen Strait and the trough extending northwards from it creates a distinct topographical feature on the middle and outer shelf of Svalbard. Additionally, the Hinlopen Strait is flanked by the ice cap of Nordaustlandet, and many glaciers on land calve into the strait, further contributing to its unique characteristics. These features can influence ocean currents and sedimentation patterns, making them crucial aspects of the region's geological setting. Understanding the topographical features of the Svalbard region, including the influence of ice caps and glaciers, is essential to accurately reconstruct the area's paleoceanography.

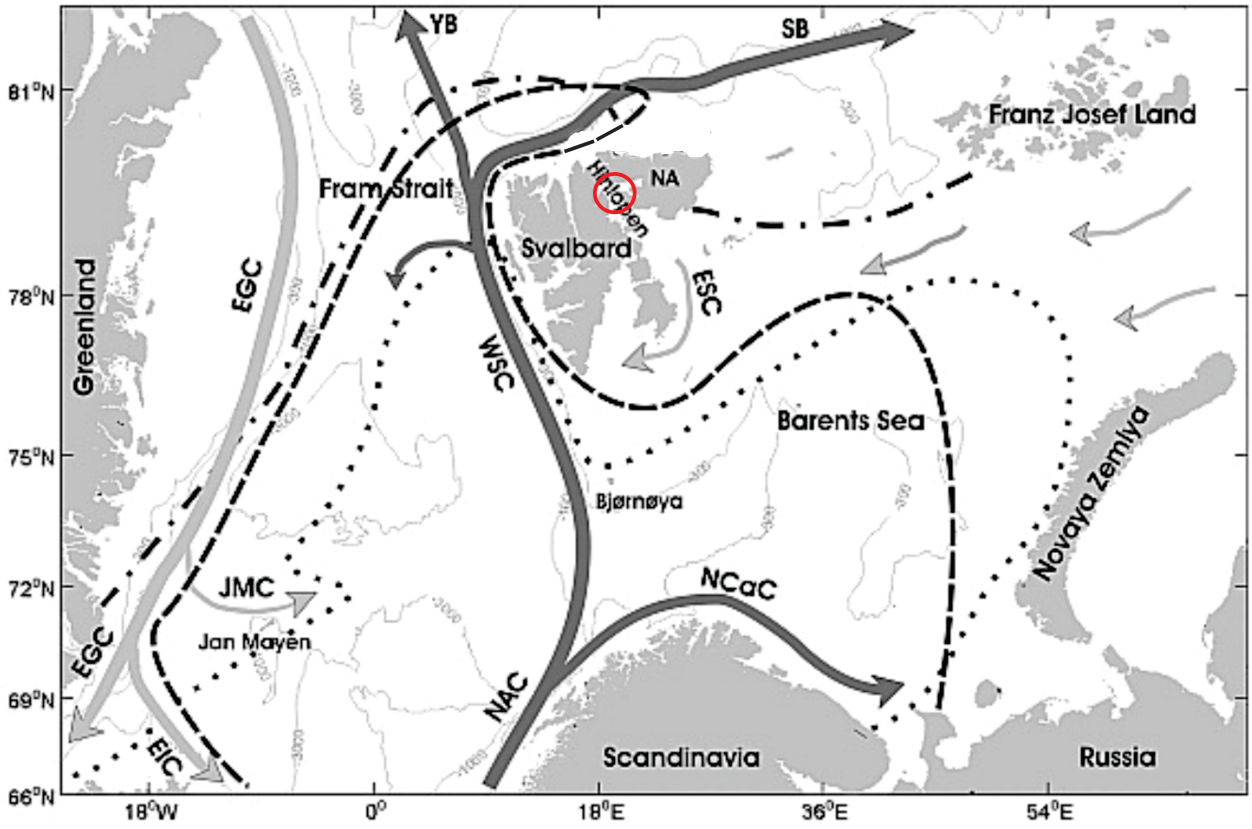

Figure 1: Location of the core HH15-1280-GC core site and the main current system in the area. Polar Front (dashed line), average winter (dotted line), and summer sea ice margin (dashed-dotted line) modified from Vinje (1977). Warm currents are represented by dark grey, while cold currents are denoted by light grey. Abbreviations are NAC, North Atlantic Current, WSC, West Spitsbergen Current; ESC, East Spitsbergen Current; EGC, East Greenland Current; NCaC, North Cape Current; EIC, East Iceland Current; JMC, Jan Mayen Current; SB, Svalbard Branch; YB, Yermak Branch; and NA, Nordaustlandet.

2.2 Oceanography

The oceanography of the Northern Svalbard shelf is influenced by various water masses, including the Arctic Water, the Atlantic water, and the Polar Water. The inflow of Atlantic Water into the Nordic Seas plays a crucial role in the region's oceanography, as it is responsible for transporting heat and salt into the region, influencing the water column structure and circulation patterns (Skagseth et al., 2008).

The inflow of warm and saline Atlantic water to the Northern Svalbard shelf occurs via the West Spitsbergen Current (WSC), which flows northward along the western coast of Svalbard (Fig 1). The WSC divides into two branches north of Svalbard, the Svalbard branch and the Yermak branch. The Svalbard branch flows northeastward along the shelf break, while the Yermak branch flows northward along the continental slope.

The Atlantic Water inflow is also affected by the Polar Front, which separates the Arctic Water from the Atlantic Water. The position of the Polar Front is influenced by various factors, including atmospheric forcing and ocean circulation patterns, and can vary seasonally and interannually (Skagseth et al., 2008). The Polar Water is the least saline and coldest water mass in the region, originating from the Arctic Ocean and the Barents Sea.

In the CTD profile collected from Hinlopen, HH15-1279-CTD station (79.49.832 °N and 018.08.061 °E), several distinct water layers can be observed (Fig 2). The depth range of 70 to 200 meters is characterized by a high salinity of 35 PSU, indicative of the presence of Atlantic Water (AW) in this region (Rudels et al., 2015). The temperature within this layer is also elevated, exceeding 3°C, which is consistent with the known temperature range of AW (Carmack et al., 2015).

Below 200 meters, the salinity remains relatively stable at approximately 34.8 PSU, and the temperature gradually decreases to around 1.5°C towards the bottom. This layer can be identified as Modified Atlantic Water (MAW) due to its lower salinity and colder temperature compared to the AW above (Rudels et al., 2015). MAW is formed as AW undergoes modifications due to cooling and dilution as it moves further into the Arctic Ocean and mixes with other water masses.

The density profile shows an increase from approximately 27 kg/m³ at the surface to around 28 kg/m³ at depths below 30 meters, which is consistent with the presence of a halocline separating the relatively fresher Polar Surface Water (PSW) from the underlying AW (Aagaard et al., 1981; Rudels et al., 2015). In the upper layer, between 0 and 70 meters, the salinity ranges from 34 to 34.5 PSU and the temperature varies from 5.5 to 1.8°C, suggesting a mixture of AW and PSW. This mixture could result from oceanographic processes such as advection, vertical mixing, or upwelling, causing the warmer, saltier AW to mix with the colder, fresher PSW near the surface.

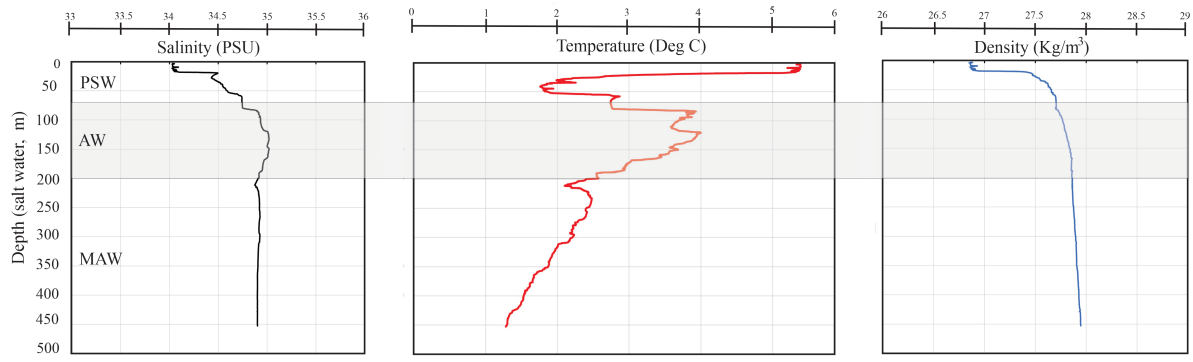

Figure 2: CTD profile from Hinlopen, HH15-1279-CTD station, highlighting the distinct water layers: warm and high-salinity Atlantic Water (70-200 m), colder and less saline Modified Atlantic Water (MAW) (>200 m), and fresher Polar Surface Water (PSW). Density gradient indicates the halocline separating the water masses.

2.3 Glacial history

The Barents Sea has experienced multiple cycles of glaciation during the late Cenozoic, with the most extensive glaciations occurring during the Quaternary period. These glacial events have had a significant impact on the geological history of the region, shaping the landscape and influencing sedimentation patterns.

During the peak of the last glacial maximum (LGM), approximately 21.000 years ago, the Barents Sea was covered by an ice sheet that extended from the Fennoscandian ice sheet, across the Arctic Ocean, and into North America. The margin of the ice sheet extended to the shelf edge, and the continental shelf and slope acted as a depocenter, receiving vast quantities of sediment eroded from the surrounding landmasses (Vorren et al., 1988).

As the ice sheet retreated during the subsequent interglacial period, sedimentation rates in the Barents Sea decreased dramatically. The region transformed into a nutrient-poor continental margin, characterized by low primary productivity and sedimentation rates (Vorren et al., 1988).

The glacial history of the Barents Sea has been reconstructed using a variety of methods, including sediment core analysis, seismic profiling, and numerical modeling. These studies have provided important insights into the timing and extent of glaciation events in the region, as well as their impact on sedimentation patterns and ocean circulation.

For example, a study by Svendsen et al. (2004) used sediment core analysis to reconstruct the environmental history of the Barents Sea over the past 130.000 years. The results of this study

revealed that the region experienced several episodes of glaciation during this period, with the most significant events occurring during the Last Glacial Maximum (20000-18000 years, Svendsen et al., 2004; Clark et al., 2009) and the preceding Marine Isotope Stage 4 (approximately 71000 to 57000 years ago; Siddall et al., 2003)

Another study by Rebesco et al. (2010) used high-resolution seismic profiling to investigate the glacial history of the northern Barents Sea. The results of this study indicated that the continental shelf and slope acted as a major depocenter during glaciation events, with large quantities of sediment being deposited in the region.

2.3.1 Late Glacial Maximum (LGM)

The Late Weichselian maximum, also known as the Last Glacial Maximum (LGM), had a significant impact on the Barents Sea's glacial history. During this period, the entire Barents Sea continental shelf, from its edge to its center, was covered by an ice sheet (Vorren et al., 2011). The ice sheet's margin extended beyond the present-day coastline, and it was characterized by rapid sediment deposition and erosion, which contributed to the formation of a large depocenter on the shelf (Hass et al., 2008).

The Bear Island Ice Stream, which was one of the primary outlets for the melting ice during the LGM, received its supply from vast northern and southern aquifers (Vorren et al., 2011). This ice stream was formed by the union of two major ice streams. One of these originated in the east and entered the White Sea through Kandalaksa Gulf. However, it is still unclear whether the ice flowed directly southeast or curved and fed the Bear Island Ice Stream (Vorren et al., 2011).

The LGM had a significant impact on the margin of the Barents Sea's sedimentation rate. During this period, sedimentation rates were high due to the rapid deposition of glacially eroded material on the continental shelf. However, during interglacial periods, the sedimentation rate dropped dramatically, transforming the Barents Sea into a nutrient-starved continental margin (Vorren et al., 1988).

2.3.2 Deglacial

During the deglaciation phase in the southern Barents Sea, the ice margin started retreating, and the glacial morphology showed both spatial and temporal variations in ice dynamics. There was evidence of active ice streaming and frozen-bed conditions during the Late Weichselian glaciation in the southern Barents Sea (Rebesco et al., 2010). The grounding zone wedge of

Bear Island was mapped to record phases of retreat and subsequent advance of the ice stream (Rebesco et al., 2010). Distinct ice stream patterns and dynamics were observed during the deglaciation in the Barents Sea and were categorized into three flow events (Dowdeswell et al., 2008). The first phase coincided with the peak of the Late Weichselian glaciation. At its furthest point, the ice sheet reached the shelf edge, which was the primary outlet for the Bear Island ice stream (Andreassen and Winsborrow, 2009; Rebesco et al., 2010). The most recent flow event, which ended 100 km from the shelf edge, is interpreted to have occurred at 16.000 yr. BP and represents an early readvance during the deglaciation (Andreassen et al., 2008).

2.3.3 Holocene

The Holocene period, spanning from approximately 11.700 years ago to the present day, has been a period of significant climate variability in the Barents Sea region. During the early Holocene (9.5–7.5 kyr), warm and salty Atlantic water had a strong significant influence on the Barents Sea. Foraminifera from the Arctic disappeared from the northern Nordic Seas, and ice-rafted debris (IRD) counts were low in the Barents Sea, East Greenland, and the Nordic Seas (Ślubowska-Woldengen et al., 2008). Dinocyst distribution in sediment cores from the southwestern Barents Sea also supports the idea that the early Holocene climate was both warm and stable (Kunz-Pirrung et al., 2001). However, a temporary cold interval (8.2-8.1 kyr BP), caused by a "8.2 ka" cooling event, was associated with an increase in sea ice, a salinity anomaly, and a decrease in methane concentrations and the North Atlantic thermohaline circulation (Alley et al., 1997; Alley, 2007).

Around 7.5 ka BP, the Arctic Front began to advance southward, signaling a reduction in the Atlantic Ocean's impact on global climate (Ślubowska-Woldengen et al., 2008). In the southeastern Barents Sea, sea-ice cover has fluctuated multiple times over the past century, as documented by Kunz-Pirrung et al. (2001). Neoglaciation began around 4 ka BP and lasted until 2 ka BP (Rasmussen et al., 2014). Benthic foraminifera have indicated a worsening climate and a decrease in the flux of Atlantic water relative to the early Holocene (Ślubowska-Woldengen et al., 2008). The shelf bottom waters cooled and became fresher, while sea ice coverage increased. Concurrently, iceberg rafting increased, possibly as a result of glacier re-advances on Svalbard and Greenland (Hormes et al., 2013).

Since 2.5 ka BP until the present day, the Barents Sea region has experienced unstable conditions characterized by reduced surface and subsurface water salinity, high IRD deposition, and stronger stratification of the water column than at present. The southwestern Barents Sea

was influenced by more coastal water and experienced colder conditions (Risebrobakken et al., 2010). This period also encompasses several significant climate events, such as the Roman Warm Period (RWP), Dark Ages Cold Period (DACP), Medieval Warm Period (MWP), and Little Ice Age (LIA).

The RWP (2200 to 1600 years BP) was characterized by a relatively warm and stable climate in many regions (Mann et al., 2009). Following the DACP (1500 to 1000 years BP) saw a decline in temperatures and increased climatic variability (Helama et al., 2017). The MWP (ca. 1000 to 700 years BP) was a time of relatively warm climate in many parts of the world, including Europe and the North Atlantic (Mann et al., 2009). Lastly, the LIA (ca. 700 to 150 years BP) was marked by a significant drop in temperatures, leading to widespread glacial advances and more extensive sea ice coverage in the Barents Sea (Miller et al., 2012).

2. Geological and Oceanographical setting

3. Material and Methods

3.1 Sediment cores

Sediment core HH15-1280-GC, which was collected from the Hinlopen Strait between Spitsbergen and Nordaustlandet (79.48.113 °N and 018.08.560 °E, water depth 439 m, Figure 3) during a marine geology and geophysics cruise from July 23rd to August 3rd, with RV Helmer Hanssen. The core has a total length of 526 cm.

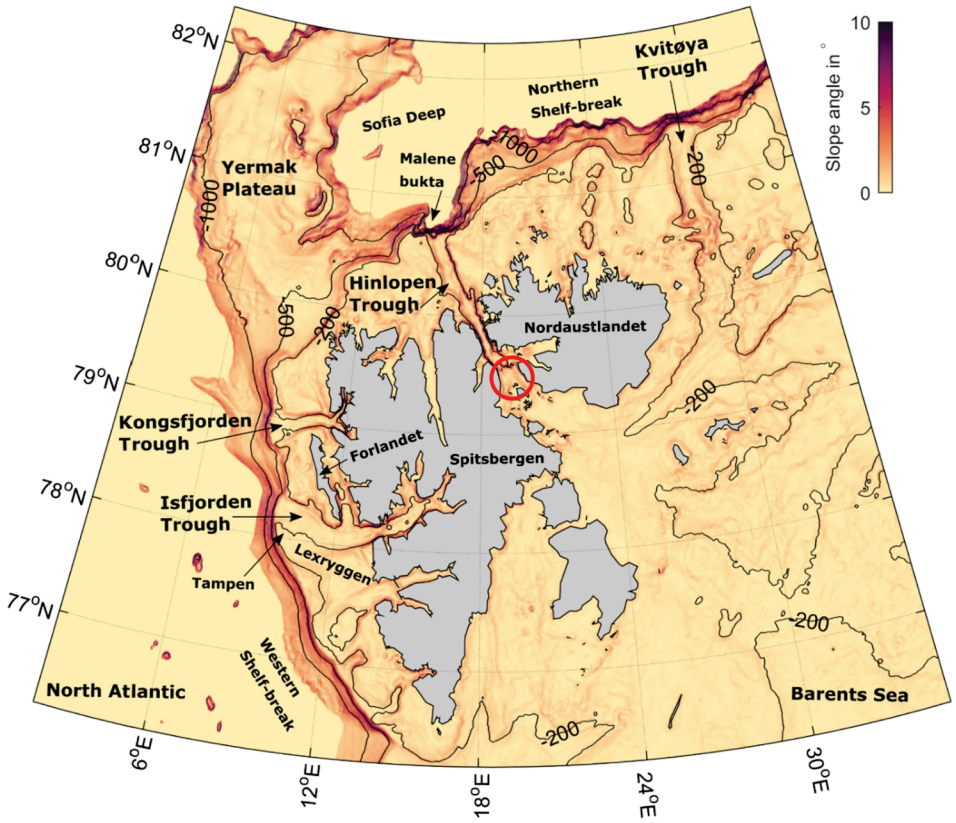

Figure 3: Map showing location of core HH15-1280-GC, modified from Menze et al. (2020).

3.2 Gravity coring and core processing

The sediment core was extracted using a gravity corer, which can collect sediments up to 6 meters in length and can be used in water depths of up to 3 kilometers. The gravity corer is lowered to the ocean floor and penetrates the seafloor to retrieve sediments by gravity. There is lined inside by an inner plastic core liner. The core cutter, located at the end of the gravity corer, is used for easier penetration of the sediments. The orange peel core catcher ensures that the sediments remain contained inside the core liner. Once the sediments were retrieved the

core liner was taken out, cleaned, measured, and labeled. It was then cut into one-meter sections, and the sediments were collected from the core catcher and core cutter if any. The sediment samples were cataloged and labeled for further analysis.

3.3 Laboratory Works

The Department of Geology at the University of Tromsø, the Arctic University of Norway, served as the site for laboratory work. Radiocarbon dating was performed at the renowned 14Chrone Center, based at Queen's University in Belfast, Northern Ireland. Samples, including those examined for $^{13}C/^{12}C$ and $^{18}O/^{16}O$, were transported to the University of Tromsø Geological Mass Spectrometer Laboratory, where they were analyzed to provide further insight into the carbon and oxygen isotopes. The grain size distribution of the sediment samples was determined using a Beckman Coulter LS 13 320 Particle Size Analyzer in department of geology at the university of Tromsø. By integrating these techniques and expertise from various institutions, the project offers a comprehensive and nuanced understanding of the paleoclimate and paleoceanography during Holocene in Hinlopen Strait.

3.3.1 GEOTEK Multisensor Core Logger

At the Geology laboratory of UiT, the GEOTEK Multisensor Core Logger was employed to measure the length of the open core, and record magnetic susceptibility and color scale per centimeter. The archive half of the core was utilized for this measurement, given that the work half of the core was sampled for this study.To prevent any surface reflections from affecting the data, the core was removed from the cooling chamber 24 hours before the logging process to allow it to reach room temperature. Prior to logging, plastic cards were used to clean the surface of each section. A point sensor was employed to assess the magnetic susceptibility of the core, while the colors were recorded in various formats, including Munsell, CIE, and spectrophotometer reflectance values.

3.3.1.1 Magnetic Susceptibility

Magnetic susceptibility (MS) is a fundamental property of materials that describes their degree of magnetization under an applied magnetic field. The GEOTEK Multisensor Core Logger's Bartington loop sensor (MS2C) generates down-core profiles of magnetic susceptibility at 1 cm intervals by providing a magnetic field to the sediment core sections as they travel through the

logger. Materials that are paramagnetic, ferromagnetic, ferrimagnetic, or antiferromagnetic will produce a positive MS reading and enhance the magnetic field, while diamagnetic materials will give a negative reading and weaken the field. This approach provides a powerful tool for stratigraphic analysis, allowing for the identification of events in the sedimentary record and detecting changes in lithology linked to shifts in provenance of the material.

3.3.2 Avaatech XRF Core Scanner

The Avaatech XRF core scanner is a tool used to obtain high-resolution color images of sediment cores for this study. The scanner operates by utilizing X-ray fluorescence (XRF) to generate images (Fig 5). The core is removed from the cooling chamber 24 hours before scanning, and the surface is cleaned to ensure accurate readings. The scanner captures images of the core's composition, displaying variations in color and texture that can reveal information about the sedimentary environment and processes that produced the core.

3.3.3 GEOTEK X-ray Core-imaging system

The GEOTEK X-ray core-imaging technology was used to acquire grayscale X-ray pictures of the six core sections (Fig 6). The core was prepared in the same manner as for the XRF core scanner; that is, it was brought to room temperature, and its surface was cleaned. The grey scale of the pictures correspond to the core's density, and the images may be utilized to assess various sedimentary features, lithological facies, and physical and biological structures (Migeon et al., 1998).

3.3.4 Sedimentology

After the core sections were collected, a circular saw was used to cut the core portions along the long axis. The plastic liner was cut with a spatula and a small wire to separate the sediment in the core portions of the archive and work half. The archive parts were wrapped and kept refrigerated in a 4°C storage facility for further analysis. The sediment surface of the working section was cleaned, and visually described, taking note of observable changes in grain size, clast distribution, sedimentary structure, and layer boundaries. The Munsell Soil Color Chart was used to determine the color of the sediment.

Lithological logs were created in Corel Draw. The lithological logs were essential in describing the vertical variation of the sediments, highlighting the changes in sedimentary facies and providing a visual representation of the core's stratigraphy.

In addition, the use of X-radiography in sedimentology helped detect structures, clasts, and fossils that would otherwise be difficult to recognize. By combining and employing X-radiography, sedimentologists were able to identify sedimentary features such as crossbedding, laminations, and bioturbation, as well as clasts and fossils that are present in the core sections are easier to identify.

3.3.4.1 Sedimentology Sampling

The work half of the core sections were sliced into 1-cm thick slices throughout the whole length of the core (526 samples) and placed in pre-weighed and labeled plastic bags. To prevent any contamination, the sediment surrounding the core liner was avoided during sampling. The samples were all wet weighed and subsequently frozen.

3.3.4.2 Freeze drying technique

In the Geology Department Laboratory, UiT, the Arctic University Norway, Tromsø, the sediments were subjected to freeze-drying to remove any remaining moisture. The freeze-drying technique involves freezing the samples and creating a vacuum that allows the frozen water in the sediments to sublimate from the solid phase to the gas phase. This process can take up to 24 hours, depending on the water content of the sediment samples. After freeze-drying, the dry samples were weighed, and the water content of each sediment sample was determined.

3.3.4.3 Sieving

To obtain sediment grain size distribution, wet sieving was performed on freeze-dried sediment samples at every 10 cm. The samples were sieved through three sieves of mesh sizes of 63 µm, 100 µm, and 500 µm. The residue from each sieve was transferred onto labeled filter sheets using distilled water to prevent contamination between samples. The sieves were cleaned in a Grant XB14 ultrasonic bath after each sample. The residues were then dried in a 40 °C oven until completely dry, and the dry weight was recorded. The dry residues were stored in labeled glass jars.

Grain size distribution is an essential parameter for understanding sediment transport and deposition processes. The wet sieving method used in this study allows for the determination of particle sizes between 63 µm and 500 µm, which is crucial for identifying sedimentary environments and depositional processes. The choice of mesh sizes used in the sieving process was based on the sediment size distribution and the research objectives.

In addition to sieving, other techniques such as laser diffraction and sedimentation analysis can also be used to determine grain size distribution.

3.3.4.4 Grain size evaluation

In order to evaluate the grain size of the sediment samples, the total dry sediment weight and the weight of each residue size (63-100 µm, 100-500 µm, and >500 µm) were measured. The percentages of the various residue sizes in each sediment sample were calculated using the following formulae:

$$\%\ 63\text{-}\ 100\ \mu m = \frac{\text{weight of } 63 - 100\ \mu m \text{ residue}}{\text{total dry weight of sediment sample}} * 100\%$$

$$\%\ 100\text{-}\ 500\ \mu m = \frac{\text{weight of } 100 - 500\ \mu m \text{ residue}}{\text{total dry weight of sediment sample}} * 100\%$$

$$\%\ > 500\ \mu m = \frac{\text{weight of } > 500\ \mu m \text{ residue}}{\text{total dry weight of sediment sample}} * 100\%$$

In addition to these three categories, the weight of sediment samples with a grain size smaller than 63 µm was also calculated as the total dry weight of sediment sample minus the weight of the < 63 µm residue. These calculations were carried out to determine the distribution of sediment grain sizes in each sample.

$$\%\ < 63\ \mu m = \frac{\text{weight of } < 63\mu m \text{ residue}}{\text{total dry weight of sediment sample}} * 100\%$$

3.3.4.5 Water content

The water content (in %) of each sediment sample was calculated by subtracting the dry sediment weight from the wet sediment weight, dividing the result by the wet sediment weight, and multiplying by 100%. The formula is as follows:

$$\text{Water content} = \frac{\text{wet sediment weight} - \text{dry sediment weight}}{\text{wet sediment weight}} * 100\%$$

$$= \frac{\text{Water weight}}{\text{wet sediment weight}} * 100\%$$

3.3.5 Sortable silt

The sortable silt proxy is a widely employed method for estimating past bottom current strength by analyzing the concentration of sortable silt in sediment samples. This proxy aids in understanding the movement and deposition of silt-sized particles, thereby helping researchers decipher sedimentary processes and current strength (McCave et al., 1995). By examining the sortable silt fraction (particles ranging in size from 10-63 μm), researchers can obtain information about the origins and pathways of sediment transport, as well as the depositional conditions and temporal variations.

The test begins by adding 20 % hydrochloric acid or acetic acid to a test tube containing more than 2 grams of dry sediment, followed by 24 hours of incubation in a fume hood. The acid dissolves any organic substances in the sample, making separation of the appropriate particle size range easier. After centrifuging the sample, the excess liquid is decanted. Next, 20 % hydrogen peroxide is added to the test tube, and the sample is heated in a thermal bath at 85 °C for 2 hours. The sample is centrifuged again after heating, and the excess liquid is decanted. To remove all moisture, the sample is either freeze-dried or dried in a fume hood.

The required amount of sample (usually 0.2-0.5 gram, depending on particle size) is then placed in a beaker with 20 ml of distilled water and 1-2 drops of Calgon and shaken for at least a day on a shaking table. Calgon is added to prevent particle clumping, resulting in more accurate

analysis. Finally, the sample is analyzed using a Beckman Coulter LS 13 320 Particle Size Analyzer, which uses laser diffraction to determine the particle size distribution in the sample. The analyzer may have pre-programmed parameters for the desired analysis, such as the particle concentration in the 10-63 μm range, which is a typical size range for sortable silt.

3.3.6 Foraminiferal examination

Foraminifera are single-celled organisms with shells made of calcium carbonate or agglutinated particles that can be found in marine sediments. They are useful for paleoceanographic and paleoclimatic reconstructions because their assemblages provide information about past environmental conditions. In this study, the distribution of foraminifera was determined using the 100-500 μm size fraction from core HH15-1280-GC to make the results comparable to other studies from the same location, and because Arctic foraminifera are often smaller in size than those from warmer waters.

Samples were evenly dispersed on a picking tray consisting of 45 squares and examined using a binocular microscope. Benthic foraminifera were counted in every sample at 10 cm intervals, with planktonic foraminifera disregarded due to their low numbers. Random squares were chosen for counting, and around 300 individuals of benthic foraminifera were counted and identified to species level. The number c. 300 was obtained to ensure accurate statistical comparability within and across populations and samples. Contamination was prevented and minimized by thoroughly cleaning the equipment with compressed air between samples.

To estimate the number of foraminifera per gram of sediment, the quantity of material on the tray was weighed for subsequent calculations. The density (number of specimens per gram dry weight sediment) and flux of foraminifera were also estimated to provide concentration data and productivity. If a sample lacked enough specimens, more than one tray was tallied to identify a sufficient number of specimens. To calculate the density the first the number of foraminifera on tray was be calculated using the following equation:

$$= \frac{\mathrm{n}umber\ of\ forams\ counted * 45\ (number\ of\ squares)}{counted\ squares * 1/2}$$

Number of foraminifera in sample:

$$= \frac{\text{Number of foraminifera on tray}}{Weight\ of\ residue\ on\ tray} * \text{weight of } 100 - 500\ \mu\text{m}$$

$$= \frac{\text{Number of foraminifera in sample}}{total\ dry\ weight\ of\ sample}\ (\frac{no}{g})$$

3.3.7 IRD Counts

In this study, the ice-rafted debris (IRD) was counted in all samples using two methods. The first method involved counting particles larger than 500 µm after sieving, while the second method used the IRD > 250 µm from the sortable silt analyses. The IRD consists of mineral and sedimentary rocks carried by icebergs and deposited in marine sediments as the icebergs melt. The number of IRD > 500 µm grains per gram dry weight sediment was determined by dividing the number of IRD_s counted (all was counted) by the total dry weight of the sediment sample. This count serves as an essential parameter for studying past ice sheet dynamics and changes in ocean currents.

$$= \frac{\text{Number of IRD counted}}{total\ dry\ weight\ of\ sample}\ (\frac{no}{g})$$

3.3.8 Radiocarbon dating

3.3.8.1 Principle

Radiocarbon dating is a widely used method to estimate the ages of elements that are less than 50000 years old. It is based on measuring the decay of the radioactive isotope carbon-14 (^{14}C) in organic materials. Carbon naturally occurs in three isotopes, including ^{12}C, ^{13}C, and ^{14}C, which have the same atomic number but different atomic weights. While ^{12}C and ^{13}C are stable isotopes, ^{14}C is unstable and radioactive. Unlike the other isotopes, ^{14}C is created in the high atmosphere as a result of nuclear processes involving free neutrons hitting other atoms and molecules, primarily ^{14}N atoms. The isotope is rapidly oxidized to CO_2 molecules, which are then dispersed throughout the atmosphere and absorbed by the oceans. Through the carbon

cycle, the absorbed CO_2 enters plant material through photosynthesis and becomes a component of calcareous ($CaCO^3$) marine creatures.

While the organism is alive, it maintains a balance with the environment, and the ^{14}C levels in its tissues are consistent with the ^{14}C levels in the atmosphere or water mass. However, when the organism dies, it stops absorbing ambient CO_2, and the ^{14}C continues to decay but is not replenished. The isotope has a half-life of 5570 ± 30 years, and the age of the organic material can be estimated by comparing the amount of unstable ^{14}C remaining with that of a standard known ^{14}C level (Bowman, 1990; Lowe and Walker, 2015).

This dating approach is based on several assumptions, including that the generation of ^{14}C in the atmosphere has remained constant throughout time, the ^{14}C concentration is the same throughout the system, and the half-life of ^{14}C is known with reasonable accuracy and has remained constant since the organism's demise. It is essential to consider these assumptions since they can be sources of error when analyzing ^{14}C ages (Faure and Mensing, 2005).

3.3.8.2 AMS radiocarbon dating

In this study, AMS radiocarbon dating was used to determine the age of sediment samples containing the benthic foraminiferal species *Nonionellina labradorica*. The samples were radiocarbon dated at separate intervals to indicate a broad age spread in the core. The intervals were chosen primarily because there was a significant quantity of material. Only well-preserved specimens with no sediment fill of *N. labradorica* with no evidence of damage were collected to prevent contamination via re-deposition.

Two samples from core HH15-1280-GC were sent to the 14CHRONO Centre at Queen's University in Belfast, Northern Ireland, for AMS ^{14}C dating. AMS (Accelerator Mass Spectrometry) is a highly sensitive method for radiocarbon dating that uses a particle accelerator to measure the concentration of isotopes. In this case, the concentration of ^{14}C isotopes in the samples was measured to determine their age. Table 1 shows the information of the samples which were chosen for AMS radiocarbon dating. The resulting dates were used to construct an age-depth model for the core, which was used to determine the timing of paleoceanographic events such as sea-ice extent changes and iceberg discharge events.

UB_No	Sample_Type	Material_Type	Sample_Weight	sample_id	Contaminants	customer_po	site_name	Comment	Excess_Returned
49738	shell or other carbonates	foraminifera	14.5	HH15-1280GC, 80.5 cm		600025251		careful pre-treatment	
49739	shell or other carbonates	foraminifera	22	HH15-1280GC, 430.5cm		600025251		careful pre-treatment	

Table 1: AMS radiocarbon dating data for sediment samples containing *N. labradorica*.

3.3.8.3 Chronology and construction of age model

The age model for the HH15-1280-GC sediment core was constructed using two AMS radiocarbon dates from the benthic foraminiferal species *N. labradorica*. These dates were calibrated into calibrated calendar years before present (cal yr. BP) using the IntCal13 and the Marine13 calibration curve. The resulting chronology covers a time span from approximately 8000 cal yr. BP to the present (Table 2).

The construction of an accurate age model is crucial for interpreting the changes and events observed in sediment cores. It allows for the linking of various datasets, such as changes in sediment composition, environmental conditions, and biological communities, with specific time periods.

The use of benthic foraminifera for dating sediment cores is particularly useful in regions were other dating methods, such as varve counting or dendrochronology, may not be applicable.

Lab code	Dated material	Depth cm	Sample weight mg	Radiocarbon age	Cal. Yr BP 1sigma range	Cal. Yr BP 1sigma mean	Cal. Yr BP 2sigma range	Cal. Yr BP 2sigma mean
49738	N. labradorica	80.5	14.5	1745 ± 25	1074-1217	1145.5	1003-1273	1138
49739	N. labradorica	430.5	22.1	6139 ± 28	6291-6434	6362.5	6223-6524	6373.5

Table 2: AMS radiocarbon dating results for *N. labradorica*-containing samples (1145.5-6362.5 cal years BP)

3.3.8.4 Marine reservoir effect and calibration

The concentration of ^{14}C in animals and plants is influenced by a variety of variables, including radioactive decay. Factors such as variations in the production of ^{14}C in the atmosphere caused by oscillations in the earth's magnetic field and sunspot activity, natural changes caused by glaciations and human activities such as fossil-fuel combustion, known as the Suess effect, and

nuclear-weapons testing (Bowman, 1990). As a result, calibration between radiocarbon years and calendar years before present is required (calendar years before present: cal yr. BP).

At the ocean-atmosphere interface, radiocarbon is absorbed into the ocean. Subsurface and deep ocean mixing rates are sluggish. Therefore, a more isolated layer of deeper water forms, with less compensation for ^{14}C degradation due to insufficient mixing with fresh surface waters. This reduced quantity of ^{14}C is incorporated by marine animals that use carbon to produce tests and shells (Bowman, 1990). This results in an apparent older radiocarbon age, which is known as the marine reservoir effect R(t), which fluctuates over time and is defined as the difference between the ^{14}C age of samples produced in the sea and the ^{14}C age of those grown in the atmosphere concurrently (Stuiver et al., 1986). To compare a marine organism's radiocarbon age to ice-core and terrestrial data, it is necessary to account for the marine reservoir effect (Bondevik et al., 2006).

Local and lateral changes in water masses must also be considered (Bowman, 1990; Mangerud et al., 2006), and a regional offset from a global mean reservoir age R(t) is known as ΔR. (Stuiver et al., 1986). Variations in sea-ice cover, wind speed, and upwelling of poorly ventilated subsurface waters cause regional differences.

3.3.9 Stable isotope analysis ($\delta^{18}O$ and $\delta^{13}C$)

3.3.9.1 Principle

Stable isotope studies of foraminiferal carbon tests have supplied much of the information and framework for reconstructions of past ocean and climatic conditions (Loubere, 1991). Variations in carbon and oxygen isotope ratios (^{18}O and ^{13}C) in foraminiferal tests show numerous geochemical features of the ambient sea water masses in which they have been calcified. More specifically, temperature and salinity changes control ^{18}O, whereas ^{13}C reflects the primary production and stratification characteristics (ventilation) of the water mass (Spielhagen and Erlenkeuser, 1994) and thus provide a foundation for the reconstruction of oceanographically change in water masses and ocean circulation. Planktic foraminifera give information about the surface ocean, while benthic foraminifera provide information on bottom conditions and shallow pore waters, ranging from shallow seas to deep ocean basins (Loubere, 1991).

3.3.9.2 Oxygen isotope

On well-preserved specimens of the benthic foraminiferal species *N. labradorica*, stable oxygen and carbon isotopic ratios were measured. The measurements were made on specimens selected from the 100-500 μm portion of the forty samples and examined on a Finnigan MAT 253 mass spectrometer equipped with a Kiel IV instrument at the UiT, the Arctic University of Norway, Tromsø. The ^{18}O readings in core HH15-1280-GC were corrected for ice volume changes using the Fairbanks sea-level record (1989). Oxygen isotope ratios are then represented as positive or negative numbers relative to the reference Vienna Standard Mean Ocean Water (VSMOW) (= 0), as follows:

$$\delta 18O = 1000 * \frac{(18O/16O)\ \text{sample} - (18O/16O)\ \text{VSMOW}}{(18O/16O)\ \text{VSMOW}}$$

Changes in the abundance of the heavy isotope ^{18}O are referred to by the words enriched/depleted, heavier/lighter, and positive/negative (Armstrong and Brasier, 2013).

3.3.9.2.1 Vital effect

Vital effect refers to the influence of physiological and environmental factors on the isotopic composition of an organism's shell or tissue. These effects can result in differences between the isotopic composition of the organism and the surrounding water or sediment, leading to potential inaccuracies in paleoclimate reconstructions. Therefore, it is important to understand and account for these vital effects when interpreting isotopic data in paleoclimate studies. Various methods, such as analyzing multiple species with different vital effects or using independent proxies, can be used to correct for vital effects and improve the accuracy of paleoclimate reconstructions (Duplessy et al., 2005)

3.3.9.2.2 Ice volume effect

The oxygen isotopic composition of foraminifera is commonly used to reconstruct past changes in the global ice volume. This is because the isotopic composition of the water in which foraminifera live is influenced by the amount of ice present on the planet's surface. As ice

volume increases, the isotopic composition of the ocean becomes enriched in the heavier isotope, ^{18}O, due to fractionation effects during evaporation and precipitation and more ^{16}O is stored in the ice. Conversely, during periods of reduced ice volume, the isotopic composition of the ocean becomes enriched in ^{16}O. Therefore, it is important to correct for the influence of ice volume when interpreting oxygen isotope records. One commonly used method is to subtract a linear trend from the oxygen isotope record, if the trend represents changes in ice volume over time. In this research, we used the Fairbanks (1989) ice volume correction method to remove the effect of ice volume from the oxygen isotope record of the foraminiferal tests.

3.3.9.2.3 Bottom Water Temperature (BWT)

In this study, is calculated the bottom water temperature (BWT) using the Shackleton equation, which relates the oxygen isotope ratio ($\delta^{18}O$) of foraminiferal calcite to the ambient water temperature. The equation is as follows:

$$T = 16.9 - 4.38 * (\delta 18O_c - \delta 18O_w) + 0.1 * (\delta 18O_c - \delta 18O_w) \text{ ^2}$$

Here, T represents the paleotemperature, $\delta^{18}O_{c\ is}$ the oxygen isotope ratio of the foraminiferal calcite (*N. labradorica* in this study), and $\delta^{18}O_w$ is the oxygen isotope ratio of the ambient seawater. To obtain accurate BWT estimates, were applied corrections for vital effects and ice volume to the $\delta^{18}O_c$ values. The vital effect correction was subtracted from the raw $\delta^{18}O_c$ values, while the ice volume correction was calculated based on the literature (Fairbanks, 1989).

For the $\delta^{18}O_w$, is assumed a value of 0.24 ‰, as used by Rasmussen et al. (2014).

3.3.9.3 Carbon isotope

Carbon has two naturally occurring stable isotopes: ^{13}C and ^{12}C, which are absorbed into carbon dioxide (CO^2) as a result of oxidation, and carbon fractionation happens throughout many natural processes (chemical and biological) (Lowe and Walker, 2015). The carbon isotope ratio ^{13}C /^{12}C, denoted as ^{13}C, varies with temperature and the isotopic makeup of dissolved inorganic carbon (DIC) in saltwater. Carbon isotope ratios are then represented as positive or negative numbers relative to the reference (= 0), as follows:

$$\delta 13C = 1000 * \frac{(13C/12C)\ \text{sample} - (13C/12C)\ \text{standard}}{(13C/12C)\ \text{standard}}$$

Changes in the abundance of the heavy isotope ^{13}C are referred to by the words enriched/depleted, heavier/lighter, and positive/negative (Armstrong and Brasier, 2005). The carbon isotopic record may be used to reconstruct ocean circulation, marine productivity, air-sea gas exchange, and carbon storage in the biosphere (Oliver et al., 2009). Carbon isotopes are separated during natural processes due to their various masses, with photosynthesis being the major mechanism. Because ^{12}C is lighter, it is absorbed preferentially during photosynthesis, resulting in a negative ^{13}C signal in the biosphere (Loubere, 1991).

During glacial eras, ^{13}C levels in upper water masses are higher than during interglacial periods, although the ^{13}C /^{12}C ratio in dissolved carbon in the deep ocean is lower (Armstrong and Brasier, 2013; Shackleton, 1977). Vertical circulation of deeper water masses ventilates the ocean, delivering oxygenated water to the ocean's depths. Reduced vertical mixing reduces oxygen levels and production, which is reflected in the ^{13}C signal. Because of their distinct ^{13}C properties, benthic foraminifera give information regarding ocean bottom circulation and ventilation changes (Lowe and Walker, 2015).

Studies have shown that benthic foraminifera primarily rely on organic matter from the surface ocean as their food source, making surface water productivity a critical factor in controlling the species composition, accumulation rate, and geographical distribution of benthic foraminiferal faunas (Loubere, 1991). During photosynthesis, phytoplankton preferentially take up ^{12}C, resulting in ^{12}C-enriched organic matter that sinks to the seafloor, leaving the surrounding surface waters enriched in ^{13}C and giving higher $\delta^{13}C$ values. As oxidation of organic matter releases nutrients and $^{12}CO_2$, $\delta^{13}C$ values decrease at the seafloor. High export production leads to higher $\delta^{13}C$ values in planktic and lower $\delta^{13}C$ values in benthic foraminifera, creating an offset between the two. For example, a decrease in planktic foraminiferal flux and a simultaneous increase in benthic flux may indicate higher surface ocean primary productivity, which can be explained by a higher food supply to the benthic community. Comparisons of $\delta^{13}C$ values in epifaunal and infaunal benthic foraminifera can reflect the presence and preservation of organic matter and ventilation.

3.3.9.3.1 Paleoproductivity

In this study, we investigated the paleoproductivity of the study area by analyzing the stable carbon isotopes ($\delta^{13}C$) and the flux of fossil assemblages in the sediment samples (Barker et al., 2003; Ternois et al., 2000).

The $\delta^{13}C$ values of organic matter in the sediments provide insights into past primary production and nutrient utilization (Rau et al., 1996). Higher $\delta^{13}C$ values typically indicate increased primary production and more efficient nutrient use by phytoplankton (Popp et al., 1998). By comparing the $\delta^{13}C$ values in our sediment samples to other studies in the region and globally, we can identify periods of high and low primary production in our study area (Eglinton et al., 1997).

Furthermore, we examined the fossil assemblages in the sediment samples to gain additional insights into past primary production. The abundance and diversity of microfossils, such as foraminifera, diatoms, and radiolarians, and their flux data can be used as a proxy for past primary productivity (Liu et al., 2009; Sarnthein et al., 2004). High species abundance and diversity usually indicate favorable environmental conditions for primary production (Thomas et al., 1996).

3.3.10 Flux calculation

The flux (accumulation rate) of benthic foraminifera is calculated by multiplying the concentration (density) by the sediment mass accumulation rate. The following approach was used to calculate the flux of benthic foraminifera and IRD:

The sediment samples were roughly 1 centimeter thick. Because the sediment samples are half cylinders, the volume of the sediment samples is given by:

$$Volume\ of\ wet\ sediment\ (cm^3) = \frac{\text{Volume of sylinder}}{2} = \frac{\pi r^2 h}{2}$$

where r is the radius (in cm) of the sediment samples and h is their height/thickness (in cm). The diameter of the inner core liner and hence the sediment inside is 10 cm, providing a radius of 5 cm. The average thickness was one centimeter. This result is a mean volume of 39.267 cm^3.

The volume of the sediment samples was used to compute the porosity, wet bulk density, and dry bulk density:

$$Sediment\ porosity\ (g/cm^3) = \frac{\text{wet sediment weight} - \text{dry sediment weight}}{\text{volume of wet sediment}} = \frac{water\ weight}{\text{volume of wet sediment}}$$

$$Wet\ bulk\ density\ (g/cm^3) = \frac{\text{wet sediment weight}}{\text{volume of wet sediment}}$$

$$Dry\ bulk\ density\ (g/cm^3) = \text{Wet bulk density} - \text{sediment porosity}$$

The mass accumulation rate is calculated using the dry bulk density. The flux of IRD and benthic foraminifera may be calculated as follows:

$$MAR = Liner\ sedimentation\ rate\ (LSR)\ \left(\frac{cm}{Ky}\right) * dry\ \text{bulk density}\ (g/cm^3)$$

where the linear sedimentation rate is determined by:

$$LSR = \ sedimentation\ rate \left(\frac{cm}{Ky}\right) * 1000$$

The final flow equation is provided by:

$$Flux(no./cm^2 ky^{-1}) = concentration\ \left(\frac{no.}{g}\right) * MAR\ (no./cm^2 ky^{-1})$$

3.4 Foraminifera

3.4.1 Introduction

Foraminifera are unicellular organisms (protists) that are widespread in marine environments, ranging from deep sea to inner fjords. They can be found on continental shelves and slopes and adapt to a variety of climatic and environmental conditions. Planktonic foraminifera exist at different depths in the upper water masses, while benthic species live near, on, or in the

sediment. Foraminifera have a soft body that is enclosed by a shell or "test" produced by the organism. The test can be made up of minerals such as calcite or aragonite, organic materials like tecthin, or agglutinated components (Lowe and Walker, 2015). During the formation of their test, foraminifera precipitate many chemical components from seawater, which reflect the properties of the seawater at the time (Loubere, 1991). After their death, become part of the marine sedimentary archives (Rasmussen and Thomsen, 2015).

Ecology is the study of the interactions between the environment and living organisms (Armstrong and Braiser, 2013). The study and understanding of present and ancient marine ecosystems have proven to be useful in paleoreconstructions (Corliss, 1985). Salinity, temperature, oxygen, currents and turbidity, light, and organic and nutritional movement within the water column can all affect the distribution of foraminiferal assemblages (Armstrong and Braiser, 2013; Murray, 2006). Foraminifera are known to inhabit most marine habitats and have strong environmental preferences (Hald et al., 1994; Rathburn and Corliss, 1994; Hald et al., 2004; Korsund and Hald, 1998; Wollenburg and Mackensen, 1998; Polyak et al., 2002)

The distribution of modern planktic and benthic foraminiferal assemblages living in various environmental conditions in the Southwestern Barents Sea, the Nordic Seas, and the Arctic provides an important analogue for interpreting Quaternary paleoenvironmental and paleoceanographic reconstructions (Sejrup et al., 2004; Saher et al., 2012). Numerous studies have been conducted along the slope and shelf along the continental edge in the Nordic and Barents Seas, comparing the fossil foraminiferal record with present distribution (Hald et al., 1994; Hald and Aspeli, 1997; Bauch et al., 2001; Rasmussen et al., 2007; Ślubowska-Woldengen et al., 2008). The use of foraminifera as bioindicators provides a valuable tool for paleoceanographic and paleoenvironmental studies, allowing for reconstructions of past climate, ocean circulation, and environmental conditions.

3.4.2 Benthic foraminifera

Benthic foraminifera are unicellular organisms that can be calcareous, organic, or agglutinated. Their tests can be either single chambered or multi-chambered with septae separating them. They are in- or epifaunal, and mostly inhabit aquatic settings. In most inshore seas and shelf regions, benthic forms dominate the foraminiferal remnants deposited and integrated in bottom sediments after death. When studying foraminifera, it is important to consider the preservation of foraminiferal specimens and potential reworking and re-deposition of sediments. These factors can lead to an incorrect assessment of faunal composition and the paleoenvironment.

However, the core HH15-1280-GC investigated in this study appears to be undisturbed, with homogeneous hemipelagic sediments and little bioturbation.

Benthic foraminifera are the most prevalent microfossil group in Barents Sea sediments and understanding their current Arctic assemblages is critical for reconstructing marine environments (Steinsund and Hald, 1994). The ecology of modern benthic foraminifera is being investigated to determine the distribution patterns and dynamics of communities and their environments. Foraminiferal distribution is influenced by their feeding techniques and microhabitat preferences on the one hand, and climate, ocean circulation, sea-ice, and water mass qualities on the other (Steinsund and Hald, 1994; Murray, 2001).

Salinity, oxygen, temperature, turbidity, bottom current activities, alkalinity, and sediment particle size are all important regulating elements examined to reconstruct paleoecology and paleoceanography (Murray, 2001). For example, the distribution of benthic foraminifera has been linked to oxygen levels in bottom water, with low oxygen levels resulting in a decrease in the number of species and abundance of individuals (Murray, 2001). The species composition of benthic foraminifera can also indicate the type of substrate on which they lived, with species that require a hard substrate indicating a different paleoenvironmental setting than those that live in soft sediment (Murray, 2001).

Studies of benthic foraminifera have been conducted in various marine environments, including the Arctic, and have provided insights into past climate and oceanographic conditions. For example, changes in the composition of benthic foraminiferal assemblages in Arctic sediment cores have been linked to fluctuations in sea-ice cover and ocean circulation patterns (Polyak et al., 2004; Bauch et al., 2010).

3.4.3 The ecological preferences of dominating species

Seven of the dominant benthic foraminiferal species from the core HH15-1280-GC had their ecology described. Less dominant species are briefly discussed because they exhibit brief periods of relative abundance, or because their occurrence may indicate change in the paleoenvironment.

3.4.3.1 *Nonionellina labradorica*

Nonionellina labradorica is a benthic foraminifera species that is known to inhabit highly productive settings with abundant food supplies (Corliss, 1991; Polyak and Mikhailov, 1996; Zajaczkowski et al., 2010). This species is commonly found in glaciomarine habitats, where it prefers cold temperatures as low as 1 °C and salinities as low as 33-34 psu (Cedhagen, 1991; Steinsund and Hald, 1994). *Nonionellina labradorica* is associated with the Polar front, which is characterized by strong organic output and rapid changes. It is often found at moderate depths of water and slightly sandy sediments (Steinsund and Hald, 1994; Jennings et al., 2004).

Nonionellina labradorica is predominantly found in the deepest, middle, and outer parts of fjords, where it is linked to Atlantic water (Hald and Korsun, 1997). This species thrives in dynamic habitats that have temperate, saline, and oxygenated water masses and are impacted by iceberg activity (Vorren et al., 1988). It is located at a medium distance from rivers (Polyak et al., 2002). *Nonionellina labradorica* can survive long periods of food starvation, but it prefers settings with at least seasonally high food supply concentrations of mainly diatoms (Cedhagen, 1991, Polyak et al., 2002).

Nonionellina labradorica feeds on buried organic matter and is known to be associated with areas that have significant Phyto-detritus on the sediment surface (Corliss, 1991; Zajaczkowski et al., 2010). Therefore, a lack of Phyto-detritus on the sediment surface may result in a lack of *N. labradorica*.

3.4.3.2 *Elphidium excavatum forma clavatum*

Elphidium excavatum forma clavata is the most common ecophenotypes of *Elphidium excavatum* and is found on the east and west coasts of Spitsbergen (Feyling-Hanssen, 1972). Although *Elphidium excavatum* forma selseyensis could be present in the examined sediment core, all forms documented are *Elphidium excavatum forma clavata*, referred to as *Elphidium excavatum* in this thesis.

Elphidium excavatum is an opportunistic and infaunal species found in a broad variety of sediment depths (Corliss, 1991; Steinsund and Hald, 1994). It is commonly found in Arctic shelves and widely distributed in Quaternary marine sediments (Steinsund and Hald, 1994; Hald and Korsun, 1997; Polyak et al., 2002). The species dominates in pure polar conditions

with sea ice, considerable turbidity, and rapid sedimentation rates (Steinsund and Hald, 1994; Hald and Steinsund, 1996; Hald and Korsun, 1997). It is typically found in Arctic and shallow seas with rapid temperature and salinity variations, which are characteristic of glacier-proximal settings (Feyling-Hanssen, 1972; Hald and Vorren, 1987; Steinsund and Hald, 1994). It is a salinity and temperature indicator, preferring low temperatures of less than 1 °C and/or lowered salinities of 30 to 34 psu (Hald and Vorren, 1987; Steinsund and Hald, 1994).

The species dominates the bottom of laminated muds, with limited overall diversity, and is typically found in glaciomarine deposits near a receding glacier (Vorren and Hald, 1987; Hald and Korsun, 1997). It is almost exclusively restricted to the Arctic seas of the Barents and Kara Seas (Steinsund and Hald, 1994). The southerly spread of *E. excavatum* in the Barents Sea is limited by winter sea ice and temperatures over 4 °C, as well as competition with species that thrive on more consistent food supply (Polyak et al., 2002). The species is associated with brackish water in the Kara Sea (Hald et al., 2004) and with riverine-influenced near-shore waters at lower latitudes (Feyling-Hanssen, 1972).

3.4.3.3 *Melonis barleeanus*

Melonis barleeanus is a species of foraminifera that is widely distributed in the Arctic and subarctic regions. It is an intermediate infaunal species, meaning that it lives in the sediment but close to the sediment surface (Corliss, 1991). The species is typically found in areas with rapid sedimentation and fine sediments that contain high and consistent rates of partially degraded organic carbon (Mackensen et al., 1993; Caralp, 1989; Steinsund and Hald, 1994). In the Barents Sea, *M. barleeanus* is associated with troughs containing cooled Atlantic water with temperatures ranging from 3-4.5 °C and typical salinities of over 32 psu (Hald and Steinsund, 1996). It is most found on the eastern sides of northern troughs, where it feeds on organic matter delivered by winter bottom waves (Steinsund and Hald, 1994).

Melonis barleeanus is known for its strong flexibility in adapting to different environments. It can change to an epifaunal environment depending on food supplies, which allows it to maintain a stable population even in variable conditions (Linke and Lutze, 1993). The species has been found to be a good indicator of productivity in Arctic and subarctic regions, and its abundance has been used to infer changes in organic carbon fluxes over time (Mackensen et al., 1993; Caralp, 1989).

3.4.3.4 *Cassidulina reniforme*

Cassidulina reniforme is a species that is commonly found in cold bottom waters with seasonal sea ice cover. It is the second most significant species in glaciomarine settings (Polyak and Solheim, 1995; Hald and Korsun, 1997; Polyak et al., 2002). The ideal temperature range for this species is less than 2 °C, and it thrives in salinities of more than 30 PSU (Polyak et al., 2002). This species is often dominant in laminated muds (Steinsund and Hald, 1994), and it is frequently found in locations impacted by Atlantic water and is related to warmer interstadials, indicating a distal glaciomarine habitat (Hald and Vorren, 1987; Polyak and Solheim, 1995). *Cassidulina reniforme* is related to local water and is now commonly found inhabiting fjord mouths in Svalbard (Hald and Korsun, 1997).

It is worth noting that the distribution of *C. reniforme* has been shown to be influenced by climate change. In a study conducted in the Arctic Ocean, researchers found that the abundance of *C. reniforme* has significantly increased in areas with decreased sea ice cover (LeKieffre et al., 2015). This suggests that as the Arctic climate continues to change, the distribution and abundance of this species may also be impacted.

3.4.3.5 *Buccella* spp

Buccella spp. is a group of foraminifera dominated by *B. frigida*, with a minor fraction of *B. tenerrima*, that are commonly found in the Arctic region. These species are epifaunal or shallow infaunal in nature (Rosoff and Corliss, 1992).

Buccella spp. are adapted to cold, arctic habitats and are found inside seasonal sea ice-influenced zones, where they take advantage of algae blooms near the ice edge (Hald and Steinsund, 1996; Polyak et al., 2002). The ideal temperature range for these species is 0-1 °C, with salinities of 33-34 psu and water depths of 100-200 meters being optimal (Steinsund and Hald, 1994).

These foraminifera have been found in river-affected regions of the Kara Sea, including the Ob estuary (Polyak et al., 2002). They are also commonly found in shallow places with somewhat sandy substrates surrounding Franz Josef Land (Steinsund and Hald, 1994; Hald and Steinsund, 1996). In current arctic fjords, faunas dominated by *E. excavatum* and *C. reniforme* are frequently joined by *Buccella frigida* and *Buccella tenerrima*, indicating their widespread presence in this habitat (Jennings et al., 2004).

3.4.3.6 *Islandiella helenae/ norcrossi*

Islandiella helenae and *norcrossi* are two species that are morphologically similar identical and are mostly represented by *Islandiella norcrossi*. *Islandiella norcrossi* is an epifaunal or shallow infaunal species that shares a similar distribution pattern to *Buccella* spp. However, it prefers fine sediments and deeper water depths ranging from 200 to 400 meters (Steinsund and Hald, 1994). This species is often found in glacial-distal environments in Svalbard fjords, along with *N. labradorica* (Hald and Korsun, 1997). It is also commonly found in marine mud and glaciomarine sediments, including glacier-rafted debris (Hald and Korsun, 1997).

Islandiella norcrossi shows a significant response to organic fluxes on the seafloor (Jennings et al., 2004) and has been discovered in high concentrations in troughs or depressions filled with winter bottom water with sluggish sedimentation rates (Steinsund and Hald, 1994; Jennings et al., 2004). This species also benefits from seasonal sea ice cover, as it may take advantage of ice-edge algae blooms (Steinsund and Hald, 1994).

3.4.3.7 *Cassidulina neoteretis*

Cassidulina neoteretis is a species of foraminifera that thrives in cold, deep waters. It is known to reflect organic flows to the seafloor and is often found in conjunction with numerous planktonic specimens, indicating a period of mostly subsurface Atlantic water influx, which might enhance ice melting (Polyak and Solheim, 1995). It prefers finer sediments and has the same distribution as planktic foraminifera (Steinsund and Hald, 1994). *Cassidulina neoteretis* is commonly found in Greenland fjords in Atlantic Intermediate Water with a temperature greater than 0 °C (Jennings and Helgadottir, 1994). Its spread is determined by the availability of seasonal food falls, and it is most usually found in depths ranging from 626 to 1500 meters (Rosoff and Corliss, 1992).

3.4.4 Sub-dominating benthic species

3.4.4.1 *Stainforthia loeblichi*

Stainforthia loeblichi is a species of foraminifera that belongs to the family Stainforthiidae. It is an opportunistic species that is typically found in high seasonal production locations (Gustavsson and Nordberg, 2001). The species is known for its tolerance of low temperatures and is often found in cold-water environments with temperatures around 0 °C. It has been observed in locations with seasonal sea-ice cover, such as in the Arctic Ocean and adjacent seas (Gustavsson and Nordberg, 2001).

Stainforthia loeblichi is commonly found in muds, sands, and gravels on bank slopes exposed to cold water (Gustavsson and Nordberg, 2001). It has a similar distribution pattern as the species *N. labradorica*, which is also commonly found in Arctic marine sediments (Steinsund and Hald, 1994). The species is also known to prefer fine-grained sediments, and it has been found in high abundance in locations with slow sedimentation rates.

In terms of its ecological significance, *S. loeblichi* has been used as a proxy for paleoceanographic reconstructions of the Arctic region. The species is known to prefer colder water temperatures and has been used to reconstruct past sea ice cover and ocean circulation patterns. The species has also been observed in locations with high nutrient availability, which suggests that it is an indicator of organic matter flux to the seafloor (Jennings et al., 2004).

3.4.4.2 Miliolids

It should be noted that the Miliolid group is a diverse group of foraminiferal species, with varying ecological preferences and distribution patterns. While some Miliolid species may be epifaunal, others may be infaunal or even planktic in nature (Bé et al., 1977). Therefore, the ecological preferences and distribution patterns of Miliolids should be evaluated at the species level. For example, some Miliolid species have been found in association with cold water masses and seasonal sea ice cover, such as *Miliolinella subrotunda* and *Miliolinella subrotundata* (Polyak and Solheim, 1995; Hald and Korsun, 1997). Other Miliolids species, such as *Quinqueloculina* spp, have been found in warmer waters and are associated with coral reefs and seagrass meadows (Bé et al., 1977).

The distribution Miliolids can also vary depending on sediment type and depth. For example, some Miliolid species have been found to be abundant in carbonate-rich sediments, while others are more abundant in siliciclastic sediments (Bé et al., 1977). Additionally, Miliolid abundance has been found to decrease with sediment depth, although some species may still be present at deeper depths (Corliss, 1991).

3.4.4.3 *Cassidulina laevigata*

Cassidulina laevigata is a species of epifauna or shallow infauna that prefers finer sediments and is typically found in the uppermost sediment layer (Steinsund and Hald, 1994). It has been identified in a range of marine environments, including the North Sea and the Barents Sea,

where it is associated with warm Atlantic Water (Mackensen et al., 1993). In the Barents Sea, *C. laevigata* is restricted to regions with bottom water temperatures over 2°C, indicating a preference for relatively warmer waters (Mackensen and Hald, 1988).

This species has been used as a paleotemperature indicator in sediment cores from the Arctic and subarctic regions, as it responds to changes in bottom water temperature (Mackensen et al., 1993). *Cassidulina laevigata* has also been found in laminated muds in the Barents Sea, indicating a glaciomarine environment (Steinsund and Hald, 1994).

3.4.4.4 Agglutinated species

The agglutinated foraminifera are a diverse group of benthic foraminifera that build their shells by agglutinating sediment grains or other particles using an organic or calcareous cement. These species are important in paleoenvironmental reconstructions due to their sensitivity to environmental changes and their preservation potential in sediment records.

Agglutinated foraminifera are mostly found in the top few centimeters of sediments but can also occur at greater depths depending on the species and sediment characteristics (Corliss, 1991). The presence and abundance of agglutinated species can provide information on water turbidity, sedimentation rates, and organic carbon content (Zajaczkowski et al., 2010).

Reophax scorpiurus is a commonly found agglutinated foraminifera species that is often associated with cooler bottom waters with temperatures ranging from 2 to 4°C (Hald and Steinsund, 1996). It has also been found to tolerate brine production associated with acidic bottom waters (Rasmussen and Thomsen, 2014).

3. Material and Methods

4. Results and interpretation

4.1 Sedimentological description

The cores are described in stratigraphic order, from the oldest to the youngest. The sedimentological description of the cores is based on visual description, such as the lithological log, XRF, and X-ray images of the core section are included (Fig 4). Additionally, Figures 5 and 6 present the XRF and X-ray images separately, providing a more thorough examination of the core's composition and structure.

Furthermore, magnetic susceptibility, grain-size fractions, and water content data were also analyzed, as presented in Figure 7, which demonstrates the coupling of these physical characteristics with the lithological log. Magnetic susceptibility measurement was conducted using a point sensor at the UiT Geology Laboratory, as shown in Figure 7. It is essential to note that the sensors at the ends of the core sections may detect extremely low or high magnetic susceptibility values, which are considered errors and are excluded from the analysis. IRD, Flux of IRD were analyzed using three size fractions: IRD 150-250 µm, IRD 250-500 µm, and IRD > 500 µm (Figures 8 and 9). Figure 10 present the benthic and planktonic foraminiferal concentrations and their flux and planktonic/benthic foraminiferal ratio.

The sediments in core is mainly clay/silt with number of shells distributed throughout the core. The record was divided into five lithological units (LU).

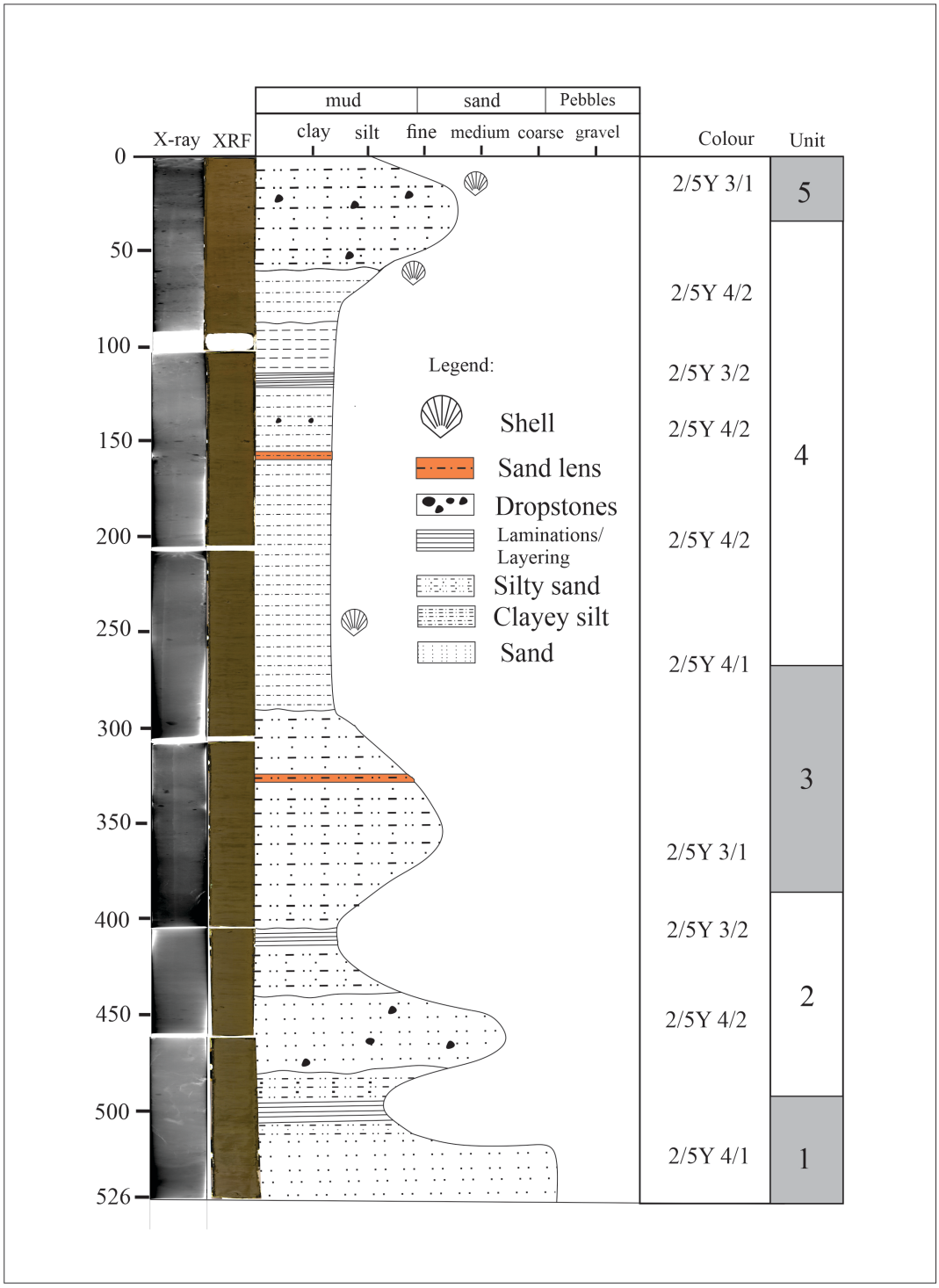

Figure 4: lithological log, XRF, and X-ray images of the core HH15-1280-GC.

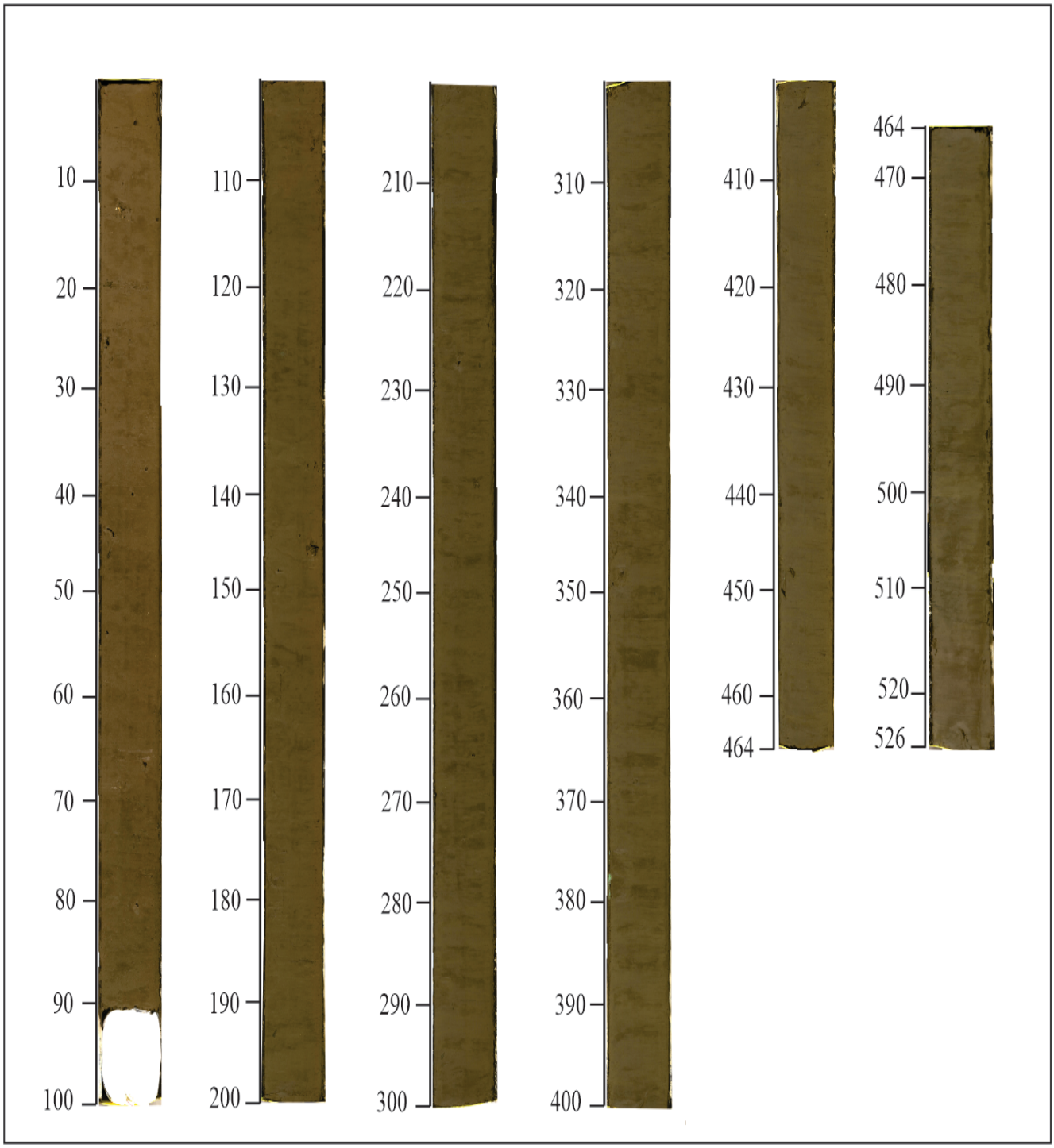

Figure 5: Avaatech XRF core scanner images of the six core sections. The displayed ruler indicates the length of each section in centimeters, providing a visual representation of the sedimentary features and aiding in the analysis of core characteristics.

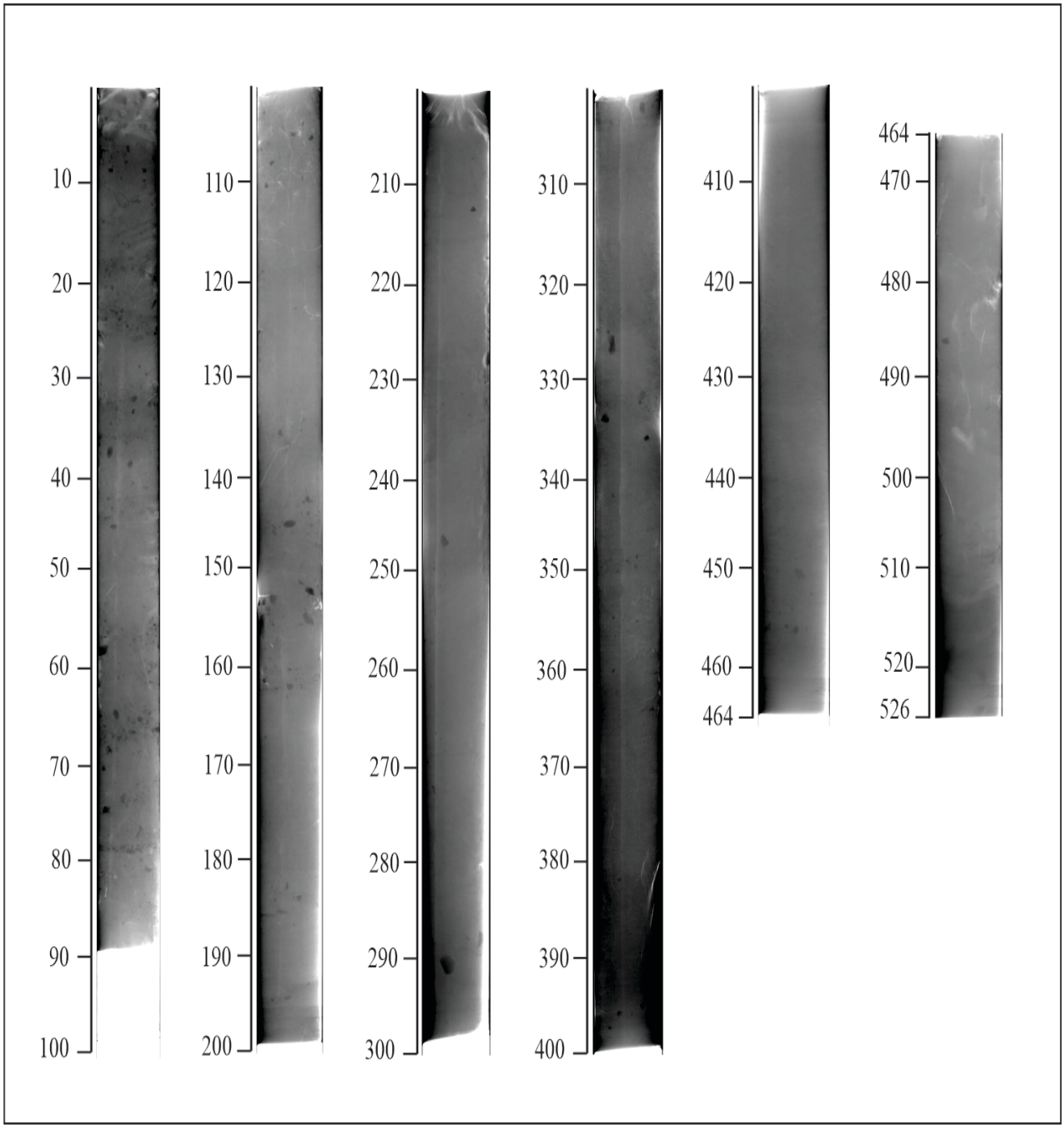

Figure 6: GEOTEK X-ray core imaging system pictures of the six core sections. The accompanying ruler displays the length of each section in centimeters, offering a detailed view of the internal structure, stratification, and sedimentary features for comprehensive analysis.

4. Results and Interpretation

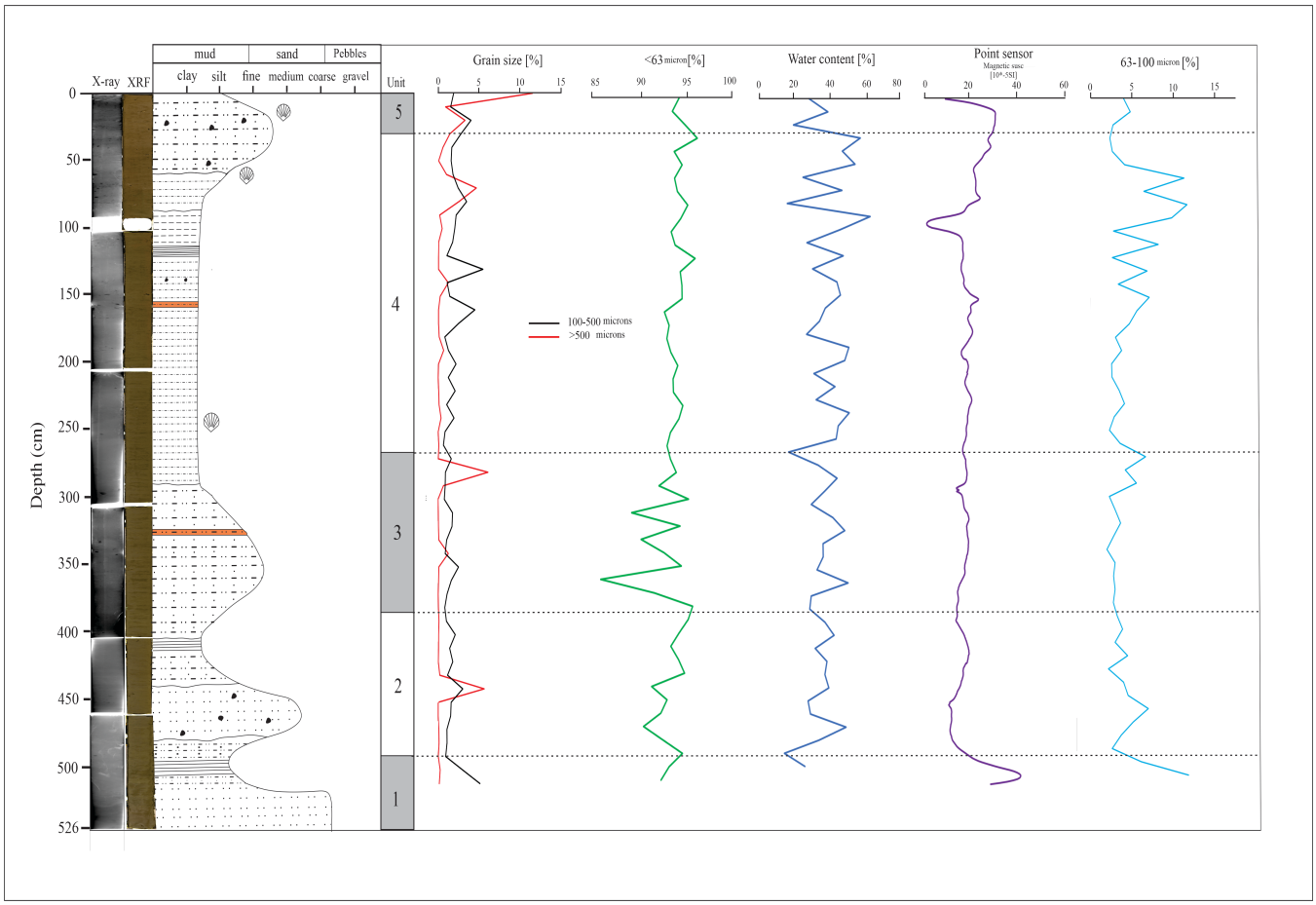

Figure 7: Correlation of magnetic susceptibility, grain-size fractions, water content data and lithological log forming basis for the subdivision into lithological units.

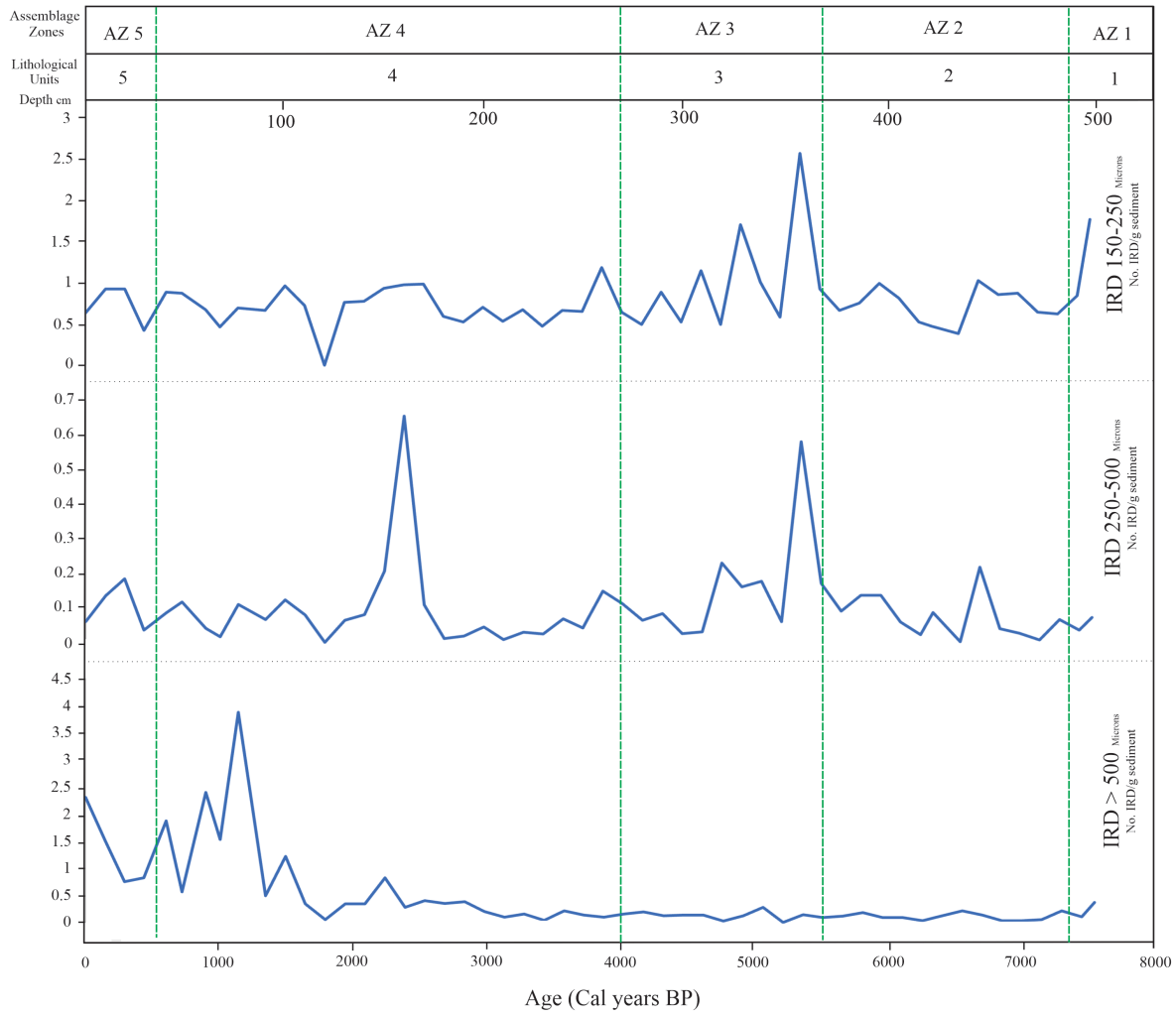

Figure 8: Distribution of IRD size fractions (IRD 150-250 µm, IRD 250-500 µm, and IRD >500 µm) in core HH15-1280-GC from the Hinlopen Strait, plotted against age in calendar years BP and depth (cm).

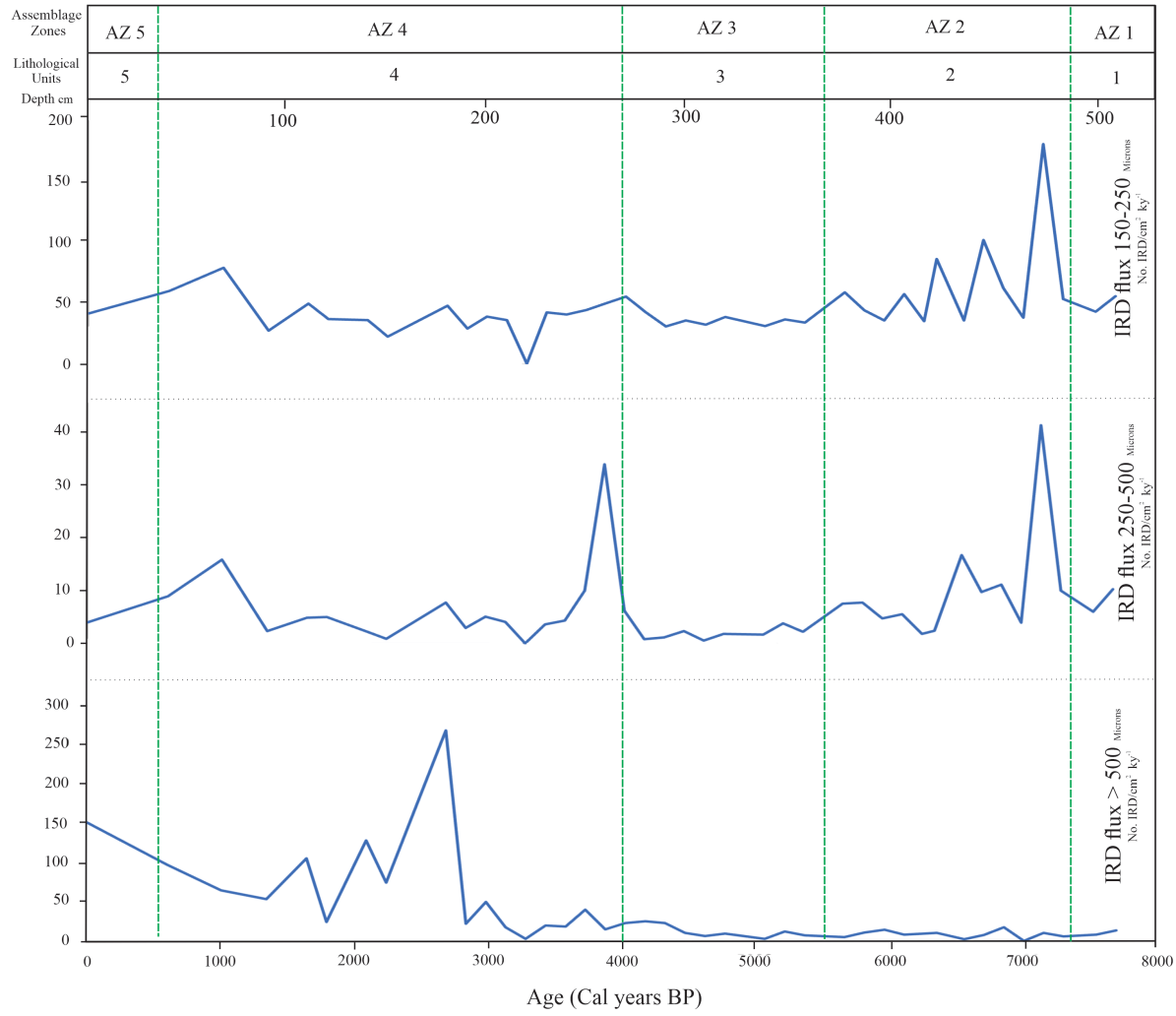

Figure 9: Distribution of IRD flux size fractions (IRD 150-250 µm, IRD 250-500 µm, and IRD >500 µm) in core HH15-1280-GC from the Hinlopen Strait, plotted against age in calendar years BP and depth (cm).

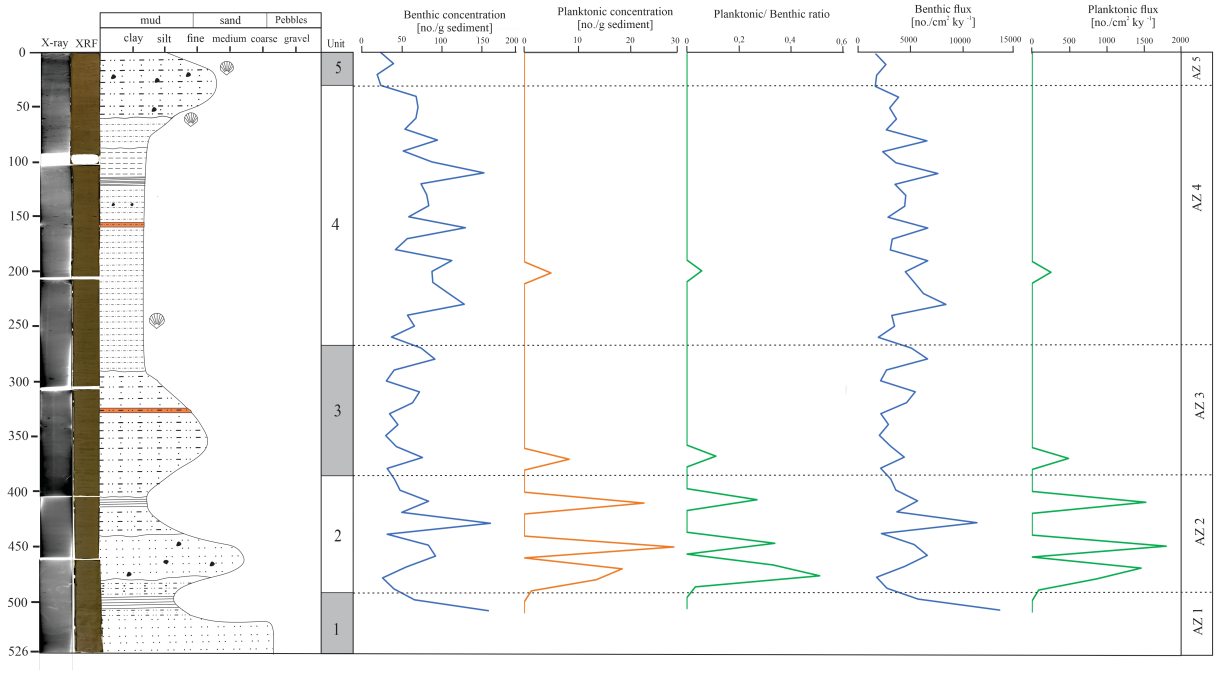

Figure 10: Correlation of benthic and planktonic foraminiferal concentrations and flux, planktonic/benthic foraminiferal ratio integrated with the lithological units marked.

4.1.1 Unit 1 (526-490 cm depth)

Unit 1, spanning from the bottom of the core to approximately 490 cm depth (Fig 4), exhibits a dark grey color (2.5Y 4/1; Figures 4 and 5) and is characterized by abundant sand in a mud matrix. The sediments in Unit 1 are more compact and less water-saturated compared to Unit 2 above. Subrounded to subangular clasts are sparsely observed, with thin laminations in the upper half of the unit (Fig 4).

Unit 1 displays the highest magnetic susceptibility levels (Fig 7), with values of $33*10^{-5}$ SI at 526 cm depth and $42.06*10^{-5}$ SI at 520 cm depth. Magnetic susceptibility diminishes upwards towards the overlying unit. However, data on water content, grain size (Fig 7), concentrations of IRD (Fig 8), and foraminifera (Fig 9) data are limited due to only two sediment samples being extracted from Unit 1 (500.5 and 510.5 cm).

Water content is approximately 40 % at 510.5 cm depth and decreases to 20 % towards shallower depths. Benthic and planktonic foraminifera concentrations at 510.5 cm depth are around 170 and 0 per gram dry weight sediment, respectively (Fig 10). IRD count per gram

sediment declines from 0.9 to 0.2 (Fig 8). The IRD flux follows a similar trend, decreasing from 90 to 20 no./cm^2 k^{-1} (Fig 9).

4.1.2 Unit 2 (490- 370 cm depth)

Unit 2, situated between 490 and 370 cm depth, comprises a mix of clay and sand (Fig 4). Like Unit 1, Unit 2 exhibits thin laminations at both its top and bottom. The color of this unit transitions from 2/5YR 4/2 to 2.5YR 3/2 (greyish brown) (Figures 4 and 5). The water content increases from about 20 % at the bottom to 50 % in the middle and then decreases to 30 % at the top (Fig 7).

Magnetic susceptibility in Unit 2 is moderate, approximately $18*10^{-5}$ SI (Fig 7). Benthic and planktonic foraminifera concentrations per gram dry weight sediment increase, reaching about 170 and 30 in the middle of the unit, respectively (Fig 10). The amount of IRD per gram sediment remains constant at around 0 (Fig 8), with the IRD flux following the same pattern (Fig 9).

The planktonic to benthic foraminiferal ratio generally varies between 0 and 0.5 (Fig 10), indicating the number of planktonic foraminifera per benthic foraminifera. When the ratio is below 1, there are more benthic than planktonic foraminifera. The ratio peaks at the bottom of the unit, at 480 and 450 cm depth, being respectively 0.5 and 0.33.

4.1.3 Unit 3 (370-270 cm depth)

Unit 3, located between 370 and 270 cm depth, mainly consists of silty sand and features a sand lens at approximately 330 cm depth. The lower portion of the unit exhibits a 2/5Y 3/1 color (Figures 4 and 5), transitioning to yellowish grey (2.5Y 4/1) towards the top. Water content within this unit varies from 18 % to 50 %, with the lowest value recorded just below Unit 4 (Fig 7).

Magnetic susceptibility in Unit 3 remains relatively constant, with a value of around $18*10^{-5}$ SI (Fig 7). A significant increase in benthic foraminiferal concentration occurs at 280 cm depth, rising from 40 at the unit's bottom to 90 individuals per gram sediment at this depth (Fig 10). Conversely, planktonic foraminifera concentration and flux are both steady and close to zero throughout the unit (Fig 10).

The number of IRD per gram of sediment in Unit 3 is approximately 0.1 in the lower portion, with no significant increase observed towards the top (Fig 8). Notably, foraminiferal flux in the unit varies from 2000 no./cm^2 k^{-1} at the bottom to 6000 no./cm^2 k^{-1} at the top (Fig 10). These findings suggest that the sedimentary environment during Unit 3's deposition was relatively stable, with a consistent influx of benthic foraminifera and no significant changes in magnetic susceptibility and IRD content.

4.1.4 Unit 4 (270-30 cm depth)

Unit 4, the thickest layer in the sediment core, spans from 270 to 30 cm depth and is composed of silty clay. Two shells found at depths of 250 and 70 cm suggest the presence of marine macro-organisms during this time period. The unit's bottom half is colored yellowish grey (2.5Y 4.1), transitioning to greyish brown (2/5Y 4/2 and 2/5Y 3/2) in the top portion (Fig 5).

Water content in Unit 4 varies, ranging from 20 % to 61 %, with the highest value of 61.4 % observed at a depth of 90 cm (Fig 7). Water content gradually decreases from this depth towards Unit 5. Magnetic susceptibility varies from low to high, with the highest value of $29.2*10^{-5}$ SI at a depth of 36 cm, and the lowest value of $2.05*10^{-5}$ SI at 96 cm depth (Fig 7). Benthic foraminiferal concentration in Unit 4 increases towards the center of the unit and decreases towards the top (Fig 10). Concentration ranges from 42 to 153 no./g sediment with the highest concentration observed at 110 cm deep (153 no./g sediment). In contrast, planktonic foraminifera concentration remains steady at zero throughout the unit. Benthic foraminiferal flux ranges between 2000 and 8400 no./cm^2 k^{-1}, with a peak observed at a depth of 110 cm (Fig 10).

IRD per gram sediment remains low, at approximately 0 until a depth of 200 cm (Fig 8). The amount of IRD gradually increases, reaching a peak at 80 cm depth. The ratio of planktonic to benthic foraminifera remains around 0 throughout the unit, indicating a dominance of benthic foraminifera in this environment.

4.1.5 Unit 5 (30-0 cm depth)

Unit 5, the uppermost layer of the sediment core, is primarily composed of clayey silt, as indicated by the sediment's composition and texture (Figures 4 and 7). The sediment color is uniformly dark, featuring a brownish-black hue (2.5Y 3/1) throughout the layer (Figures 4 and 5). Water content in the bottom part of Unit 5 is around 20 %, gradually increasing towards the top of the unit (Fig 7). Due to the limited number of sediment samples in this unit, the findings are constrained, similar to Unit 1.

Magnetic susceptibility in this unit remains relatively constant until the middle of the layer, where it drops to approximately $30*10^{-5}$ SI (Fig 7). The decrease in magnetic susceptibility in the middle of the layer could signify a change in the sediment's source or composition.

Benthic foraminiferal concentration in Unit 5 ranges between 20 and 40 no./g of sediment (Fig 10). Benthic foraminifera flux fluctuates, spanning from 2000 to 2500 no./cm^2 k^{-1} (Fig 10). Planktonic foraminifera concentration remains consistently zero, with the ratio of planktonic to benthic foraminifera similarly zero. These results suggest that the sediment conditions in this layer were unsuitable for planktonic foraminifera survival and growth, while benthic foraminifera were present but in low numbers.

The number of IRD per gram of sediment in Unit 5 is approximately one at the bottom and two at the top of the layer (Fig 8). The IRD flux follows the same pattern, ranging from 60 to 140 no./cm^2 k^{-1} (Fig 9). The increase in IRD flux towards the top of the layer could indicate a change in the depositional environment or an increase in the supply of IRD to the site.

4.2 Chronology

4.2.1 Age Model

In order to establish an age model for HH15-1280-GC, the two AMS radiocarbon dates from *N. labradorica* were calibrated using the calibration curve Marine20 (Heaton et al., 2020). The calibrated ages with the highest probability within the mean values of the two ranges were used to build the chronology for the age model. It is important to note that there were no radiocarbon dates available for the top and bottom sections of the core due to limited funds.

The calibrated dates from the core HH15-1280-GC vary from 6362.5 to 1145.5 cal years ago, covering a depth range of 80.5 to 430.5 cm in the core (Table 2). By assuming a linear accumulation rate across the dated layers, the calibrated dates were plotted against depth to establish an age-depth model for the core (Fig 11). From this age model, the ages in subsequent analysis will be given in calibrated (calendar) years BP. It is important to note that this age-depth model assumes a constant sedimentation rate, which may not be the case for the entire length of the core. Further studies incorporating additional dating methods or sedimentological analyses can be employed to refine the age model and sedimentation rates in the core.

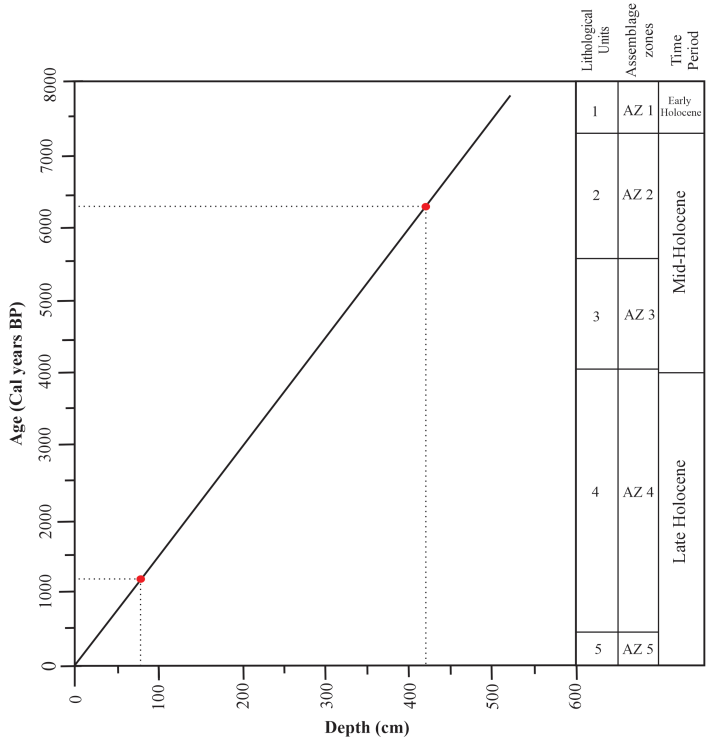

Figure 11: Age-depth model for core HH15-1280-GC based on calibrated radiocarbon dates and assumption of linear accumulation rates.

4.2.2 Sedimentation rate

The sedimentation rates calculated between the calibrated radiocarbon dates provide valuable information on the accumulation rates of sediments in the study area. The average sedimentation rate between 0 cm and 80.5 cm depth is 70.27 cm/ky assuming recent sediments at the core top, while that between 80.5 cm and 430.5 cm depth is 67.08 cm/ky. Assuming that the sedimentation rates remain constant outside the calibrated radiocarbon dates, the sediment's age at the core's bottom is predicted to be 7793±25 calibrated years BP, indicating the age of the sediments at the bottom of the core, which is 526 cm deep. These dating and computations allow the development of an age model, which provides an estimate of the sediment ages throughout the core (Fig 11). Therefore, based on these results, it can be inferred that the sediments in the study area date from the early to late Holocene.

The age model developed in this study is provides a framework for comparing the study's results with other studies in the same or adjacent regions and enable a more comprehensive understanding of the sedimentary processes in the Arctic region during the Holocene (Rasmussen et al., 2012). Similar sedimentation rates have been reported in other studies from the Svalbard region (Rasmussen et al., 2012), supporting the consistency of the sedimentation rate estimates in the Hinlopen area.

4.3 Description of biozones

Core HH15-1280-GC has been analyzed for down-core distribution of benthic foraminifera (Figures 12 and 13). The foraminiferal record of core HH15-1280-GC comprises 12 calcareous benthic and 2 planktonic species, indicating a diverse and well-preserved assemblage. In this study, we will focus on the dominant benthic species, which fulfill the following criteria: (1) they are the most abundant throughout the core, (2) they have specific environmental preferences that can be useful in paleo reconstruction, and (3) they account for more than 5 % of the total fauna in a sample.

Seven benthic species that meet these criteria will be presented in the faunal description. The distribution patterns of these species allow the foraminiferal record to be divided into five

assemblage zones (AZ). Assemblage zones are described in stratigraphic order, from the oldest to the youngest. Figures 12 and 13 illustrates the distribution of these benthic species, as well as the density, flux, and diversity of the fauna in the different samples. The assemblage zones correspond to the same boundaries as the lithological units, highlighting the close relationship between the benthic species distribution and sedimentary environments.

4.3.1 Unit AZ 1: *Nonionellina labradorica* and *Cassidulina reniforme* (526-490 cm)

In Unit AZ 1 of core HH15-1280-GC, which spans from 526 cm to 490 cm, the dominant benthic foraminifera species are *Nonionellina labradorica* and *Cassidulina reniforme*. This assemblage zone marks a transition from sediment with a high flux of foraminifera (14000 no./cm^2 k^{-1}) to a foraminifera-poor sediment (Figures 12 and 13). The zone can be divided into two phases based on the dominant species' significant positive peaks. The first phase between 526 and 510 cm is characterized by a gradual increase in the abundance of *C. reniforme*, which reaches a maximum value of 50 %. The second phase, which spans from 500 cm to 490 cm, is marked by the dominance of *N. labradorica*, which accounts for 65 % of the species.

In addition to the dominant species, the subdominant foraminifera species in this unit include *Melonis barleeanus*, *Islandiella helenae/norcrossi*, *Buccella* spp and *Cassidulina neoteretis*, which account for 12.5 %, 6 %, 4 %, and 2.5 % of the species, respectively. The lowest portion of the zone is characterized by a considerable peak with the highest quantity of 14000 no./cm^2 k^{-1} benthic foraminifera, followed by a decline and fluctuating values.

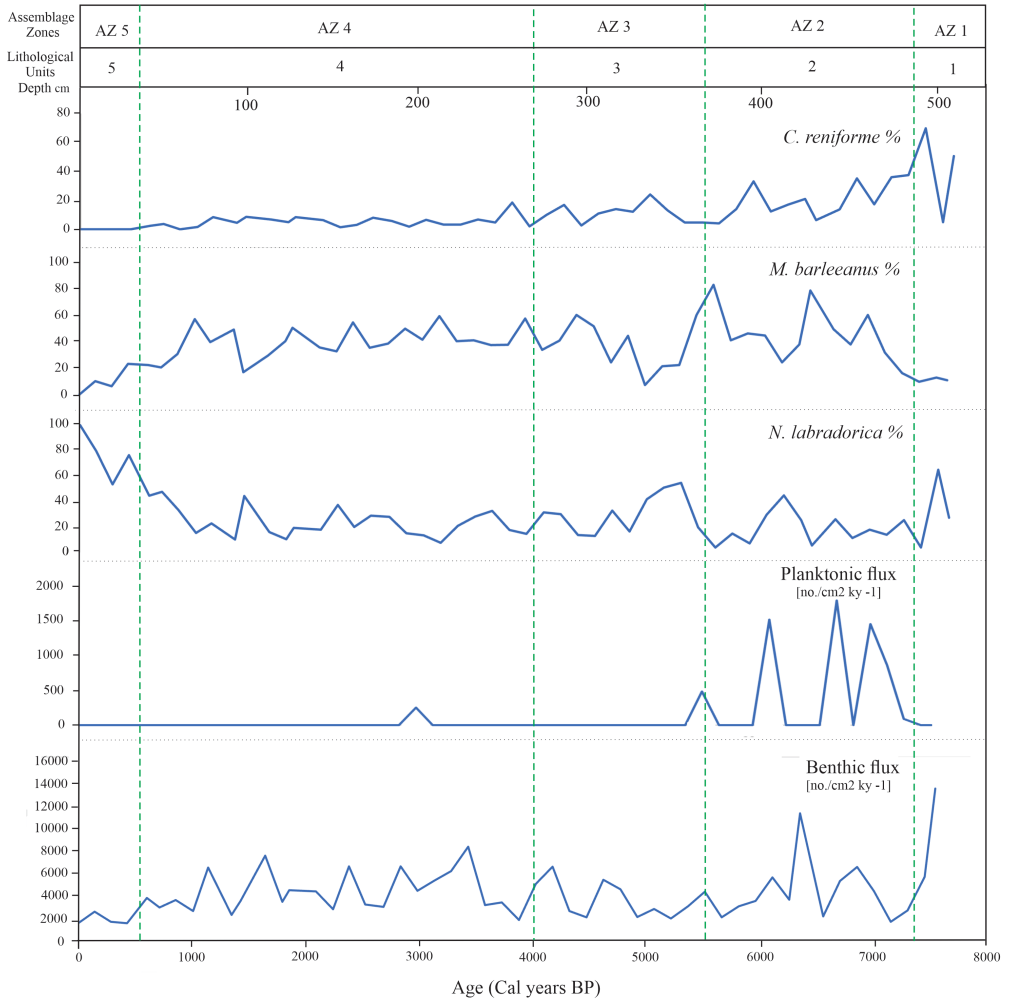

Figure 12: Distribution of dominant benthic foraminiferal species and benthic and planktonic flux in core HH15-1280-GC. The percentage abundance of each species is plotted against age (Cal years BP) and depth (cm).

4.3.1.1 Interpretation

The dominance of *N. labradorica* in the upper portion of the assemblage zone indicates a shift to warmer and less saline conditions, and presence of the sea ice edge and polar front and seasonal sea ice cover (Alve et al., 2016). *Nonionellina labradorica* is a known subpolar species, indicating the presence of subpolar Atlantic Water and a front of high productivity. *Islandiella helenae/norcrossi* and *C. neoteretis* are also indicative of relatively warmer bottom water masses (Hald and Vorren, 1987; Hald and Korsun, 1997). The fluctuating values of foraminiferal abundance suggest a variable environment, likely influenced by seasonal changes in sea-ice cover and water mass variability.

Overall, the assemblage zone suggests a transitional environment, characterized by shifts between colder periods, dominated by Arctic Water masses and extensive sea ice coverage, and

warmer periods influenced by Atlantic Water. These shifts may be associated with changes in oceanic circulation patterns, such as variations in the strength and position of the Atlantic Meridional Overturning Circulation (AMOC) and regional currents, affecting the distribution of water masses, the presence of sea ice, and the heat transport in the study area.

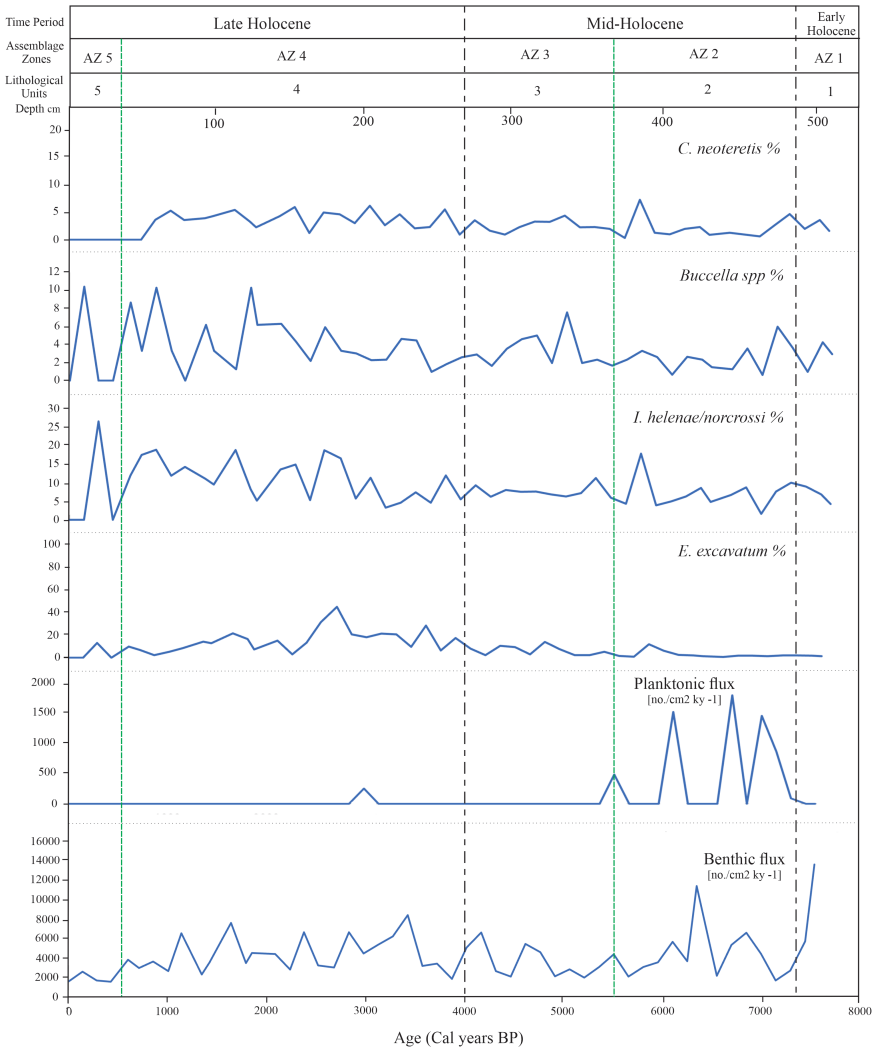

Figure 13: Distribution of dominant benthic foraminiferal species and benthic and planktonic flux in core HH15-1280-GC. The percentage abundance of each species is plotted against age (Cal years BP) and depth (cm).

4.3.2 Unit AZ 2: *Melonis barleeanus* and *Cassidulina reniforme* (490-370 cm)

Assemblage zone 2, which spans from 490 to 370 cm, is characterized by a decline in the relative abundance of *C. reniforme* and *Buccella* spp. and a significant increase in the relative abundance of *M. barleeanus* and planktic foraminifera (Figures 12 and 13). *Melonis barleeanus*

dominates the zone, accounting for 47 % of the entire fauna in the bottom section of the zone. *C. reniforme* diminishes dramatically across the zone but remains over 20 % in the lowest half of the core. *Buccella* spp. shows a progressive reduction down to 1 % and fluctuates between 1 and 8 % across the zone. Other common species include *N. labradorica* (19 %), *I. helenae/norcrossi* (8 %), *Elphidium excavatum* (3 %), *Buccella* spp. (2.5 %), and *C. neoteretis* (2 %).

4.3.2.1 Interpretation

The dominance of *C. reniforme* correlates with the greatest number of planktic foraminifera in the core. This suggests a period of strong influx of chilled Atlantic Water (Polyak and Solheim, 1995; Lubinski et al., 2001; Jennings et al., 2004). The abundance of planktic foraminifera, in conjunction with benthic species that prefer deeper water, also indicates strong inflow of Atlantic Water. *Islandiella helenae/norcrossi* and *M. barleeanus* attain their greatest abundance in the highest tier of the zone, which is attributed to an influx of cold Atlantic Water (Hald and Steinsund, 1996). They also imply increasing salinities and greater fluxes of organic material to the seafloor, presumably owing to algae blooms along the sea-ice edge and Atlantic Water carrying abundant food probably associated with strong tidal currents (Hald and Steinsund, 1996; Steinsund and Hald., 1994). This suggests that the sea ice edge was retreating, and the sea ice cover was decreasing.

In summary, the assemblage zone 2 suggests a changing environment characterized by an influx of cold Atlantic Water, increasing salinities, and greater fluxes of organic material to the seafloor, which indicate that the sea ice was disappearing.

4.3.3 Unit AZ 3: *Melonis barleeanus* and *Nonionellina labradorica* (370-270 cm)

Unit AZ 3, which ranges from 370-270 cm, is dominated by *M. barleeanus* and *N. labradorica*. *Melonis barleeanus* comprises a large proportion of the benthic assemblage in this unit, ranging from 10 to 80 percent (Figures 12 and 13). Other benthic species present in this zone include *N. labradorica*, *C. reniforme*, *I. helenae/norcrossi*, and *E. excavatum*. The percentage of the polar species *C. reniforme* is low yet steady. *Buccella* spp and *C. neoteretis* are also present but in low frequencies. The benthic flux is modest, and the planktic flux is almost non-existent, with a minimal P:B ratio.

4.3.3.1 Interpretation

In this section, the benthic foraminiferal assemblages *M. barleeanus* and *N. labradorica* are discussed in relation to their environmental significance. The presence of *M. barleeanus* in this unit indicates the presence of cold Atlantic Water, which is characterized by low temperatures and high nutrient availability (Mackensen et al., 1993). Additionally, the higher sedimentation rates and fine sediments with high and consistent rates of partially decomposed organic carbon also suggest the presence of a productive and nutrient-rich environment and likely strong tidal currents (Caralp, 1989; Steinsund et al., 1994).

The modest rise in *E. excavatum* up-core suggests a reduction in salinity, which is often associated with changes in oceanographic conditions such as freshwater inputs or changes in sea ice cover (Steinsund and Hald., 1994; Hald and Steinsund, 1996; Hald and Korsun, 1997). *Nonionellina labradorica*, on the other hand, is associated with the Polar Front, a zone where water masses from the Arctic and Atlantic meet, leading to rapid changes in water properties and high organic production (Steinsund and Hald, 1994; Jennings et al., 2004). It is typically found at intermediate depths of water and in somewhat sandy strata.

Overall, the assemblages of benthic foraminifera in this unit suggest a cold, nutrient-rich environment with fluctuations in salinity and the presence of the Polar front.

4.3.4 Unit AZ 4: *Melonis barleeanus*, *Nonionellina labradorica* and *Elphidium excavatum* (270-30 cm)

Unit AZ 4, ranging from 270-30 cm, is dominated by *M. barleeanus*, *N. labradorica*, *E. excavatum*, and *I. helenae/norcrossi*, with maximum relative abundances of 60 %, 45 %, 45 %, and 18 %, respectively (Figures 12 and 13). The relative abundance of *E. excavatum* shows a rise with a maximum value of 45 % before dropping within the top 180 cm (2700 cal yr. BP), indicating changes in salinity (Steinsund and Hald., 1994; Hald and Steinsund, 1996; Hald and Korsun, 1997). In contrast, *C. reniforme* declines significantly across the zone, but remains around 5 % in the uppermost part of the core. Other abundant species include *C. neoteretis* (4 %) and *Buccella* spp (4 %). *Nonionellina labradorica* increases from 10 % to 70 % at 30 cm and is found in the upper zone. The concentration of benthic foraminifera increases within the center of the unit.

4.3.4.1 Interpretation

The benthic foraminifera assemblage dominated by *M. barleeanus*, *N. labradorica*, *E. excavatum*, and *I. helenae/norcrossi* in unit AZ 4 suggests a glaciomarine environment ranging from ice-distal to ice-proximal. The increase in relative abundance of *E. excavatum* indicates cooler bottom water and a reduction in salinity, likely associated with harsher circumstances such as more widespread seasonal ice cover, high turbidity, high sedimentation rates, and enhanced glacial activity and polar conditions. The decrease in *C. reniforme* and the rise in *E. excavatum* also suggest a decrease in inflow of Atlantic water. The presence of *N. labradorica*, *I. helenae/norcrossi*, and *Buccella* spp. indicates substantial organic fluxes to the seafloor, suggesting a system with seasonal sea ice cover and high productivity habitats associated with the ice-edge. (Hald and Steinsund, 1996; Hald and Korsun, 1997; Jennings et al., 2004; Polyak et al., 2002; Polyak and Mikhailov, 1996; Rasmussen and Thomsen, 2014; Zajaczkowski et al., 2010).

4.3.5 Unit AZ 5: *Nonionellina labradorica*, *Melonis barleeanus* and *Islandiella helenae/norcrossi* (30-0 cm)

At around 30 cm, the beginning of assemblage zone 5 is characterized by a notable increase in the relative abundance of several species (Figures 12 and 13). *Nonionellina labradorica* abundance increased from 70 % to 100 %, at the core top, while *I. helenae/norcrossi* increased from 0 % to 25 % (25 cm depth). Meanwhile, certain species like *C. neoteretis* and *C. reniforme* experienced a decline and were absent from the top of the core. The number of benthic foraminifera per gram also declined from 50 to 20 % at 20 cm. Positive oscillations in *I. helenae/norcrossi* and *C. reniforme* connect with negative oscillations in *C. reniforme*.

4.3.5.1 Interpretation

The increase in the relative abundance of *N. labradorica* from 70 % to 100 % in assemblage zone 5 suggests an extremely productive environment with ample food sources (Corliss, 1991; Polyak and Mikhailov, 1996; Zajaczkowski et al., 2010). This species is most abundant in the Barents Sea when bottom waters are colder than 2 °C and salinities are as low as 33-34 PSU (Cedhagen, 1991; Steinsund and Hald, 1994). The rise in *I. helenae/norcrossi* from 0 % to 25 % also indicates the influence of the productive habitats associated with the ice edge (Polyak and Mikhailov, 1996; Zajaczkowski et al., 2010). The decrease in *C. neoteretis* and *C. reniforme* to zero and their absence from the top of the core suggest that the environmental conditions changed significantly. The decrease in the number of benthic foraminifera per gram

from 50 to 20 % at 20 cm indicates a reduction in organic matter supply to the seafloor (Cedhagen, 1991). The positive oscillations in *I. helenae/norcrossi* and *C. reniforme* connect with the negative oscillations in *C. reniforme*, which suggests changes in the water masses and the source of the organic matter supply (Jennings et al., 2004).

4.4 Stable isotope analysis and BWT

The $\delta^{18}O$ and $\delta^{13}C$ values obtained from the benthic sediments in the Hinlopen Strait provide insights into the Holocene climate and oceanic conditions (Fig 14).

Early Holocene (Lithological Unit 1, 7700-7300 cal yr. BP; 526-490 cm depth): During this period, $\delta^{18}O$ levels were low, ranging between 4.16 ‰ and 4.01 ‰, and $\delta^{13}C$ values declined from -1.92 ‰ to -2.34 ‰.

Mid-Holocene (Lithological Unit 2, 7100-5500 cal yr. BP; 490-370 cm depth): $\delta^{18}O$ values rose to a peak at 440 cm depth (6600 cal yr. BP), then decreased towards the end of the unit at 370 cm depth (5500 cal yr. BP). The $\delta^{13}C$ values concurrently increased from -2.3 ‰ to -1.95 ‰. The BWT values decreased from 2 °C at 490 cm to 1.3 °C at 440 cm (7100-6600 cal yr. BP) and then increased to 2.5 °C at 370 cm depth (5500 cal yr. BP).

Mid-Holocene (Lithological Unit 3, 5500-4000 cal yr. BP; 370-270 cm depth): The $\delta^{13}C$ values increased to a peak of -1.54 ‰ at 340 cm (5100 cal yr. BP) before declining to -2.1 ‰ at 270 cm. Concurrently, $\delta^{18}O$ values increased from 4.0 ‰ at 370 cm to 4.14 ‰ at 340 cm, then fell to 4.05 ‰ at 340 cm, and finally increased again to 4.22 ‰ at 270 cm. The BWT values decreased from 2.5 °C at 370 cm to 1.3 °C at 280 cm (4100 cal yr. BP), and then started to increase again at 270 cm (4000 cal yr. BP).

Late Holocene (Lithological Unit 4, 4000-450 cal yr. BP; 270-30 cm depth): $\delta^{18}O$ values exhibited minor fluctuations while $\delta^{13}C$ values decreased to a minimum (-2.7 ‰) around 3500 cal yr. BP and then stabilized. Decreases in $\delta^{18}O$ values were observed between 3500 and 3300 cal yr. BP (270-250 cm), and between 2100 and 1700 cal yr. BP (200-150 cm). Conversely, $\delta^{18}O$ values increased between 1700 and 600 cal yr. BP (150-60 cm). BWT values decreased from 270 cm to a minimum of 1.1 °C at 220 cm (3200 cal yr. BP), at the same time $\delta^{18}O$ reach to maximum (4.28 ‰) then increased to 2.4 °C at 200 cm (3100 cal yr. BP), showed a minor

decrease, and finally increased to a maximum of 2.9 °C at 110 cm (1300 cal yr. BP), before decreasing to present values.

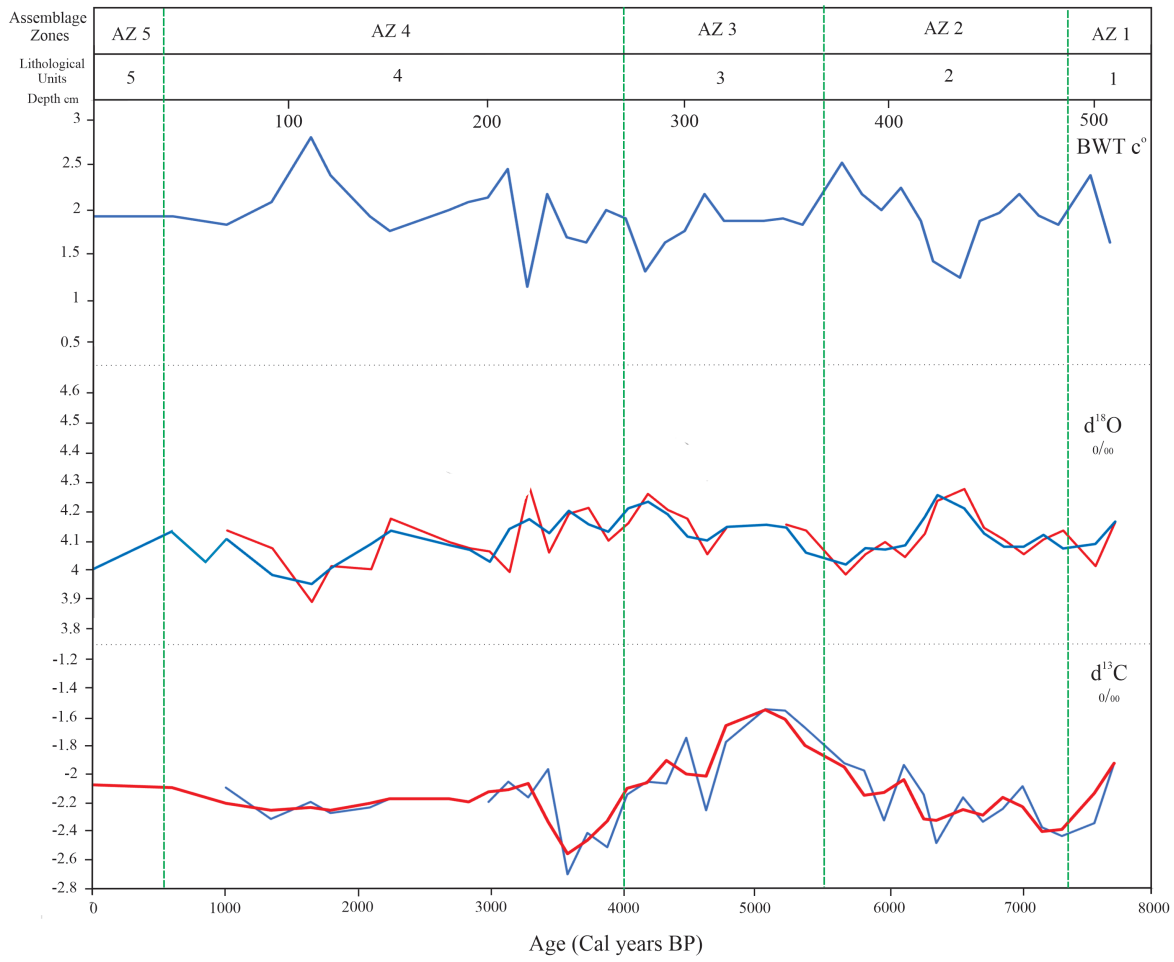

Figure 14: Stable isotope data and bottom water temperature (BWT) for core HH15-1280-GC, displaying $\delta^{18}O$ (blue line represents ice volume corrected values, and red line represents two points mean values for corrected ice volume values) and $\delta^{13}C$ values plotted against calendar age and depth (cm).

4.5 Sortable silt data

Sortable silt is an important parameter in paleoceanographic studies, as it provides valuable information on sediment transport and depositional processes, ocean currents, and sediment supply from land (McCave et al., 1995). In this study, we analyzed sortable silt data to investigate changes in sedimentary environments and their potential links to climate and oceanographic conditions in the Hinlopen Strait.

The analysis of sortable silt in this study uncovered several intriguing observations (Fig 15). Between 526-480 cm (7700-7100 cal yr. BP), the sortable silt percentage (SS%) of 10-63 µm sediments increased from 35 % to 46 %, while the percentage of sediments smaller than 10 µm (% <10 µm) exhibited a declining trend within the same period (from 58 % to 48 %).

Between 480-440 cm (7100 and 6600 cal yr. BP), the SS% content increased, reaching a peak of 53 % at 440 cm (6600 cal yr. BP). Simultaneously, the % <10 µm decreased to 45 %. From 440-420 cm (6600-6300 cal yr. BP), the % <10 µm rapidly increased to 56 %, while the SS% sharply declined to 41 %. In the 420-390 cm (6300-5800 cal yr. BP) interval, both % <10 µm and SS% remained relatively stable at approximately 41 %. From 390-360 cm (5800-5300 cal yr. BP), SS% increased to 51 %, while % <10 µm decreased to a minimum of 37 %.

From 360 cm (5300 cal yr. BP) to 350 cm (5200 cal yr. BP) and then to 330 cm (4900 cal yr. BP), SS% exhibited a minor decrease and subsequent increase. Between 330-320 cm (4900-4700 cal yr. BP), SS% declined, reaching 41 %, while % <10 µm increased to 55 %. In the 310-170 cm (4600-2700 cal yr. BP) interval, % <10 µm, and SS% experienced slight fluctuations, except around 230 cm (3500 cal yr. BP), when % <10 µm increased and SS% decreased. However, the SS% during this interval was the highest throughout the Holocene. From 170 cm (2700 cal yr. BP), SS% began to decline from 52 % to a lower level, reaching 40 % at 140 cm (2200 cal yr. BP). Following a minor rise around 130-120 cm (2000-1900 cal yr. BP), SS% decreased around 90 cm (1500 cal yr. BP) and began to increase at 40 cm (600 cal yr. BP). Ultimately, SS% reached its lowest level in the Holocene (37 %) at 30 cm (400 cal yr. BP), while % <10 µm simultaneously peaked at 63 %.

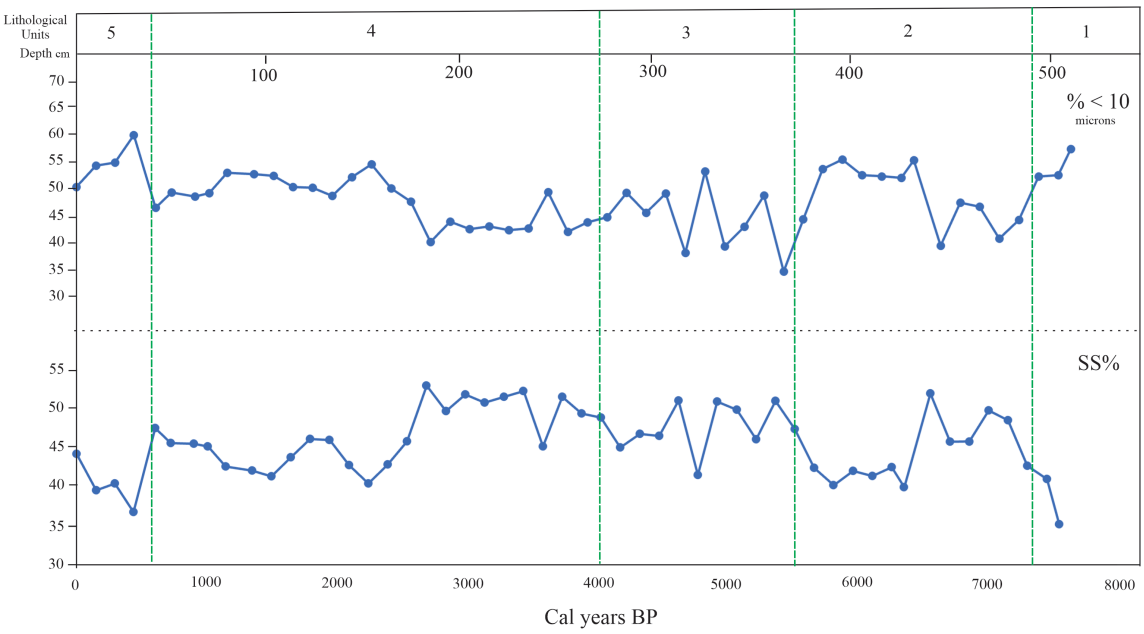

Figure 15: The distribution of sortable silt particle sizes 10-63 µm (SS%) and % <10 µm plotted against calibrated age (cal BP) and depth (cm) for the sortable silt section.

5. Interpretation

In this section, we will discuss various significant climatic events that have been identified in our data, including the Little Ice Age (LIA), Medieval Warm Period (MWP), Dark Ages Cold Period (DACP), Roman Warm Period (RWP) and Little Ice Age (LIA) as well as some other cooling and warming events. These events are explained by their features and highlighted in graphs. The core record HH15-1280-GC has been divided into three-time intervals based on radiocarbon data, benthic and planktic foraminiferal concentration and flux, dominant benthic foraminiferal species distribution patterns, oxygen isotope data of benthic foraminifera, the percentage of various grain size fractions, the concentration and flux of ice-rafted debris, and the magnetic susceptibility:

Time interval c. 7700-7300 cal yr. BP (early Holocene).

Time interval 7300-4000 cal yr. BP (mid-Holocene).

Time interval 4000 cal yr. BP- present (late Holocene).

5.1 Time interval 7700-7300 cal yr. BP (early Holocene)

Our data shows for the late early Holocene a low planktic foraminiferal flux, high benthic foraminiferal flux, and low IRD concentration (Figures 18 and 19), indicating improved environmental conditions and reduced icebergs. This period is characterized by two events: 1) a rapid increase in *N. labradorica* (from 27 % to 65%) at c. 7400 cal yr. BP; 2) an increase of *C. reniforme* (from 50 % to 5%) at c. 7400 cal yr. BP. The dominance of *C. reniforme* with low IRD (0.2 No.IRD/g sediment) and high benthic foraminifera flux (14000 no./cm^2 k^{-1}) indicates strong Atlantic Water influence and significant climatic improvement. The co-occurrence of *C. reniforme* and *N. labradorica* suggests the proximity of the Polar Front's proximity, while low percentages of *C. neoteretis* and *M. barleeanus* abundance indicates reduced advection of Atlantic-derived water.

Buccella spp, averaging 3.5 % (Fig 20), is associated with seasonal sea ice cover and high seasonal productivity, preferring temperatures between 0 °C and 1 °C and salinities around 33-34 PSU. Foraminiferal oxygen isotope data show higher values at 7500 cal yr. BP, probably reflecting lower Atlantic Water influx and lower temperatures. The fine sediment fraction (% < 63 μm) decreases due to higher bottom current activity (Fig 16), but low IRD content and

sand suggest ice-distal conditions. The end of the early Holocene is marked by high clay content (17 %), low IRD, and low SS% values (Fig 16), suggesting weak bottom current speeds and sedimentation dominated by fine-grained material like clay.

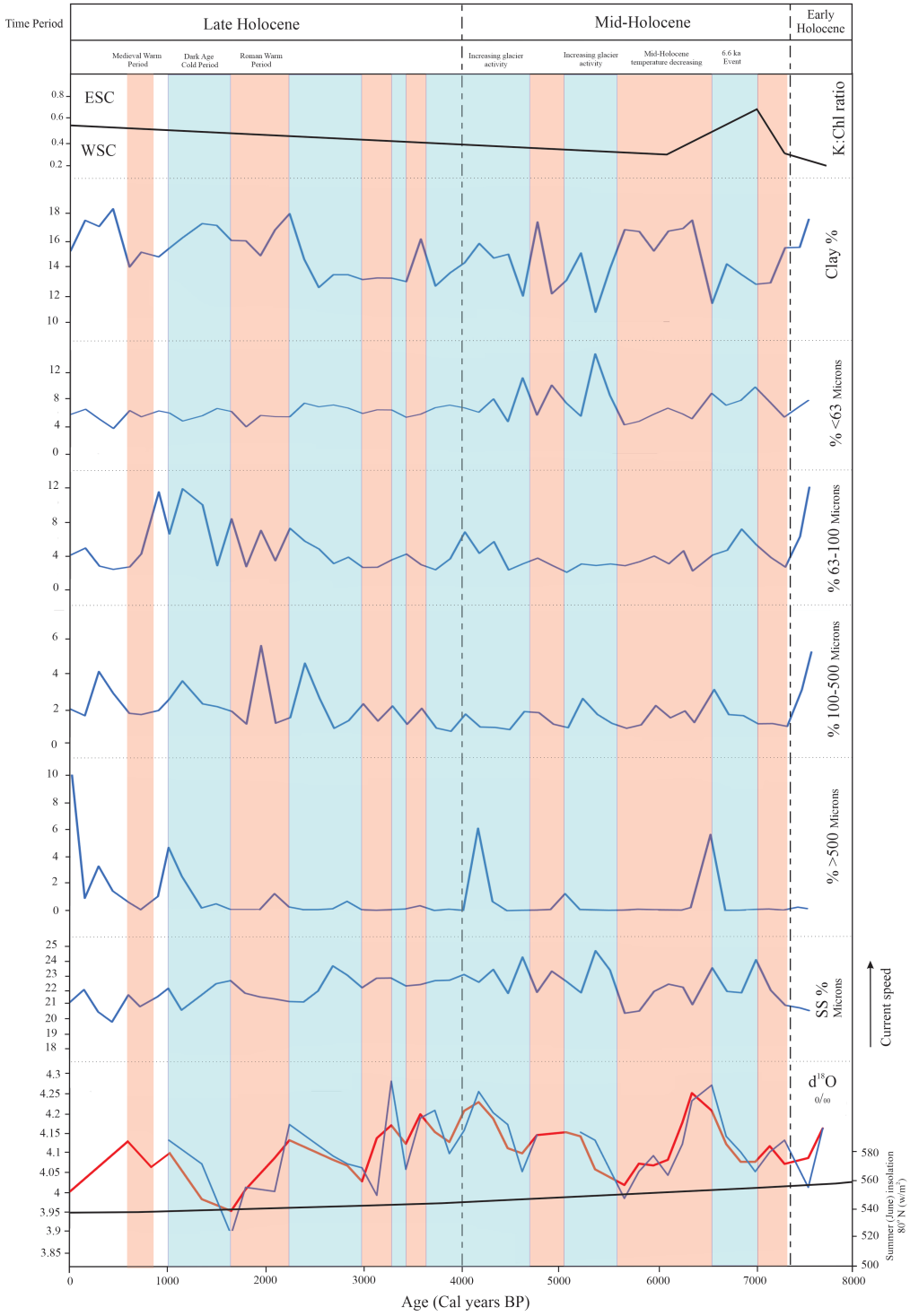

Figure 16: Records of $\delta^{18}O$, summer insolation (80°) (Ślubowska et al., 2005), SSmean, grain-size fractions, and ratio of Kaolinite (K = ESC indicator) to Chlorite (Chl = WSC indicator) (Sternal et al., 2014), plotted against age (cal yr. BP) during Holocene for core HH15-1280-GC (Hinlopen Strait).

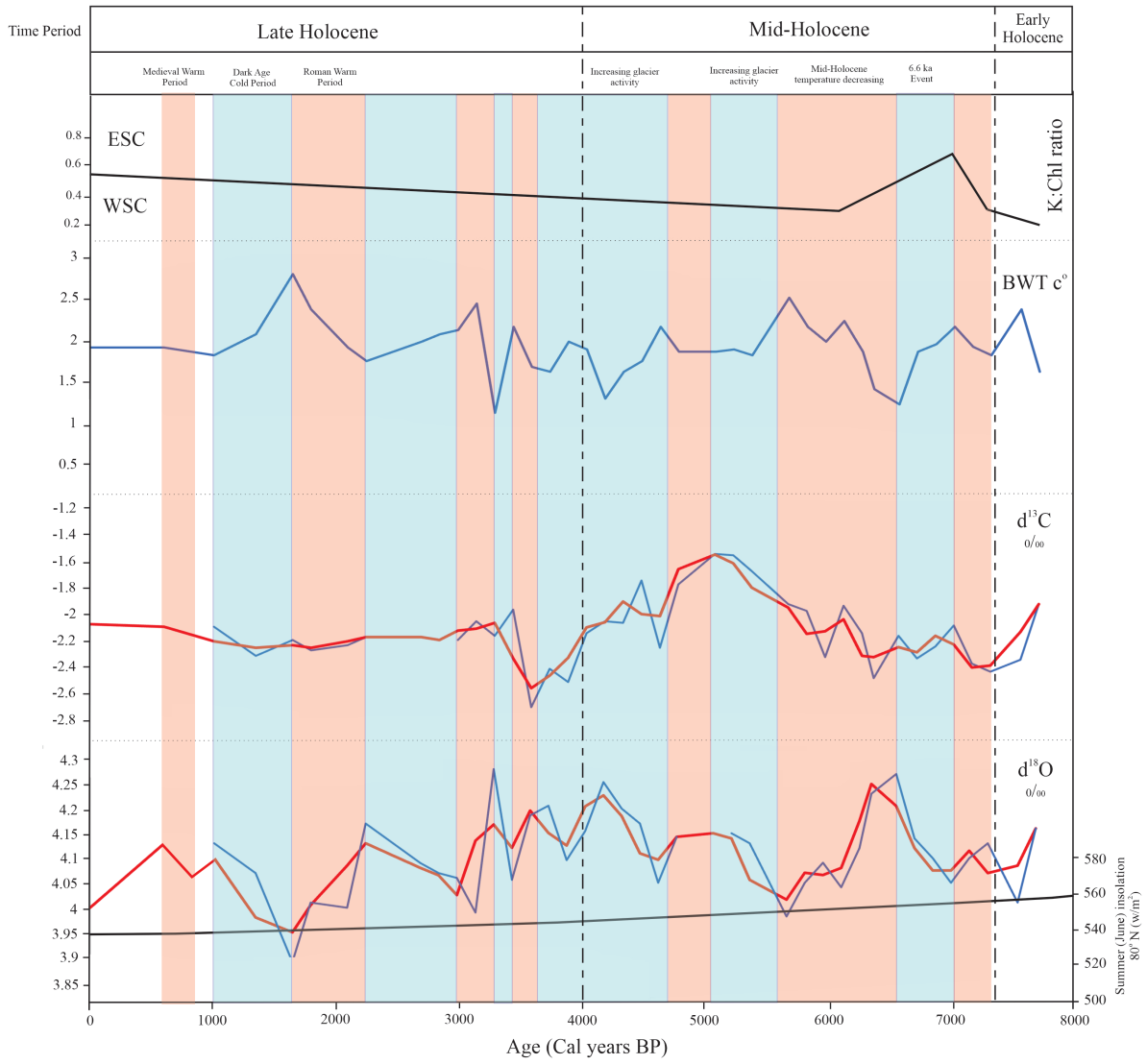

Figure 17: Records of $\delta^{18}O$, summer insolation (80°) (Ślubowska et al., 2005), $\delta^{13}C$, BWT (bottom water temperature; see methods for explanation), and ratio of Kaolinite (K = ESC indicator) to Chlorite (Chl = WSC indicator) (Sternal et al., 2014), plotted against age (cal yr. BP) during Holocene for core HH15-1280-GC (Hinlopen Strait).

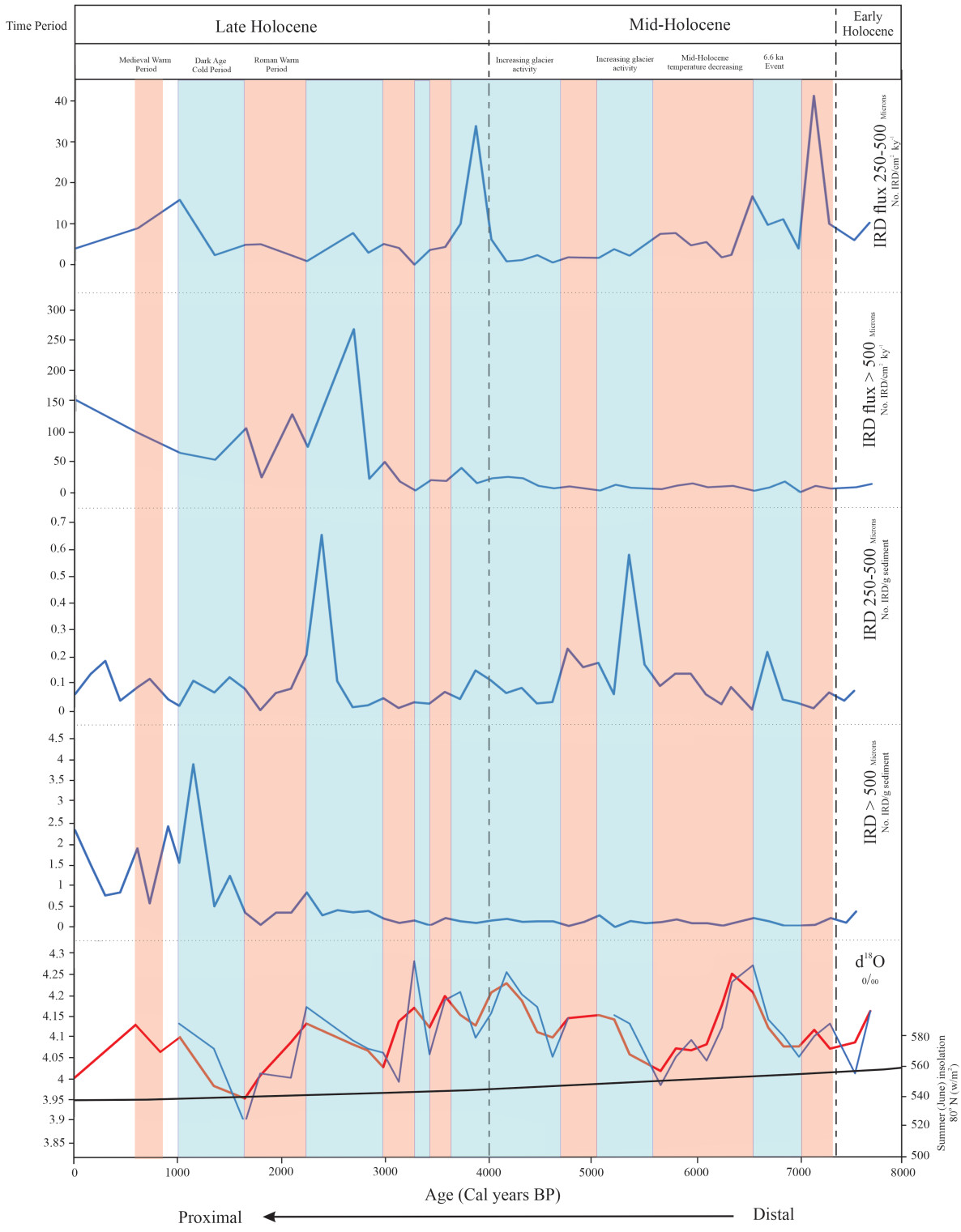

Figure 18: Records of $\delta^{18}O$, summer insolation (80º) (Ślubowska et al., 2005), $\delta^{13}C$, IRD > 500 µm, 250-500 µm and flux IRD >500 µm and 250-500 µm plotted against age (cal yr. BP) during Holocene for core HH15-1280-GC (Hinlopen Strait).

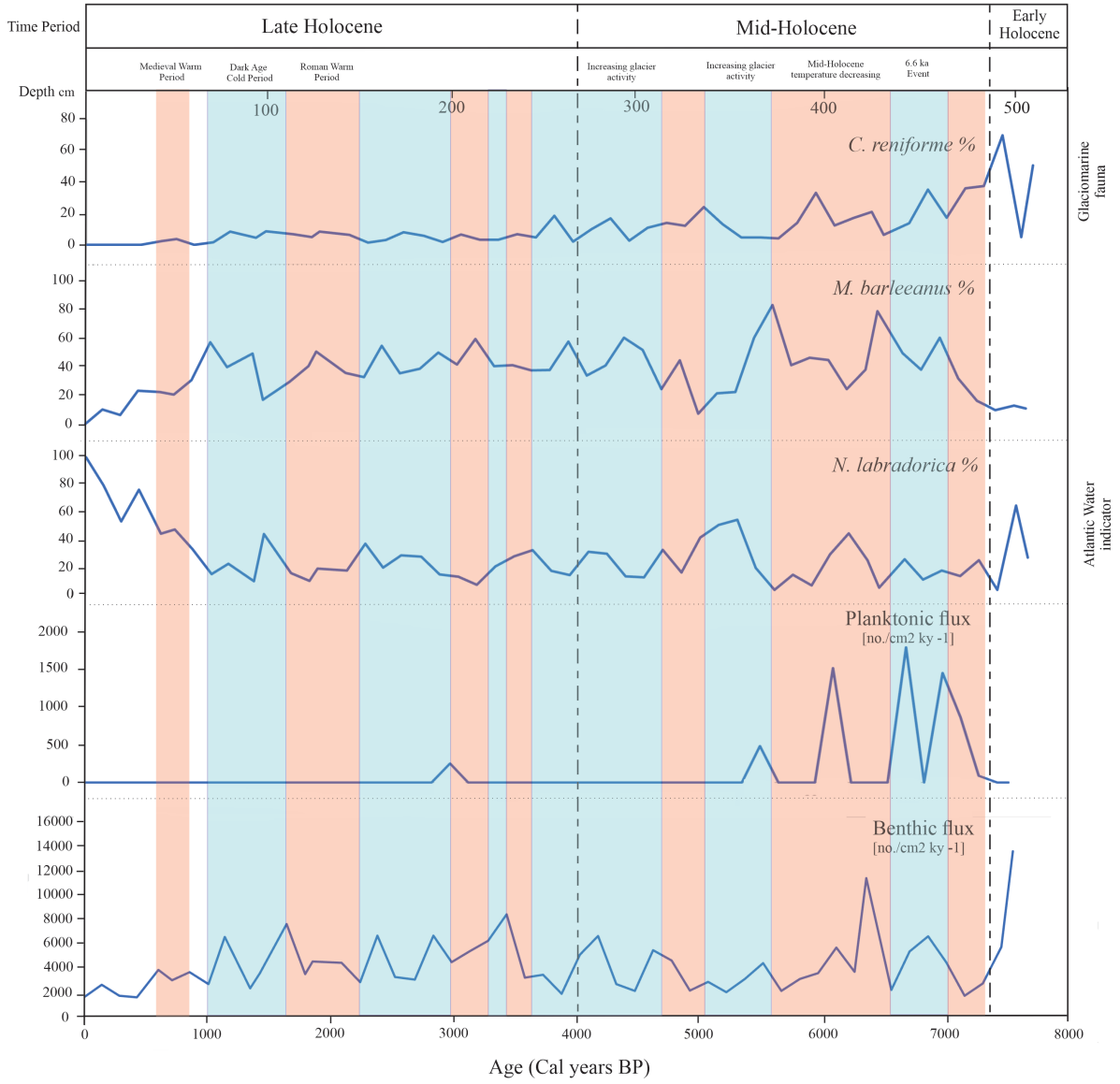

Figure 19: Records of $\delta^{13}C$, benthic foraminiferal flux and relative abundances of selected foraminiferal taxa grouped based on their ecological preferences plotted versus age.

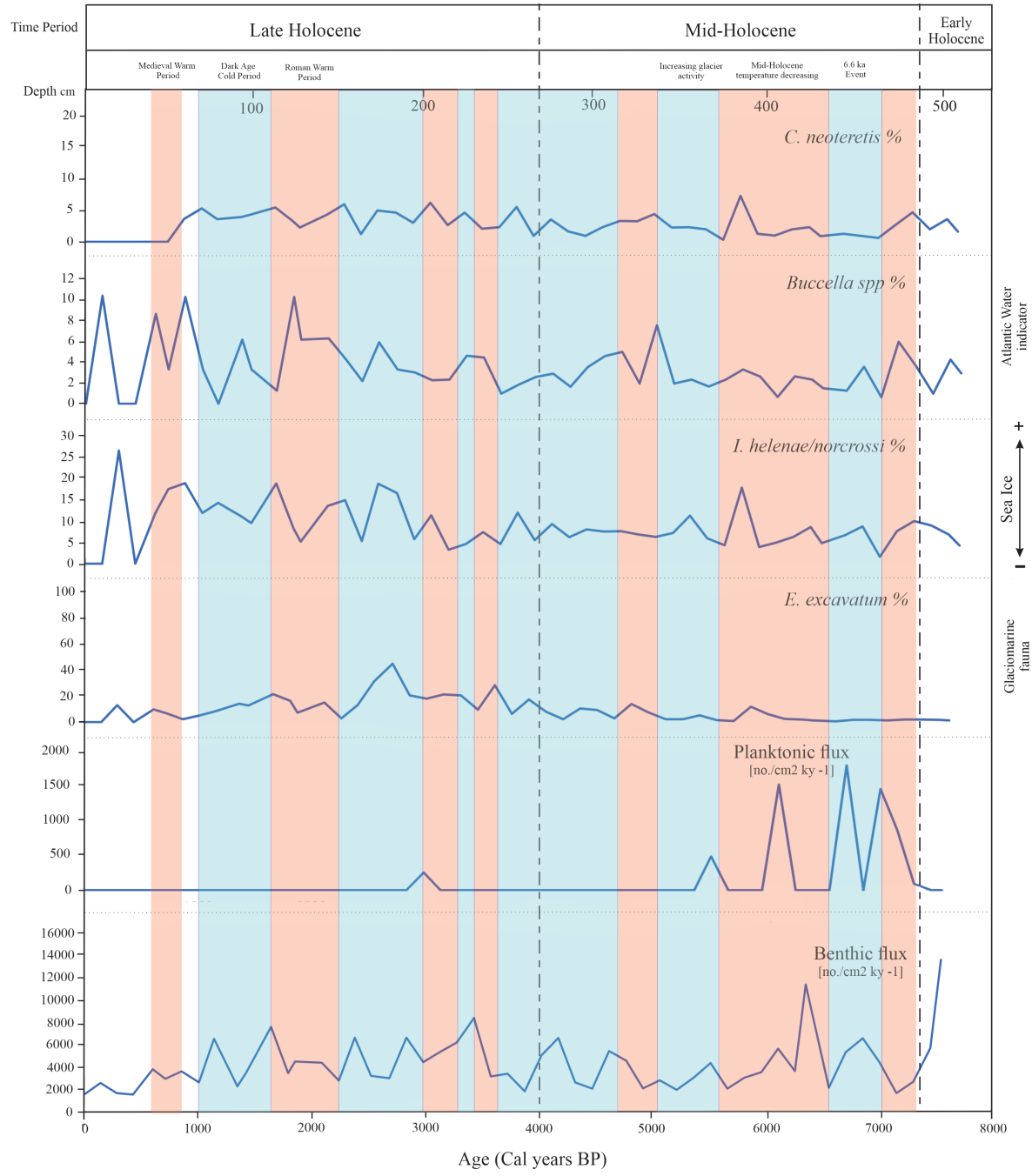

Figure 20: Records of $\delta^{13}C$, benthic foraminiferal flux and relative abundances of selected foraminiferal taxa based on their ecological preferences are shown for Holocene.

5.2 Time interval 7300-4000 cal yr. BP (mid-Holocene)

The mid-Holocene period (7300 to 4000 cal yr. BP), as illustrated, experienced significant changes in the marine environment (Figures 16, 17, 18, 19 and 20). The sediment composition was primarily silty to fine sand, similar to the early Holocene, which suggests sediment accumulation from the water column and minimal influence from strong ocean currents (Fig 16). The magnetic susceptibility is lower than early Holocene. Several abrupt cooling events interrupted the warming trend in the Hinlopen Strait during this period. An increase of meltwater release from melting icebergs during glacial conditions caused a slowdown of the thermohaline circulation and the advection of warm Atlantic water to higher latitudes every 1000 to 2000 years, resulting in a cooling (Bond et al., 1993). This section investigates all cooling and warm events and associated features.

From 7000 to 4000 cal yr. BP (mid-Holocene), $\delta^{13}C$ values and most of the benthic species display higher than average values, which may indicate a period of enhanced productivity or better ventilation (Fig 17). This observation aligns with other studies conducted in the Svalbard and Hinlopen regions (Rasmussen et al., 2014; Ślubowska-Woldengen et al., 2008), which also reported increased productivity and ventilation during the mid-Holocene.

During the first interval (7000-6600 cal yr. BP), climatic and environmental shifts occurred in the Hinlopen Strait. The K/Chl ratio curve (Sternal et al., 2014) reflects the relative contributions of ESC and WSC deposits and helps better understand sedimentary origins and oceanic currents. The peak at 6600 cal yr. BP in K (ESC indicator) suggests cooling and lower salinity resulting from decreased Atlantic Water inflow, increased Arctic surface water, and expanded seasonal sea-ice cover (Fig 17).

Higher $\delta^{18}O$ and BWT values (Fig 17) signal a stronger Arctic Water presence, leading to a more dominant cold-water mass. The major peak (5.5 %) in sediments larger than 500 µm (Fig 16) could indicate increased sediment input or changes in sediment transport dynamics. Environmental shifts, such as lower water temperatures or reduced food availability, may explain the decreased influx of benthic foraminifera. These findings suggest a retreat and weakening of the WSC from the shelf and a growing ESC influence (Fig 17). The period of 7000-6000 cal yr. BP corresponds to the establishment of the modern circulation pattern in the Nordic Seas (Thornalley et al., 2010).

ESC-driven transport of colder, less saline water and sea ice led to strong water column stratification and variable salinity. Seasonal pack ice break-up increased primary productivity, leading to oxygen depletion and low carbon isotope ratios in the bottom waters (Fig 17). A decrease in SS% (22 %) in this interval suggests ocean circulation changes, possibly due to weakened warm Atlantic Water inflow (Fig 16).) The cooling event around 6600 cal yr. BP in Northern Svalbard correlates to records from the Norwegian margin records, indicating a regional influence of Arctic Water and tidewater glaciation (Hald et al., 2007). Thus, the decreasing summer insolation causing a cooler climate and the reduced AW advection may have allowed the glaciers to grow; however, without reaching a size resulting in a considerable increase in deposition of IRD.

The second interval (6600-5600 cal yr. BP) features decreasing $\delta^{18}O$ values, increasing BWT to 2.5 °C (Fig 17), a minor increase in % IRD > 250 µm, and less % IRD > 500 µm (Fig 18), indicating a warming event. This warming could result from reduced glacial meltwater input or increased influence of warmer Atlantic Water. The ratio of Kaolinite to Chlorite (Sternal et al., 2014) decrease (Fig 17), while the high percentage of *M. barleeanus* is indicates enhanced Atlantic Water inflow and high organic matter flux (Fig 19). A decline in sediments larger than 100 µm and 500 µm is observed, and the increased flux of benthic foraminiferal species corresponds to higher water temperatures and food availability. The SS% proxy suggests slower near-bottom currents during this period (Fig 17), and clay content increases, possibly due to changes in sediment sources or transport dynamics from altered oceanographic conditions.

Between 5600 and 5200 cal yr. BP, the Hinlopen Strait experienced climatic and environmental changes marked by increasing $\delta^{18}O$ values (Fig 16), which remained higher than during the first cooling event (7000-6600 cal yr. BP). Concurrently, $\delta^{13}C$ values increased (Fig 17), suggesting changes in water mass properties or oceanographic conditions. A cooling event occurred during 5200-5600 cal yr. BP, with a general weakening of the WSC and increasing ESC influence.

A minor peak in % IRD > 250 µm (Fig 18) indicates limited impact from proximal glacial activity or ice rafting. The flux of benthic foraminifera declined, while percentages of *I. helenae/norcrossi* and *N. labradorica* increased (Figures 19 and 20). Changes in sediment sources or transport dynamics are suggested by decreasing clay content and increasing SS%. Enhanced current speed could result from stronger but colder Atlantic Water influence. Between 5200-4600 and 4600-4200 cal yr. BP, the Hinlopen Strait experienced a warming and cooling event, respectively (Fig 17). The mid-Holocene faunal shift suggests a colder

environment with lower salinity, attributed to reduced Atlantic Water inflow. This reduction would affect glacial activity, the IRD record, and decrease faunal diversity and productivity. The presence of *E. excavatum* indicates more extensive sea-ice cover, high turbidity, and fluctuating salinities (Hald et al., 1994; Hald and Korsun, 1997) (Fig 18).

5.3 Time interval 4000 cal yr. BP-present (late Holocene)

The shift from the mid-Holocene to the late Holocene, spanning from 4000 cal yr. BP to present (Figures 16, 17, 18, 19 and 20), is marked by significant marine environmental changes. The increased relative abundance of *E. excavatum* (Fig 20) during the late Holocene implies harsher conditions, characterized by elevated turbidity and sedimentation rates. Meanwhile, the decline of *C. reniforme* (Fig 20) suggests reduced salinities due to diminished Atlantic Water inflow and a prevailing presence of Arctic Waters. However, the coexistence of *I. helenae/norcrossi* and *C. reniforme* indicates that Atlantic water continues to flow as a subsurface layer. In contrast to other regions in Svalbard, the late Holocene shows warmer bottom water temperatures than the mid-Holocene in the Hinlopen Strait (Fig 17). This is probably primarily due to the strong surface water stratification, which coincided with decrease in near surface current (SS%; Fig 16) and $\delta^{13}C$ values (Fig 17) and diminished ventilation. Reduction in mixing of water layers restricts and isolates the Atlantic bottom water (Fig 17). As a result, the bottom water is unable to lose heat, leading to an increase in water temperature and correspondingly lower $\delta^{18}O$ values.

Between 3600 and 3400 cal yr. BP, a sharp increase in $\delta^{13}C$ (Fig 17) and flux of benthic foraminifera occurred, along with a decrease in percentages of *I. helenae/norcrossi*, *C. reniforme*, concentration of IRD, and $\delta^{18}O$, indicating a stronger influence of cold (modified) Atlantic Water (Nesje et al., 2008; Bakke et al., 2005). From 3400 to 3200 cal yr. BP, a cooling event took place, evidenced by increased $\delta^{18}O$ (Fig 16), higher concentration of IRD > 500 μm (Fig 18), clay content (Fig 16), and flux of benthic foraminifera, along with increased abundance of *Buccella* spp, and a decrease in BWT to (1.1 °C; Fig 17) suggesting expanded sea ice distribution (Ślubowska-Woldengen et al., 2007).

During the late Holocene, the influence of the ESC apparently intensified due to more water stratification, with the increased presence of cold-water species like *I. helenae/norcrossi* suggesting enhanced sea ice presence (Ślubowska-Woldengen et al., 2008). The near-zero

abundance of *E. excavatum* (Fig 20) indicates reduced Polar influence at the sea floor and decreased turbidity.

The Roman Warm Period (RWP; 2200-1600 cal yr. BP) saw a minimum in IRD (Fig 18) and increasing bottom water temperature (2.8 °C; Fig 17), suggesting intensified AW influence. The Dark Age Cold Period (DACP; 1300-1000 cal yr. BP) experienced cooling, increased IRD (Fig 18), and heightened glacial activity (Hald et al., 2007), with the rise in grain size across all ranges (Fig 16) and decreasing BWT to 1.8 °C (Fig 17) indicating increased glacial influence (Svendsen et al., 1997; Humlum et al., 2005). The Medieval Warm Period (MWP; 600-800 cal yr. BP) saw fluctuations in glacial dynamics and oceanographic conditions, with a rise in *E. excavatum* (Fig 20) and decline in cold-dominant species, pointing to the influence of AW and a warmer climate (Miller et al., 2012; Mangerud et al., 2018; Ślubowska et al., 2005).

5.4 Assessing the Influence of Tectonics, Glacial Activity, and Sea Ice on Sortable Silt data and Sediment Transport Dynamics

The sortable silt data in the Hinlopen Strait provides valuable insights into the sediment transport dynamics and paleoceanographic conditions of the region during the Holocene. A more detailed analysis was performed by plotting SS% against SSmean (Geometric mean grain size of 10-63 μm), revealing a positive correlation with an R-value of 0.82 (Fig 21) following McCave and Andrews, 2019. This strong relationship suggests that periods with higher SS% are characterized by a coarser sedimentary composition, indicating increased sediment transport and deposition by stronger bottom currents (McCave et al., 2006). Conversely, lower SS% values are associated with a finer sediment composition, indicative of weaker bottom currents and slower sediment transport (Thornalley et al., 2010). The high degree of correlation between SS% and SSmean demonstrates that the sortable silt fraction is a reliable proxy for reconstructing variations in bottom current strength and sedimentation processes throughout the investigated time intervals (McCave et al., 2006).

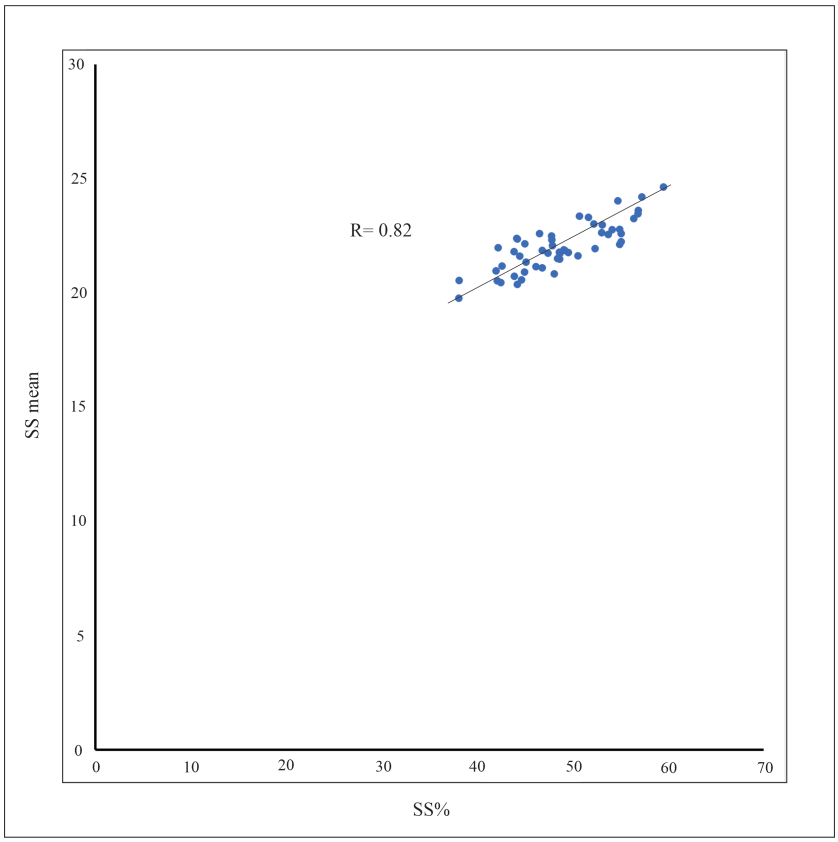

Figure 21: Scatter plot of sortable silt percentage (SS%) against sortable silt mean grain size (SSmean) with a strong positive correlation (R=0.82; liner equation: y = 0.1675 x + 13.848) indicating a close relationship between these two parameters.

However, the downcore points 5 and 7 show (mean of 5 and 7 points) R values below 0.5 during the intervals 450-1700 and 2700-3700 cal yr. BP (Fig 22), which warrant further investigation.

The Lomfjorden-Agardbukta Fault Zone (LAFZ) is a significant tectonic feature in the region (Fig 23) and may have a notable impact on the sortable silt data during specific intervals. The fault zone could potentially influence sedimentary processes and current patterns in the area, which might, in turn, affect the sortable silt data and the reliability of the R parameter (Ottesen et al., 2005). The LAFZ can alter sedimentary processes and current patterns in several ways:

1. Topographic changes: The fault zone may cause topographic variations on the seafloor, leading to changes in current flow patterns. These modifications could result in an increased or decreased deposition of sortable silt particles, depending on the local current dynamics.

2. Sediment supply: The fault zone could impact the amount and type of sediments supplied to the region by influencing nearby erosion and sediment transport processes. For example, tectonic movements associated with the LAFZ may cause an increase in erosion rates from nearby land areas, consequently affecting the sortable silt content in the sediments.
3. Seafloor instability: The fault zone's tectonic activity may induce seafloor instability, leading to mass wasting events such as landslides or turbidity currents. These events can cause the re-suspension and re-distribution of sortable silt particles, altering the sortable silt data and potentially affecting the R parameter's reliability.

The proximity of the Hinlopen Strait to Spitsbergen suggests that sedimentary inputs from nearby fjords on the Spitsbergen side could be a significant factor. The presence of several fjords on the eastern Spitsbergen coast, such as Lomfjorden, may contribute sediments to the surrounding areas, particularly during periods of glacier advance and retreat. The time intervals 450-1700 and 2700-3700 cal yr. BP coincide with periods of glacier and deglacial activity in the region, including the MWP, DACP, RWP and LIA (Kinnard et al., 2011)

The increase in the abundance of foraminiferal species *E. excavatum*, *I. helenae/norcrossi*, and *Buccella* spp during these intervals suggests a stronger influence of sea ice in the Hinlopen Strait (Fig 22). The presence of increased sea ice could lead to the delivery of unsorted sediments to the study area, disrupting the sortable silt signal and contributing to lower R values during these periods. Additionally, low productivity and a reduced amount of particles smaller than 2 μm (clay content) during these intervals further support the idea of a stronger sea ice influence.

Increased water column stratification during the intervals 450-1700 and 2700-3700 cal yr. BP may have also contributed to the observed lower R values in the sortable silt record. The combination of reduced vertical mixing, changes in sediment deposition patterns, and the influence of sea ice could have disrupted the sortable silt signal, resulting in less reliable R values during these time periods.

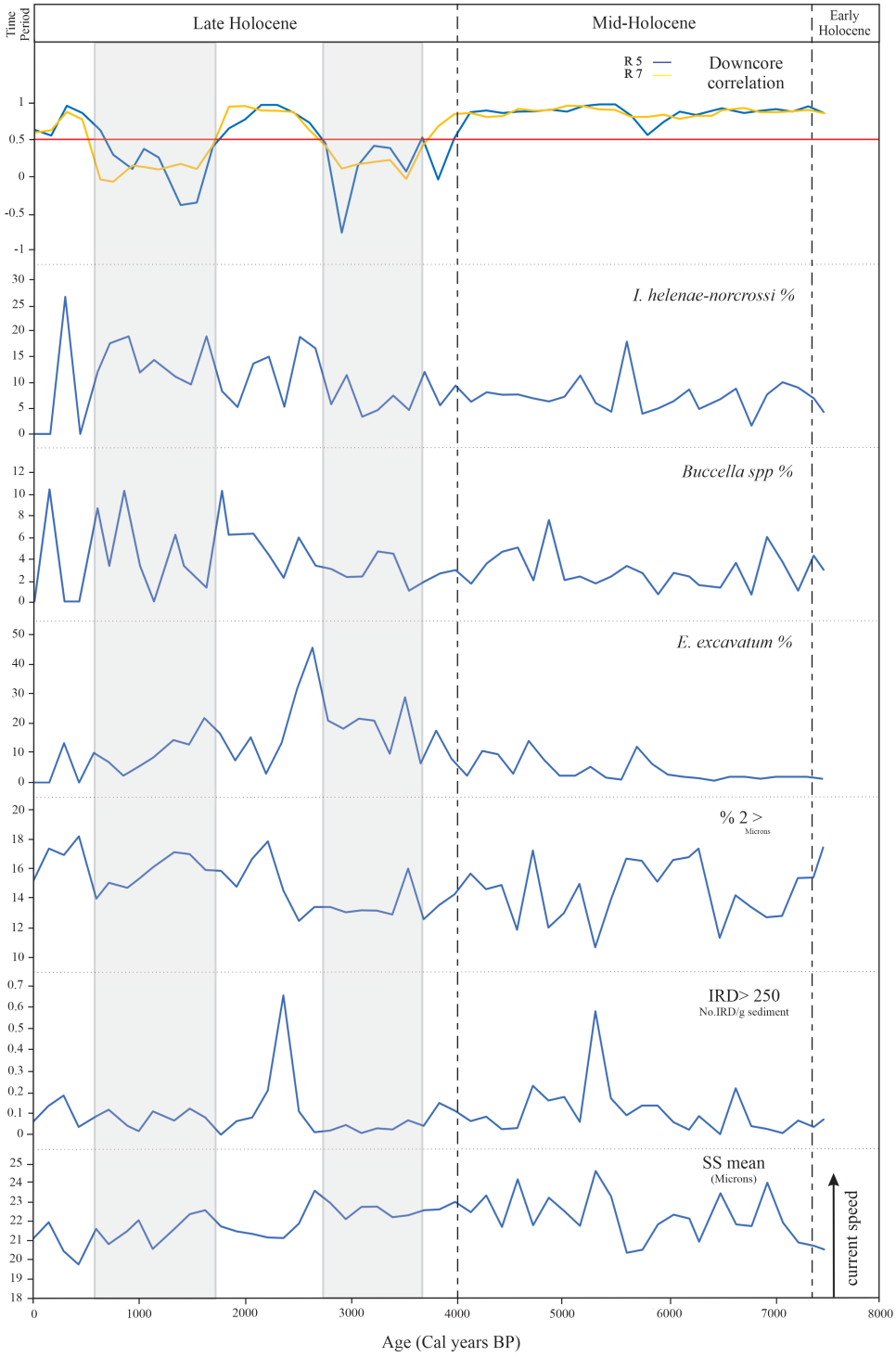

Figure 22: Clay content, IRD, SSmean, and R values, plotted along three dominant benthic foraminifera sensitive to iceberg presence. Gray bars highlighting intervals 450-1700 and 2700-3700 cal years BP indicating periods where the R parameter is less than 0.5.

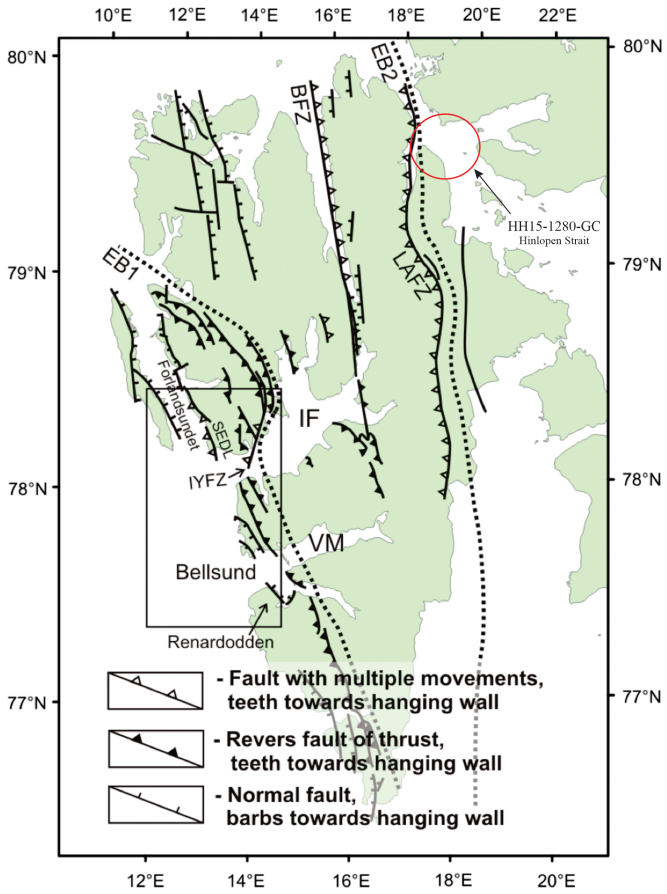

Figure 23: Map of the study area in the Hinlopen Strait, highlighting the core location and proximity to the LAFZ fault zone (Lomfjorden-Agardbukta Fault Zone) and nearby fjords on the Spitsbergen side, such as Lomfjorden and Billefjorden. Modified from Piepjohn et al. (2015).

6. Discussion and correlation

6.1 Development during the Holocene

A discussion and correlation of the obtained sedimentological and foraminiferal data, with the created age model is presented in the first part of this chapter. The results are divided and discussed within different time intervals from the early Holocene to the present. This is done to reconstruct the Holocene paleoenvironment and paleoceanography of the study area. The last part aims to put the results in a wider context with observations and implications of the paleoceanography of the Nordic Seas, Barents Sea and the Svalbard margin.

6.1.1 Early Holocene

Our study's early Holocene data is somewhat limited, but the available evidence points to improved environmental conditions. The period is marked by a reduction in iceberg presence and low concentrations of Ice Rafted Debris (IRD).

The early Holocene was a time of increased summer insolation, resulting in a climate significantly warmer than today (Fig 17). Studies carried out by Ślubowska et al. (2005) and Koç et al. (2002) at the northern Svalbard margin indicate that a rapid decrease in *I. helenae/norcrossi* and an increased abundance of *N. labradorica* signal a southward retreat of the Polar Front (Figures 19 and 20). The dominance of fine sediments, as illustrated in unit 5 of core HH15-1280-GC, suggests an environment minimally influenced by strong ocean currents.

The foraminiferal records from the Hinlopen Strait (as seen in Figures 19 and 20) show a clear shift with a significant increase in *C. reniforme*. *Cassidulina reniforme* is typically found in areas influenced by Atlantic Water and is associated with the warmer part of the Holocene. Its presence indicates ice-distal glaciomarine conditions, signifying a period of reduced ice coverage and warmer waters.

6.1.2 Middle Holocene

The commencement of the mid-Holocene, specifically from 7300 cal yr. BP to 6600 cal yr. BP, is marked by a noticeable decrease in the absolute abundance of planktic and benthic foraminifera, particularly a reduction in *M. barleeanus* and *C. reniforme*. This decline corresponds with an increase in the $\delta^{18}O$ record (Fig 17). An increase in $\delta^{18}O$ values typically signals either a drop in temperature or a rise in salinity (Lubinski et al., 2001). This event aligns with a cooling phenomenon noted in the west Svalbard margin (core MD99-2304; Hald et al., 2004; Ebbesen et al., 2007), the northwestern Barents Sea margin (core MD95-2011; Risebrobakken et al., 2003; Andersson et al., 2003 and core 23258; Hald et al., 2004; Ebbesen et al., 2007), which also saw a minor increase in IRD. According to Hald and Aspeli. (1997), a cooling period around 6500 cal yr. BP can be linked to heightened atmospheric pressure.

This cooling event is mirrored, despite minor discrepancies in timing, in various foraminiferal records from the Svalbard and Barents Sea area. An analogous increase in $\delta^{18}O$ was identified by Ślubowska et al. (2005) from the Hinlopen Trough, Ślubowska-Woldengen et al. (2007) from the Bellsund Trough, Skirbekk et al. (2010) from Kongsfjorden, and Hald et al. (2007) from the northwestern Barents Sea margin and west Svalbard margin (Hald et al., 2007).

The benthic foraminiferal distribution pattern closely aligns with most other Holocene records from the Svalbard and Barents Sea area (Lubinski et al., 1996; Duplessy et al., 2001; Rasmussen et al., 2007). It concurs with a progressive cooling observed in the aforementioned studies, following the Holocene Temperature Optimum and extending into the middle and late Holocene. This cooling, accompanied by diminishing salinity, is likely a result of a decrease in the influx of Atlantic Water, increased prevalence of Arctic surface water, and a more extensive sea ice cover.

From 6600 cal yr. BP to 5500 cal yr. BP, a recovery and stronger influence of Atlantic Water is indicated in the Hinlopen Strait. This is evidenced by an increase in *C. neoteretis*, a high percentage of *C. reniforme*, and a decrease in $\delta^{18}O$ values. Improved conditions, marked by an increase in *C. neoteretis* and a higher concentration of benthic and planktic foraminifera, were similarly noted by Ślubowska et al. (2005) from the Hinlopen Trough, Ślubowska-Woldengen et al. (2007) from the Bellsund Trough, and Skirbekk et al. (2010) from Kongsfjorden.

6.1.3 Late Holocene

The transition from the mid-Holocene to the late Holocene is delineated by an increase in the relative abundance of *E. excavatum*, as evidenced in figure 20. This species' increasing prevalence during the late Holocene suggests a shift towards harsher conditions, characterized by heightened turbidity and elevated sedimentation rates (Jennings et al., 2004). This inference is reinforced by the observed decrease in *C. reniforme*, indicative of diminished salinities due to a reduction in the inflow of Atlantic Water as a subsurface layer (Ślubowska et al., 2007).

The rise in percentage of *E. excavatum*, along with an increase in IRD flux, aligns with late Holocene fauna records reported by Ślubowska et al. (2005) from the Hinlopen Trough, Ślubowska-Woldengen et al. (2007) from the Bellsund Trough, and Skirbekk et al. (2010) from Kongsfjorden. Numerous late Holocene records from the Barents Sea, around Svalbard, and the Greenland shelf, show a similar rise in *E. excavatum* (Hald et al., 2004; Ślubowska et al., 2005; Ślubowska-Woldengen et al., 2007; Skirbekk et al., 2010 and Rasmussen and Thomsen, 2014). This trend is interpreted as a reflection of a general cooling and a paleoenvironmental shift towards more polar conditions across the region.

The late Holocene's onset is marked by an increase in *Buccella* spp, *N. labradorica*, and *I. helenae/norcrossi*, suggesting heightened sea-ice coverage and a southward shift of the Polar Front. This shift is also documented in the Hinlopen Trough (Ślubowska et al., 2005).

In the Hinlopen Strait, an increase in benthic foraminiferal abundances around 2200-1600 cal yr. BP points to improved conditions, potentially corresponding to the Roman Warm Period (Holzhauser et al., 2005). This period is recognized for warm climatic phases in Europe and is characterized by increased benthic foraminiferal abundances in the Hinlopen Strait. However, a sharp drop in foraminiferal abundance is discernible around 1600 and 300 cal yr. BP, which could align with the onset of the Dark Ages Cold Period and Little Ice Age (Grauel et al., 2013).

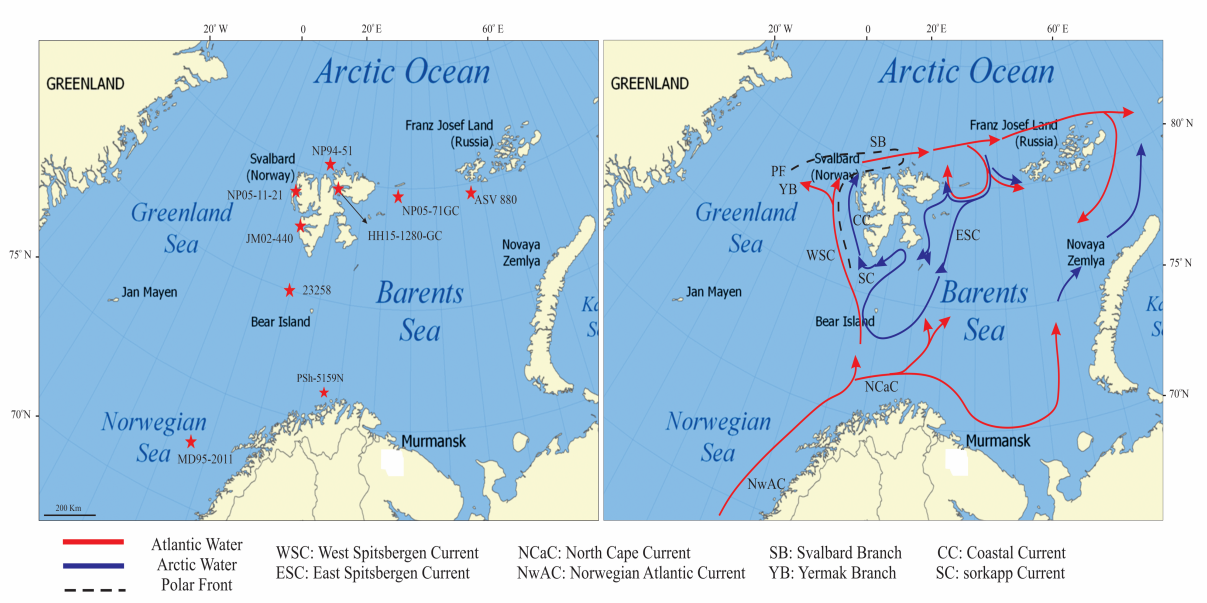

Figure 24: An overview map showing the location of core sites in the Norwegian, Barents Sea and Svalbard area and the approximate path of the currents.

Core ID	Latitude	Longitude	Water depth (m)	Location	References
NP94-51	80° 21.403 N	16° 18.125 E	398	Hinlopen Trough	Ślubowska et al., 2005
HH15-1280-GC	79° 48.113 N	18° 08.560 E	439	Hinlopen Strait	This study
ASV 880	79° 55.5 N	47° 08.2 E	388	Franz Victoria Trough	Duplessy et al., 2005
NP05-11-21	79° 57 N	11° 05 E	327	Kongsfjorden	Skirbekk et al., 2010
NP05-71 GC	79° 58 N	33° E	360	Kvitoya	Kristensen et al., 2013
MD99-2304	77° 37.26 N	9° 56.90 E	1315	W. Svalbard margin	Hald et al. (2004) and Ebbesen et al. (2007)
JM02-440	77° 2 N	13° E	240	Bellsund Trough	Ślubowska-Woldengen et al., 2007
23258	75° N	14° E	1768	North-western Barents Sea margin	Sarnthein et al., 2003
PSh-5159N	71° 21.80 N	22° 38.77 E	422	South- western Barents Sea	Risebrobakken et al., 2010
MD95-2011	66° 58.19 N	7° 38.36 E	1048	Mid Norwegian Margin (Voring Plateau)	Risebrobakken et al. (2003) and Andersson et al. (2003)

Table 3: Core location, water depth, geographical area and proxy data references.

6.2 Tracing Holocene Paleoceanographic Shifts: A Cross-Regional Study in Svalbard and north Barents Sea

The analysis presented in this study, centering on core HH15-1280-GC, is primarily juxtaposed against the findings from cores NP94-51 from the Hinlopen Trough (Ślubowska et al., 2005), JM02-440 from the Bellsund Trough (Ślubowska-Woldengen et al., 2007), and NP05-11-21 from Kongsfjorden (Skirbekk et al., 2010), NP05-71-GC from Kvitøya (Kristensen et al., 2013) and ASV 880 from Franz Victoria Trough (Duplessy et al., 2005) along with several other sites (Table 3).

These comparative sites are strategically situated along the route of the WSC, which leads warm and saline AW towards the Arctic (Fig 24). Submerging beneath the sea ice and cold Arctic Water around 78°N, the AW continues as a subsurface flow along the western and northern shelves and continental slopes of Svalbard (Fig 24). Each of these locations, while subject to the inflow of AW, also encounters unique local conditions.

The Hinlopen Trough, positioned at the edge of the Arctic Ocean, is subject to polar conditions including significant annual fluctuations in sea ice cover (marginal ice zone) and the interplay of AW and Arctic water masses (Cokelet et al., 2008). Its proximity to the marginal sea-ice zone often results in a robust primary biological production (Sakshaug and Skjoldal, 1989; Falk-Petersen et al., 2000).

The southward advection of AW into the adjacent Hinlopen Strait may have been generated by intense wind-induced upwelling events at the northern Svalbard shelf like has been reported from the western Spitsbergen shelf today (Cottier et al., 2007). Lind and Ingvaldsen. (2012) reported that prevalent easterlies north of Svalbard support the upwelling of AW onto the northern shelf. This would enable a strengthened AW inflow into the Hinlopen Strait.

Contrastingly, the greater influence of AW along the western coast of Svalbard renders the waters in Kongsfjorden and Bellsund Trough largely ice-free, with only the innermost parts of the fjord experiencing frequent winter sea-ice cover (Svendsen et al., 2002; Cottier et al., 2007, 2010; Gerland and Renner, 2007). Given their proximity to tidewater glaciers, these locations are subject to higher sediment loads due to iceberg discharge and meltwater. They are also sporadically affected by colder and fresher Arctic Water (ArW) from the northward-drifting Coastal Current (CC) along the west coast of Spitsbergen (Fig 24). The CC is a continuation of

the Sørkapp Current (SC) which wraps around the southern tip of Spitsbergen (Fig 24). Despite the SC and CC being extensions of the East Spitsbergen Current (ESC), transporting ArW from the Arctic Ocean into the Barents Sea, the CC exhibits a broader range of salinities due to its interaction with water masses from fjords along the western coast of Spitsbergen (Cottier et al., 2007).

While the WSC traces the shelf slope, the CC navigates the banks and troughs on the shelf (Fig 24). The density disparity between these water masses impacts the formation and positioning of the Polar Front (Fig 24; Tverberg and Nøst, 2009). Yet, seasonal variations in frontal strength can permit AW to infiltrate the fjords of west Spitsbergen (Tverberg and Nøst, 2009). The Franz Victoria and Kvitøya are also influenced by subsurface inflow of Atlantic Water (Fig 24).

The conditions along the northern Barents Sea shelf east of Svalbard are in stark contrast to those on the western side, owing to the cold and low-salinity Arctic surface water that flows southwards out of the Arctic Ocean (ESC). The ESC passes the southern tip of Spitsbergen (Fig 24) and continues towards the north as a coastal current. The warm Atlantic Water keeps the western area of Svalbard free of sea ice year-round, while sea ice is regularly formed north, south and east of Svalbard, close to the coast and in the fjords of western Spitsbergen, where the cold Arctic Water predominates. Today, Atlantic Water passes through the Barents Sea and, after mixing and heat loss, it continues into the St. Anna Trough (Schauer et al., 2002).

6.2.1 Comparison of sedimentation rates in a regional context

In the age-model section of the thesis, the sedimentation rates observed in core HH15-1280-GC from Hinlopen Strait are compared with those from other cores (Fig 25), including NP94-51 from Hinlopen Trough, JM02-440 from Bellsund, and NP05-11-21 from Kongsfjorden. The location of core HH15-1280-GC is situated further south and inside the Hinlopen Strait, while core NP94-51 is from the shelf in Hinlopen Trough (Koç et al., 2003). The difference in latitude between these two cores suggests that they are located within distinct oceanographic and climatic settings, which may influence the observed sedimentation rates.

During the late Holocene, specifically the last 1000 yr. BP, core HH15-1280-GC exhibits sedimentation rates similar to those observed in core JM02-440 from Bellsund Trough (Ślubowska et al., 2007). Both Bellsund and Kongsfjorden are strongly influenced by Atlantic

Water at the surface (Nilsen et al., 2008; Skogseth et al., 2008). The inflow of Atlantic Water affects the local oceanographic conditions, such as temperature and salinity, and contributes to the similarities between these cores. These similarities suggest comparable environmental conditions and sedimentary processes, including reduced glacial influence, as well as similar sediment supplies and oceanographic conditions.

The core site in the Hinlopen Strait, which is predominantly under the influence of the ESC (Mangerud et al., 2002), exhibits higher sedimentation rates compared to the core sites in the western part of Svalbard, influenced by the stronger WSC (Aagaard et al., 1987).

The disparity in sedimentation rates might be a result of various environmental and geological factors. Firstly, increased melting due to warmer temperatures could be driving up sedimentation rates, as the process facilitates greater transport of sediment into the ocean.

Secondly, there could be a higher prevalence of sediment-laden sea ice or icebergs in the region, which upon melting, deposit their sediment load into the ocean, thus increasing sedimentation rates. The role of fjords and glaciers as sources of sediment must also be considered.

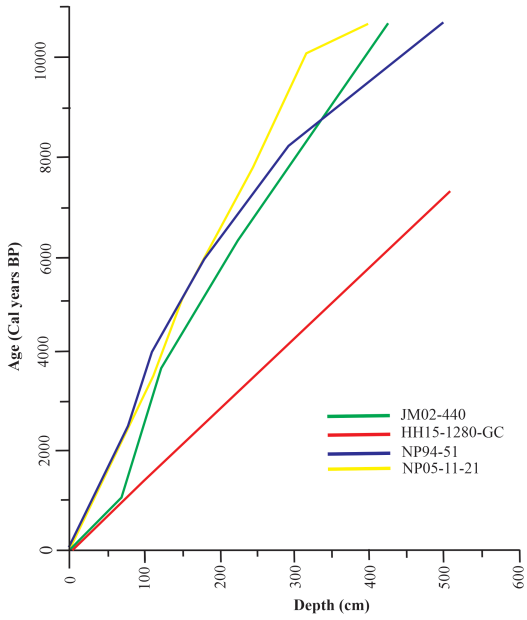

Figure 25: Age-depth models for cores HH15-1280 GC (Hinlopen Strait), NP94-51 (Hinlopen Trough), JM02-440 (Bellsund), and NP05-11-21 (Kongsfjorden) from the Svalbard area. The plot highlights the differences in sedimentation rates among the cores, with HH15-1280-GC exhibiting a higher rate compared to the others.

6.2.2 Ocean currents and benthic foraminiferal assemblages in the north Barents Sea and Svalbard area during the Holocene

This section examines the intriguing interplay between ocean currents and benthic foraminiferal assemblages in the Barents Sea and Svalbard area throughout the Holocene. The ESC and WSC present as significant forces shaping foraminiferal distribution and abundance in response to changes in water mass properties and circulation dynamics.

For a visual exploration of these changes, refer to figures 29 and 30, which showcase the distribution of dominant benthic foraminifera faunas, and figures 26, 27, and 28, which present the three dominant species in core HH15-1280-GC. Comparison with cores from the Hinlopen Trough (NP94-51; Ślubowska et al., 2005), the Bellsund Trough (JM02-440; Ślubowska-Woldengen et al., 2007), Kongsfjorden (NP05-11-21; Skirbekk et al., 2010), Kvitøya (NP05-71GC; Kristensen et al., 2013) and Franz Josef Land (ASV 880; Duplessy et al., 2001; Hald et al., 2004) allows a broader understanding of how these currents shape benthic foraminiferal distribution (Ślubowska-Woldengen et al., 2008).

The onset of the mid-Holocene (c. 7300 cal yr. BP) reveals a fascinating shift. The slow increase of *E. excavatum* in the Hinlopen Strait and its rapid rise at other sites are mirrored in records from the entire Svalbard and north Barents Sea region (Duplessy et al., 2001; Hald et al., 2004; Ślubowska -Woldengen et al., 2007; Skirbekk et al., 2010; Rasmussen et al., 2012; Kristensen et al., 2013). This trend likely indicates a regional hydrographic shift affecting all locations at the north (western) Barents Sea margin, possibly triggered by a weakening of the AMOC at c. 7000 cal yr. BP (Solignac et al., 2004). Sarnthein et al. (2003) documented a sub sea-surface temperature drop of ~3 °C at the western Barents slope at around 7700 cal yr. BP, which was probably linked to a weakening of the WSC (Fig 26).

Post 7700 cal yr. BP, a parallel decrease of *N. labradorica* is observed across all studies around Svalbard, suggesting retreating oceanic fronts and/or a diminishing influence of AW, along with a related productivity drop (Ślubowska et al., 2005; Rasmussen et al., 2012). Only at the easternmost site (Hinlopen Strait and Franz Josef Land), percentages of *N. labradorica* (as well as *Buccella* spp) increased synchronously with percentages of *E. excavatum*. This has been linked to an approaching sea-ice edge and a related productivity increase (Duplessy et al., 2001; Kristensen et al., 2013).

Further, during the mid-late Holocene, there's a noted decrease in percentage of *N. labradorica* with some small peaks observed at 300 cal yr. BP for Kongsfjorden and Hinlopen Trough, indicating a possible retreat of the Polar Front to the core site in Hinlopen Strait.

In all cores, the percentage of *E. excavatum* increases, indicating a deterioration of environmental conditions in all areas and over the Svalbard and north Barents Sea region. This significant climatic shift is observed through the simultaneous decline of Atlantic Water influence, and an increased glacial impact, indicating a colder environment (Skirbekk et al., 2010).

The specific distribution patterns of *C. reniforme* and *E. excavatum*, both of which are associated with the front of glaciers and termed 'ice-proximal' faunas (Hald and Korsun, 1997), provide crucial information about the environmental dynamics. It's interesting to observe that *C. reniforme* tends to dominate over *E. excavatum* in less stressed environments, where food supply is more abundant, and the glacial influence is reduced (Korsun and Hald, 1998).

The early Holocene presents a distinct picture, with *C. reniforme* dominating in Bellsund Trough, Kongsfjorden, Kvitøya, Franz Viktoria Trough and Hinlopen Trough (Fig 27). Coupled with the absence of *E. excavatum*, low IRD flux, and high concentration of benthic foraminifera, these factors indicate a strong influence of Atlantic water masses at the core sites, pointing to a period of significant climatic improvement. After 6000 cal yr. BP the influence of Atlantic Water diminished, as inferred from the higher content of *E. excavatum* and a slight increase in ice-rafted debris (Fig 28).

Fast forward to the late Holocene, and the scenario changes. In Kongsfjorden, we see *E. excavatum* increasing its dominance, a development that alongside an increased IRD flux and a noticeable decrease in productivity, paints a picture of a colder environment with a stronger glacial influence (Skirbekk et al., 2010).

In the Hinlopen Strait, is seen an increase in the percentage of *E. excavatum* during the late Holocene at c. 2700 cal yr. BP and 1600 cal yr. BP. This increase correlates well with the lower abundance of planktic foraminifera, further reinforcing the notion of deteriorating environmental conditions.

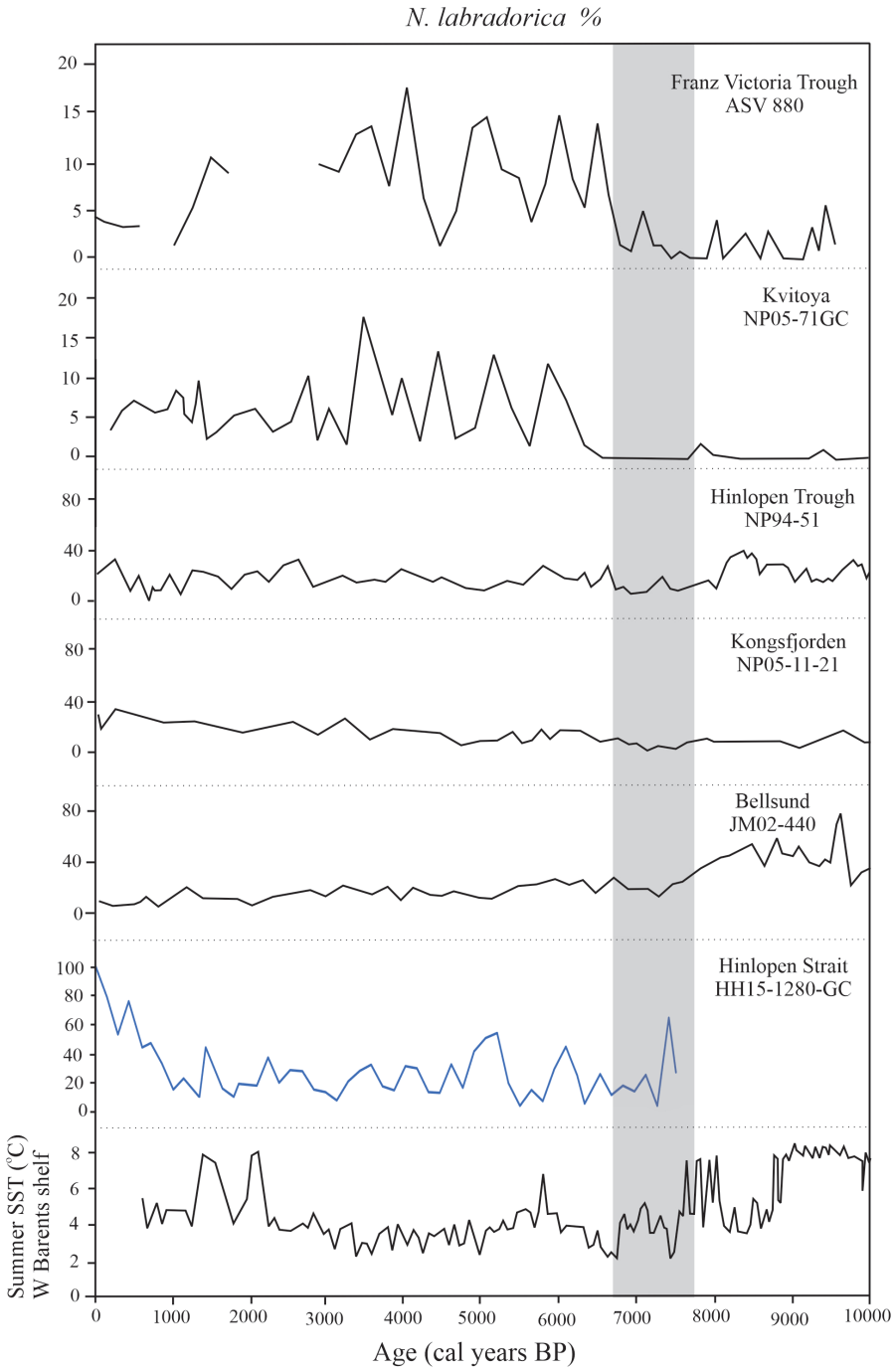

Figure 26: Comparative distribution of *N. Labradorica* species in the Svalbard and north Barents Sea area. Hinlopen Strait (HH15-1280-GC; this study), Hinlopen Trough (NP94-51; Ślubowska et al., 2005), Bellsund Trough (JM02-440; Ślubowska-Woldengen et al., 2007), Kongsfjorden Trough (NP05-11-21; Skirbekk et al., 2010), Kvitøya (NP05-71-GC; Kristensen et al., 2013) and Franz Victoria Trough (ASV 880; Duplessy et al., 2005). Summer (sub) surface temperatures at the western Barents slope (23258; Sarnthein et al., 2003). Highlighted area marks timespan of faunal shift including the timing discrepancies between records.

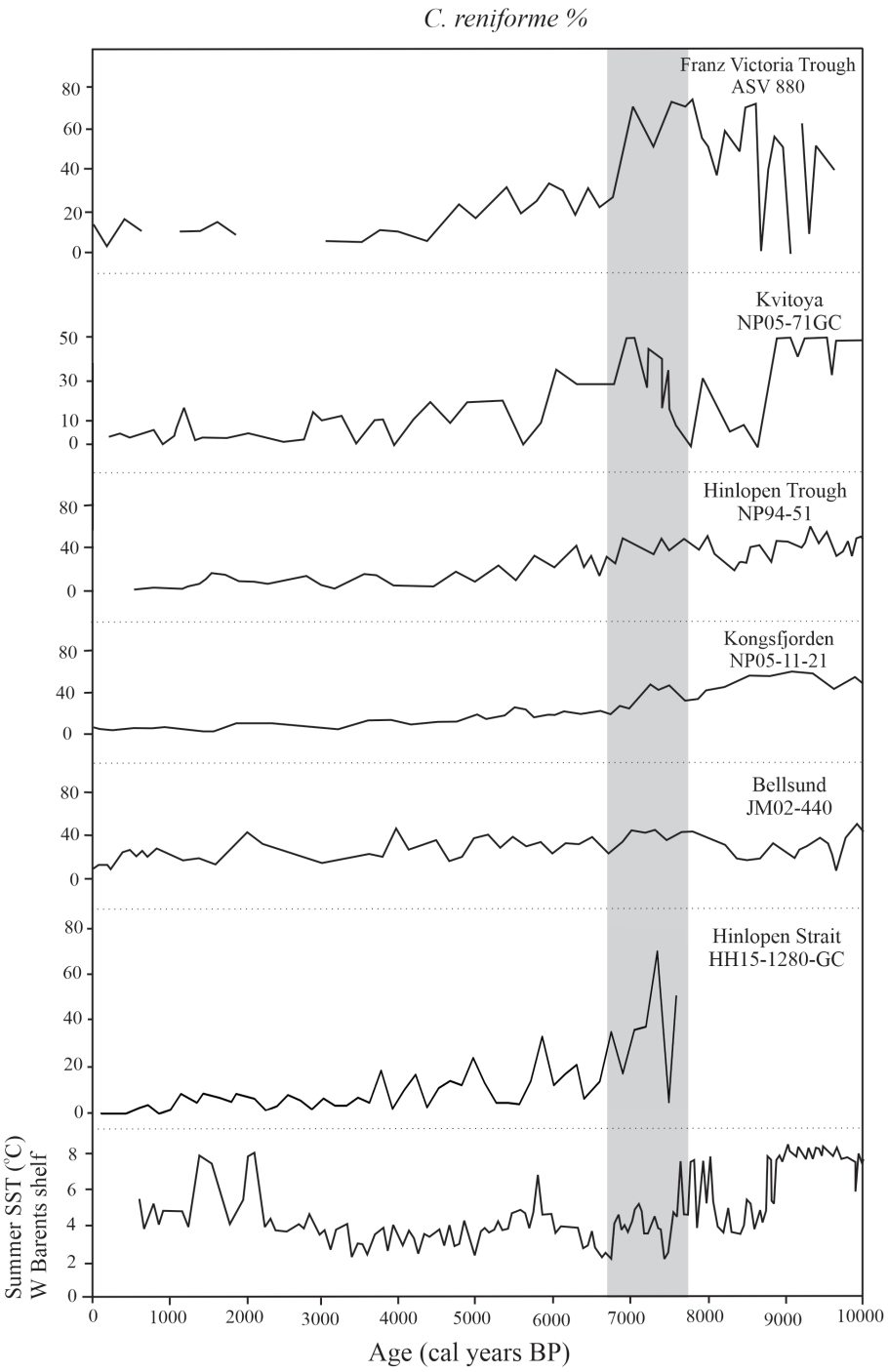

Figure 27: Comparative distribution of *C. reniforme* species in the Svalbard and north Barents Sea area. Hinlopen Strait (HH15-1280-GC; this study), Hinlopen Trough (NP94-51; Ślubowska et al., 2005), Bellsund Trough (JM02-440; Ślubowska-Woldengen et al., 2007), Kongsfjorden Trough (NP05-11-21; Skirbekk et al., 2010), Kvitøya (NP05-71-GC; Kristensen et al., 2013) and Franz Victoria Trough (ASV 880; Duplessy et al., 2005). Summer (sub) surface temperatures at the western Barents slope (23258; Sarnthein et al., 2003). Highlighted area marks timespan of faunal shift including the timing discrepancies between records.

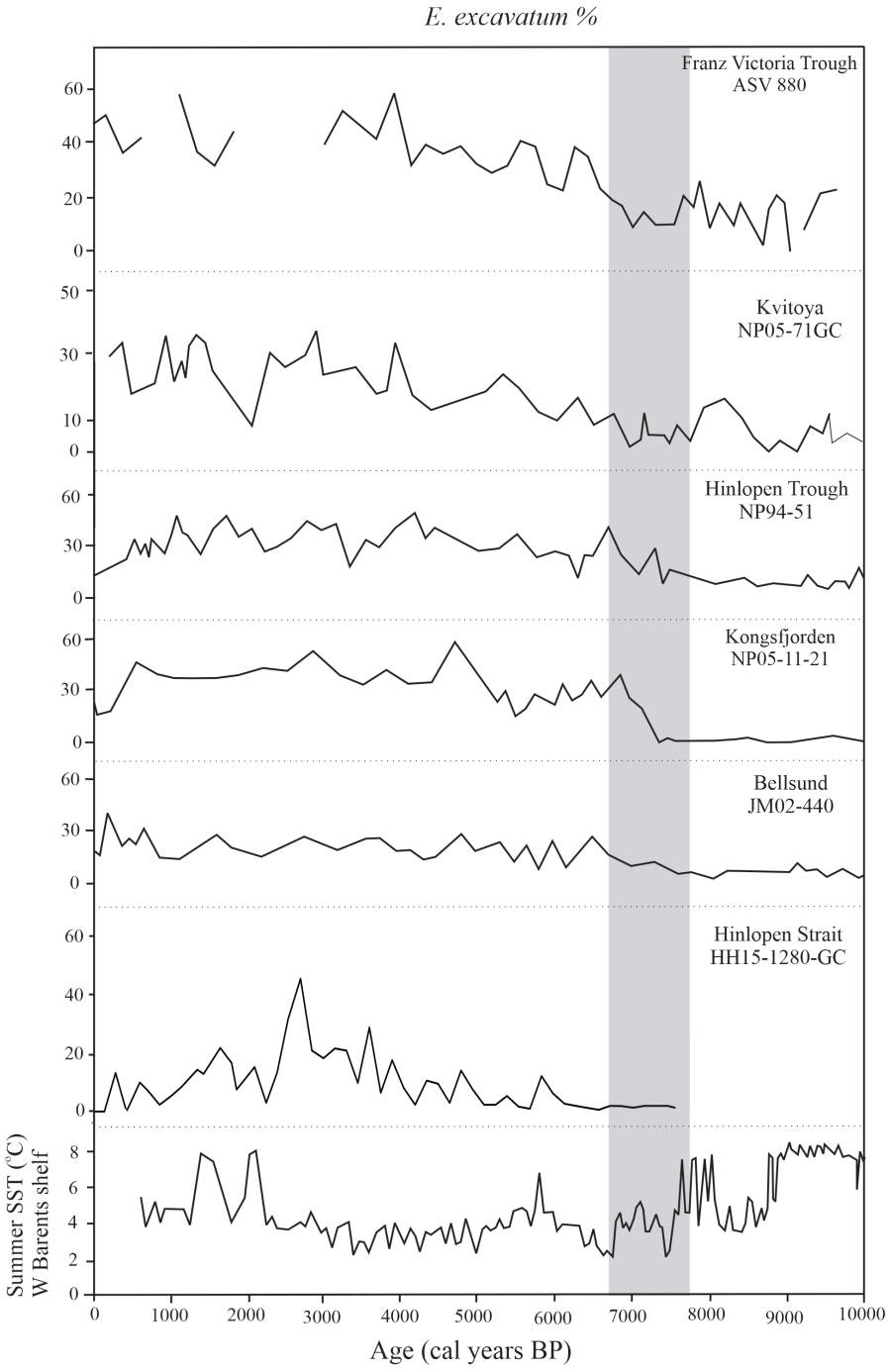

Figure 28: Comparative distribution of *E. excavatum* species in the Svalbard and north Barents Sea area. Hinlopen Strait (HH15-1280-GC; this study), Hinlopen Trough (NP94-51; Ślubowska et al., 2005), Bellsund Trough (JM02-440; Ślubowska-Woldengen et al., 2007), Kongsfjorden Trough (NP05-11-21; Skirbekk et al., 2010), Kvitøya (NP05-71-GC; Kristensen et al., 2013) and Franz Victoria Trough (ASV 880; Duplessy et al., 2005). Summer (sub) surface temperatures at the western Barents slope (23258; Sarnthein et al., 2003). Highlighted area marks timespan of faunal shift including the timing discrepancies between records.

Figures 29 and 30 take a closer look at the mid-Holocene (7000-5000 cal yr. BP) and late Holocene (4000-2000 cal yr. BP) periods in the Svalbard region, focusing on the shifts in ocean currents and their influence on benthic foraminiferal assemblages. The mid-Holocene period (7000-5000 cal yr. BP) shows an initial amplification of the ESC and its branches in the Svalbard region. This is represented by an increase in cold-water species, such as *C. reniforme*, suggesting a stronger presence of colder Atlantic waters (Ślubowska-Woldengen et al., 2008). However, towards 5000 cal yr. BP, a decrease in these species hints at a diminishing ESC influence, possibly making way for warmer AW carried by the WSC to permeate deeper into the study area.

Conversely, during this time, the WSC demonstrates a reduced influence at the start but strengthens over the period. The increasing frequency of *M. barleeanus*, a species associated with warmer water masses, implies a gradual rise in the WSC's influence (Ślubowska-Woldengen et al., 2008). These trends are corroborated by studies such as Rasmussen et al. (2014) and Sztybor and Rasmussen. (2017), which report similar shifts in the Svalbard region's oceanographic conditions and benthic foraminiferal assemblages.

The late Holocene period (4000-2000 cal yr. BP) shows an amplified influence of the ESC compared to the mid-Holocene. This is denoted by a higher prevalence of cold-water species like *I. norcrossi*, indicative of an increased sea-ice presence (Ślubowska-Woldengen et al., 2008). A surge in *E. excavatum* until approximately 3000 cal yr. BP further suggests a regional cooling of the Atlantic Water in the Nordic Seas, as supported by various marine records (Eiriksson et al., 2006; Jennings et al., 2002; Knudsen et al., 2004; Hald et al., 2004; Duplessy et al., 2001).

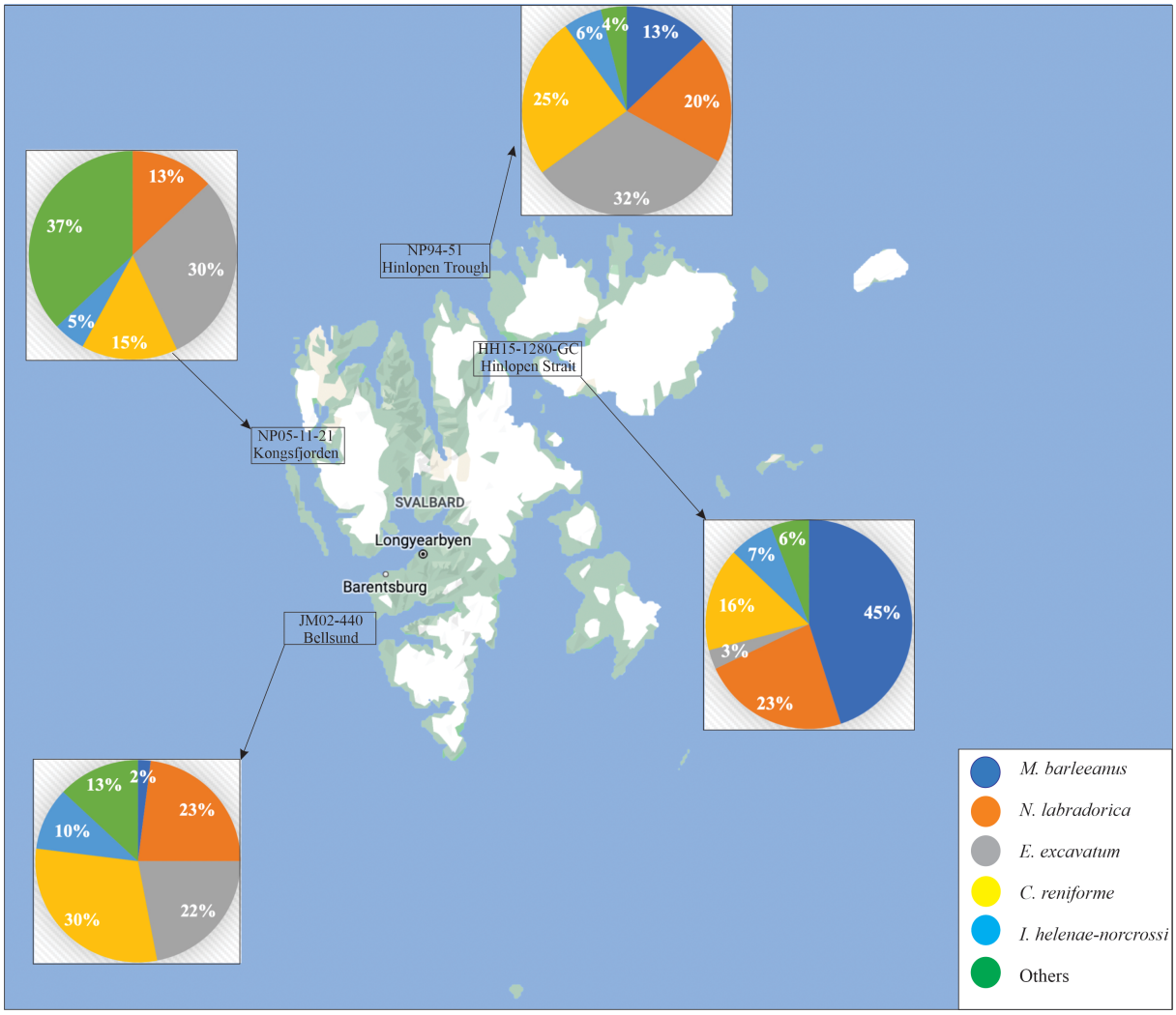

Figure 29: Benthic foraminiferal assemblages in the Svalbard region influenced by the East Spitsbergen Current (ESC) and West Spitsbergen Current (WSC) during the mid-Holocene (7000-5000 cal years BP).

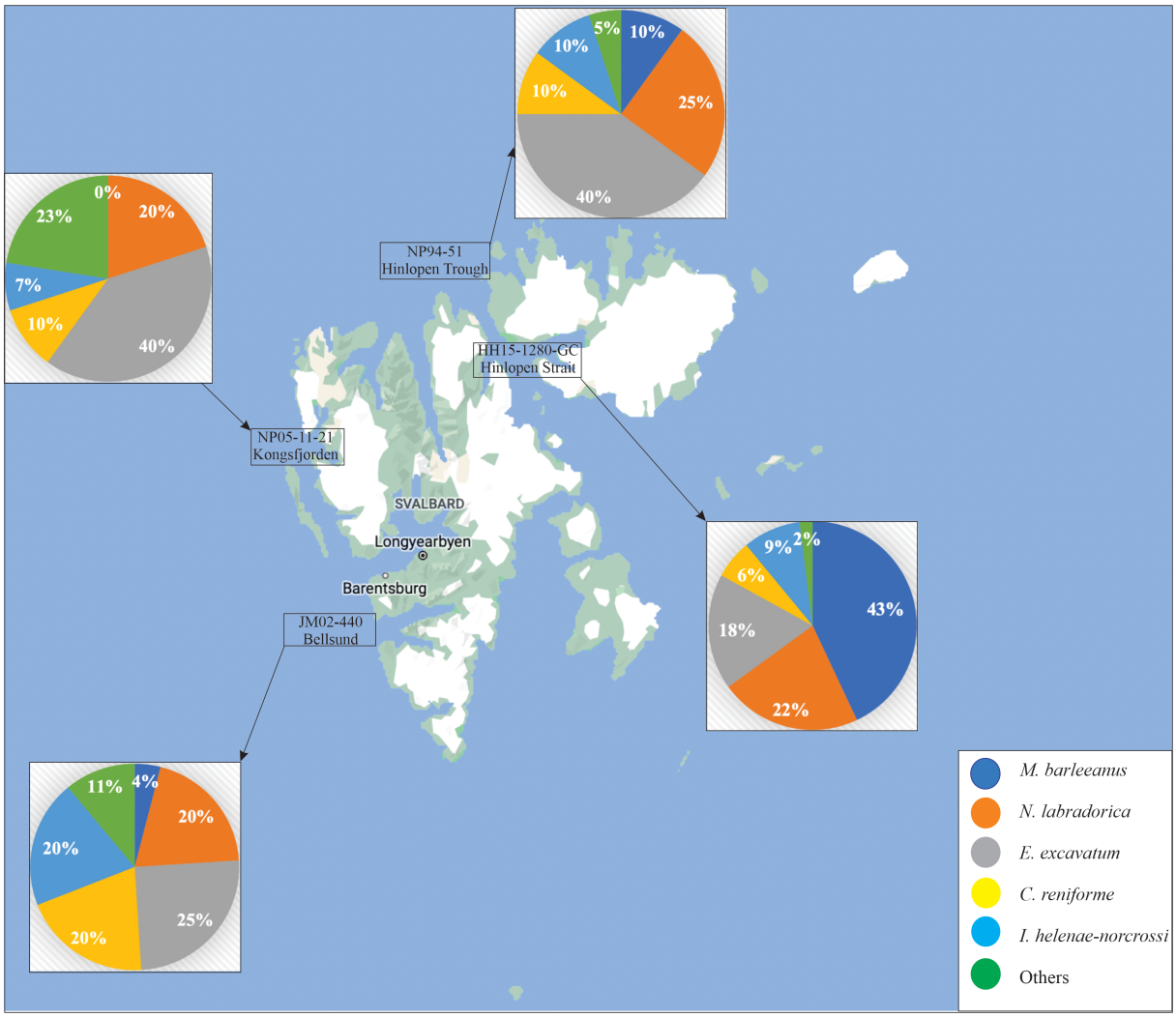

Figure 30: Benthic foraminiferal assemblages in the Svalbard region influenced by the East Spitsbergen Current (ESC) and West Spitsbergen Current (WSC) during the late Holocene (4000-2000 cal years BP).

6.2.3 Comparison of $\delta^{18}O$ records between core HH15-1280-GC (Hinlopen Strait) and cores from Svalbard

The $\delta^{18}O$ records of core HH15-1280-GC from the Hinlopen Strait, core NP94-51 from the Hinlopen Trough (Ślubowska et al.,2005), JM02-440 from Bellsund Trough (Ślubowska-Woldengen et al., 2007) and NP05-11-21 from Kongsfjorden (Skirbekk et al., 2010), beautifully align in a comparative illustration presented in figure 31.

Notably, the Hinlopen Strait values generally supersede those from the Hinlopen Trough, Bellsund Trough, and Kongsfjorden until about 3000 cal yr. BP. Thereafter, they show a convergence, especially with Kongsfjorden. The differences between these sites may stem from variations in the measured foraminiferal species (*N. labradorica* for Hinlopen Strait and *M.*

barleeanus for other sites), species-specific isotopic fractionation, or the differing rates of sea-ice melting and freshwater release in regions characterized by perennial pack ice (Łącka et al., 2015). Moreover, the lower values from the Hinlopen Trough could hint at the influence of the warm North Svalbard Branch current on the core site (Ślubowska-Woldengen et al., 2008).

Interestingly, the Hinlopen Strait exhibits a warmer late Holocene compared to the other sites, likely due to strong stratification. This closeness of values further enhances our understanding of the region's climatic history.

Key periods of climate change are detected across the cores. A sharp decrease in $\delta^{18}O$ event is discernible in the mid Holocene (7000-6600 cal yr. BP) for Hinlopen Strait, Kongsfjorden, and Bellsund Trough, albeit less pronounced in the Hinlopen Trough. A warming event, particularly sharp in the Kongsfjorden site, emerges between 6600-5600 cal yr. BP across all sites. In figure 32, a cooling event around 7000-6000 cal yr. BP is visible in summer surface temperature records from the north-west and south-west Barents Sea. As is depicted in figure 32 the cooling event is smaller in southern records which can be due to reduced insolation from north to south.

The mid-Holocene cooling observed in the Barents Sea and Svalbard is also recorded and reported by Birks and Koç. (2002) at lower latitude on the Vøring Plateau (Fig 32), where an SST reconstruction exhibits also a gentle cooling trend between 6700 and 4700 cal yr. BP. The diatom record of Birks and Koç. (2002) also shows that at the same time, the assemblage associated with the North Atlantic Water decreased, whereas that of Norwegian-Atlantic Water began to increase continuously for 2000 years. This trend is similar to the small warming depicted by the $\delta^{18}O$/temperature records of *N. pachyderma* in the north Barents Sea core (ASV 880; Duplessy et al., 2005). This observation suggests that the broad intense warm Atlantic current, which fed directly the Nordic seas during the thermal optimum (Koç et al., 1993), was suddenly reduced by 6700 cal yr. BP and did not reach any more the Barents Sea anymore.

An anomalous localized elevation in $\delta^{18}O$ values is noted in the Hinlopen Strait during the time span of 4600-4200 cal yr. BP. Concurrently, a decreasing trend in $\delta^{18}O$ values is seen in other locations, while sea surface temperature (SST) and bottom water temperature (BWT) records from the Barents Sea and Svalbard indicate an increase in temperature. This unique pattern observed in the Hinlopen Strait might potentially be ascribed to an enhanced influx of meltwater originating from sea ice or glaciers in the vicinity.

In the Nordic Seas and western Norwegian margin between 2800 and 2600 cal yr. BP the strongest Holocene solar irradiance minimum occurred (Renssen et al., 2012; Vonmoos et al., 2006) that this event is visible in our data around 3100 cal yr. BP.

After 3000 cal yr. BP the water column in Svalbard and Barents Sea became more stratified and the deep convection and inflow of AW did not recover. After 2000 cal yr. BP inflow of the AW enhanced into the core sites despite the orbitally forced cooling of the surface water (Calvo et al., 2002), it led to a subsurface warming. The warming can be observed in records from across the entire region (Andersen et al., 2004; Giraudeau et al., 2010; Hald et al., 2007; Risebrobakken et al., 2011; Werner et al., 2013).

The Roman Warm Period is detected across all cores at 2200-1800 cal yr. BP. This warm period is depicted as two M-shaped excursions which also is known from the North GRIP ice core from northern central Greenland inland ice (Johansen et al., 2001), from core MD95-2011(Vøring Plateau; Risebrobakken et al., 2003; Andersson et al., 2003) and core 23258 (NW Barents Sea margin; Sarnthein et al., 2003). This event is also marked by low IRD content in Bellsund (Ślubowska-Woldengen et al. 2007) and Hinlopen Strait (Fig 33).

A striking increase in $\delta^{18}O$ values between 1400 and 1000 cal yr. BP in Hinlopen Strait and Kongsfjorden cores coincides with high amounts of IRD content (Fig 33) content and *I. helenae/norcrossi*, indicating an escalation in iceberg activity and ice activity - this is in alignment with the Dark Age Cold Period (DACP) event. Interestingly, the same event occurs earlier in Hinlopen Trough and Bellsund Trough (2000-1800 cal yr. BP). Deposition of IRD increased gradually through the period 1400-1000 cal yr. BP as the surface water became colder during summers (Hald et al., 2007; Risebrobakken et al., 2011) (Fig 32), indicating that transported sea ice reached the site before melting, possibly because of the colder summer surface water (Fig 33).

A decline in $\delta^{18}O$ levels from 800 to 400 cal yr. BP across all cores is consistent with the Medieval Warm Period (MWP), characterized by warmer temperatures and the presence of Atlantic Water in the Arctic Ocean. This event is well pronounced in SST record from core 23258 (NW Barents Sea margin; Risebrobakken et al., 2010) and PSh-5159N (SW Barents Sea; Risebrobakken et al., 2011).

Finally, the Little Ice Age (LIA), which was centered around 300 cal yr. BP, marked a phase of cooling and glacier expansion in the Northern Hemisphere (Nesje et al., 2008). This event took

place when reduced summer insolation coincided with periods of minimal solar activity. Evidence of the LIA is observable in all core samples, as indicated by a decrease in $\delta^{18}O$ values (Fig 31) and lower SST in Barents Sea cores (Fig 32). The LIA, dated at 300 cal yr. BP in both Hinlopen Strait and Kongsfjorden cores, corresponds with increased IRD content particularly in Kongsfjorden core (Fig 33). Additionally, the presence of *I. helenae/norcrossi* suggests an increase in iceberg and ice activity.

The observed variations in $\delta^{18}O$ values between the cores could be a product of a myriad of factors, including varying influences of AW and ArW, atmospheric circulation patterns, and iceberg presence (Ślubowska-Woldengen et al., 2007; Rasmussen et al., 2014).

Mayewski et al. (2004) conducted an exhaustive study of over fifty paleoclimatic records from diverse global locations. Their findings delineated six significant periods of abrupt climate alterations occurring during the intervals 9000-8000, 6000-5000, 4200-3800, 3500-2500, 1200-1000, and 600-150 cal yr. BP. The majority of these climate perturbations, as derived from the globally distributed data, were marked by a pattern of intensified polar cooling, increased tropical aridity, and substantial shifts in atmospheric circulation dynamics.

Contrarily, the cooling episode identified around 6600 cal yr. BP in the present study does not appear to correlate directly with the global phenomena as characterized by Mayewski et al. (2004). This suggests that the observed cooling event may be of a more local/regional character, potentially limited to the Svalbard margin and the Barents Sea area. This observation underscores the intricate and heterogeneous nature of climatic changes, manifesting variability across global and regional scales.

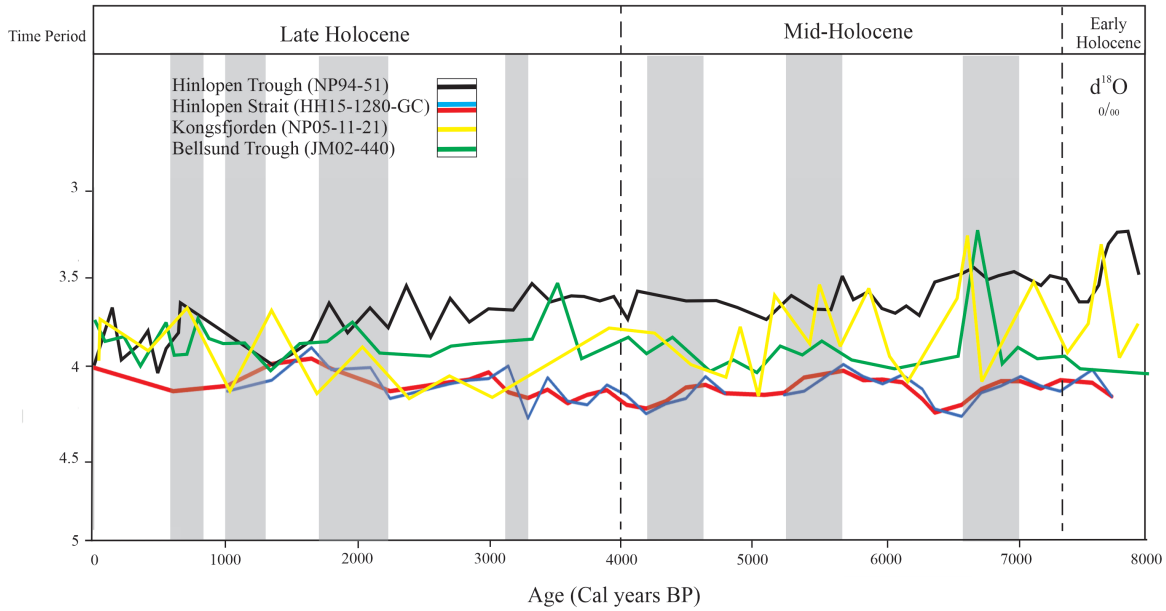

Figure 31: Comparison of $\delta^{18}O$ records from core HH15-1280-GC in the Hinlopen Strait (blue and red lines) and core NP94-51 from the Hinlopen Trough (black line) (Ślubowska et al., 2005), NP05-11-21 from Kongsfjorden (yellow line) (Skirbekk et al., 2010) and JM02-440 from Bellsund Trough (green line) (Ślubowska-Woldengen et al., 2007).

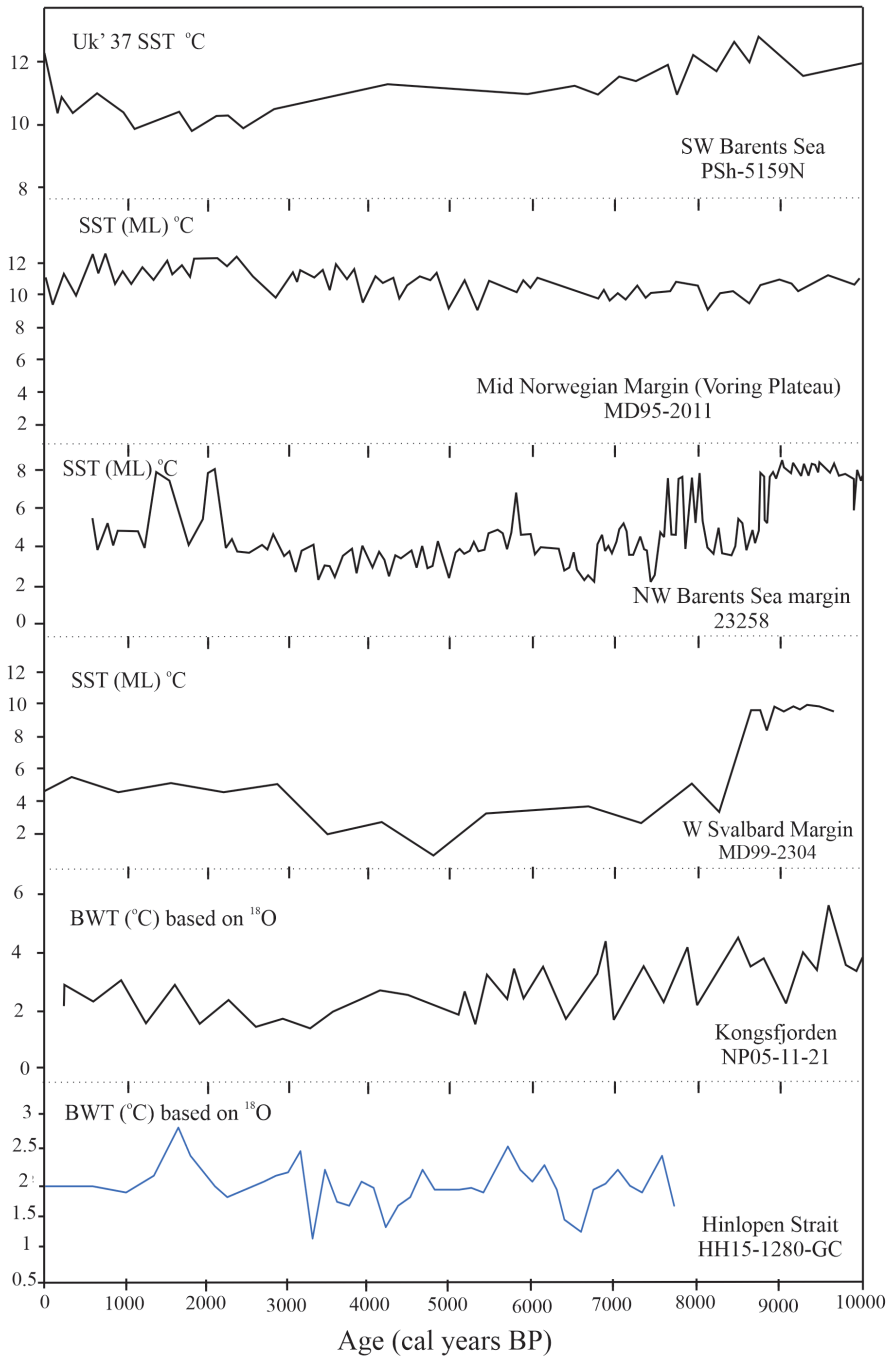

Figure 32: Reconstructed Sea surface summer temperature (SST-ML) based on a planktonic foraminiferal transfer function using the maximum likelihood statistical method in the sediment cores on the Norwegian-Barents Sea-Svalbard margin by Hald et al. (2007), alkenone SST from south-west Barents Sea (Risebrobakken et al., 2010) and bottom water temperature (BWT) based on $\delta^{18}O$ benthic foraminifera from Hinlopen Strait (this study) and Kongsfjorden (Rasmussen et al., 2014).

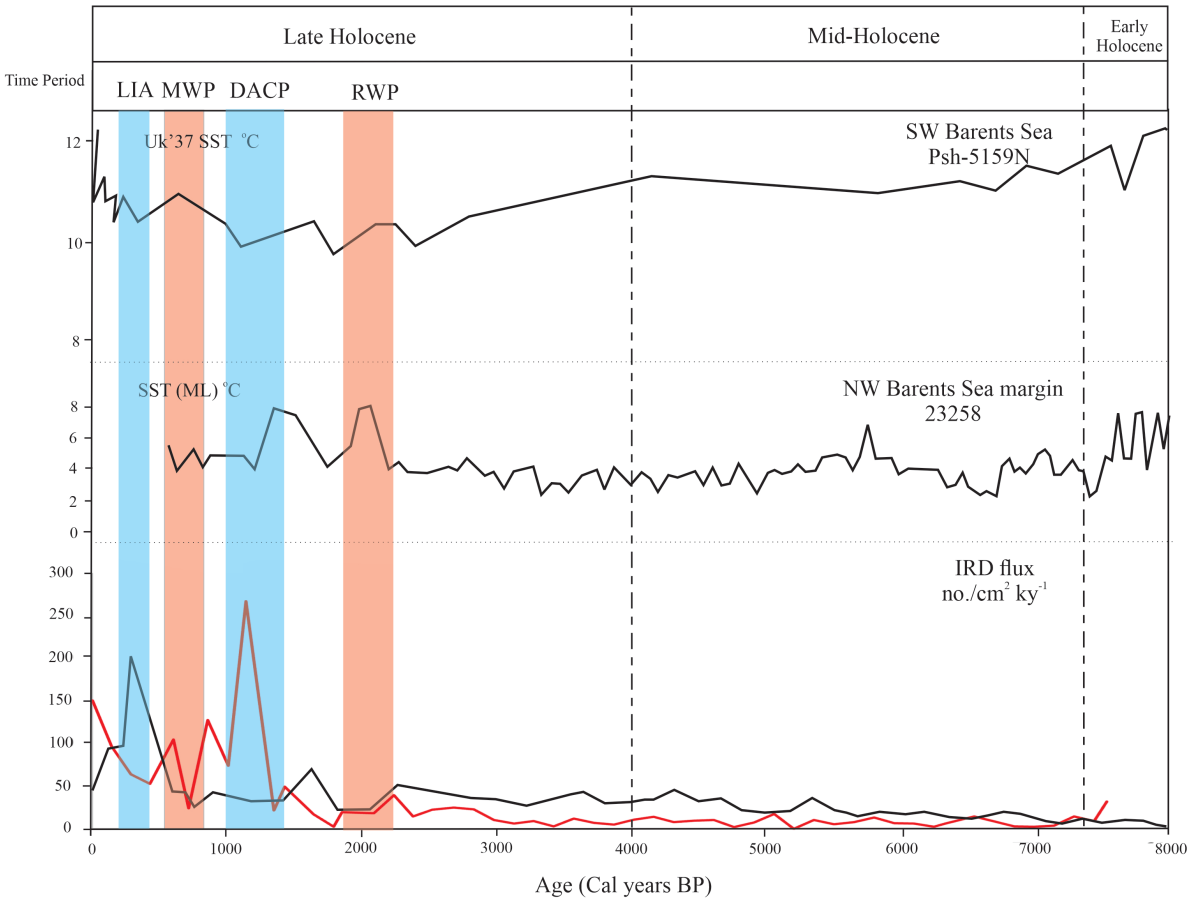

Figure 33: Flux of IRD between the Hinlopen Strait core (HH15-1280-GC), represented by the red line, and the Bellsund core (JM02-440), represented by the black line. It also includes an alkenone-based Sea Surface Temperature (SST; Risebrobakken et al., 2011) from the SW Barents Sea, and planktonic SST from the NW Barents Sea (Hald et al., 2007). The highlighted periods illustrate the Roman Warm Period (RWP), Dark Ages Cold Period (DACP), and the Medieval Warm Period (MWP).

6.2.4 Holocene Sortable Silt Comparison: South-West Spitsbergen vs. Hinlopen Strait/Northern Svalbard

The first sortable silt (SS) study from the Hinlopen Strait was compared to an SS study conducted on a core from the south-west Spitsbergen region outer continental shelf (76°53.660 N, 14°41.170 E) at 148 m water depth (Sternal et al., 2014). The choice of this core was based on the fact that both study areas are influenced by the ESC and WSC. The two studies revealed a similar trend, particularly in the late and mid Holocene (Fig 34). However, SSmean values in the south-west Spitsbergen region were higher than those observed in the Hinlopen Strait, suggesting stronger near-bottom current speeds. This difference in SS values and current strength was more pronounced during the early Holocene. The higher SS% values and stronger

currents off south-west Spitsbergen during the early Holocene period may also reflect regional differences in oceanographic and climatic conditions at the time (Mangerud et al., 2004), as compared to the conditions in the Hinlopen Strait and Northern Svalbard.

For example, the south-west Spitsbergen region experienced a more rapid retreat of sea ice during the Early Holocene (Ślubowska-Woldengen et al., 2008), while the Hinlopen Strait and Northern Svalbard had a more gradual reduction in sea-ice cover (Rasmussen et al., 2014). The presence of less sea ice in south-west Spitsbergen could have led to enhanced wind-driven mixing and circulation (Polyak et al., 2010), which in turn could have increased the near-bottom current speeds and the corresponding SS values in south-west Spitsbergen, relative to the Hinlopen Strait and Northern Svalbard.

Furthermore, differences in freshwater input from meltwater could also play a role in the observed differences in SS values between the two regions. The south-west Spitsbergen region likely experienced a greater influx of meltwater from the retreating ice sheets during the Early Holocene (Bauch et al., 2001), while the Hinlopen Strait and Northern Svalbard had comparatively lower meltwater inputs (Rasmussen et al., 2014). This difference in meltwater input could have created stronger buoyancy-driven circulation in the south-west Spitsbergen region, leading to higher SS values compared to the Hinlopen Strait and Northern Svalbard.

Lastly, variations in ocean circulation patterns could have contributed to the observed differences in SS values between the two regions. During the early Holocene, the south-west Spitsbergen region experienced a stronger influence of AW due to the northward shift of the Subpolar Front. In contrast, the Hinlopen Strait and Northern Svalbard were under the influence of the ESC and had a reduced AW influence during the same period (Cottier et al., 2010; Rasmussen et al., 2014). The inflow of warmer and saltier AW in the south-west Spitsbergen region might have resulted in more vigorous circulation, leading to higher SS values compared to the Hinlopen Strait and Northern Svalbard, where the ESC-driven circulation was relatively weaker.

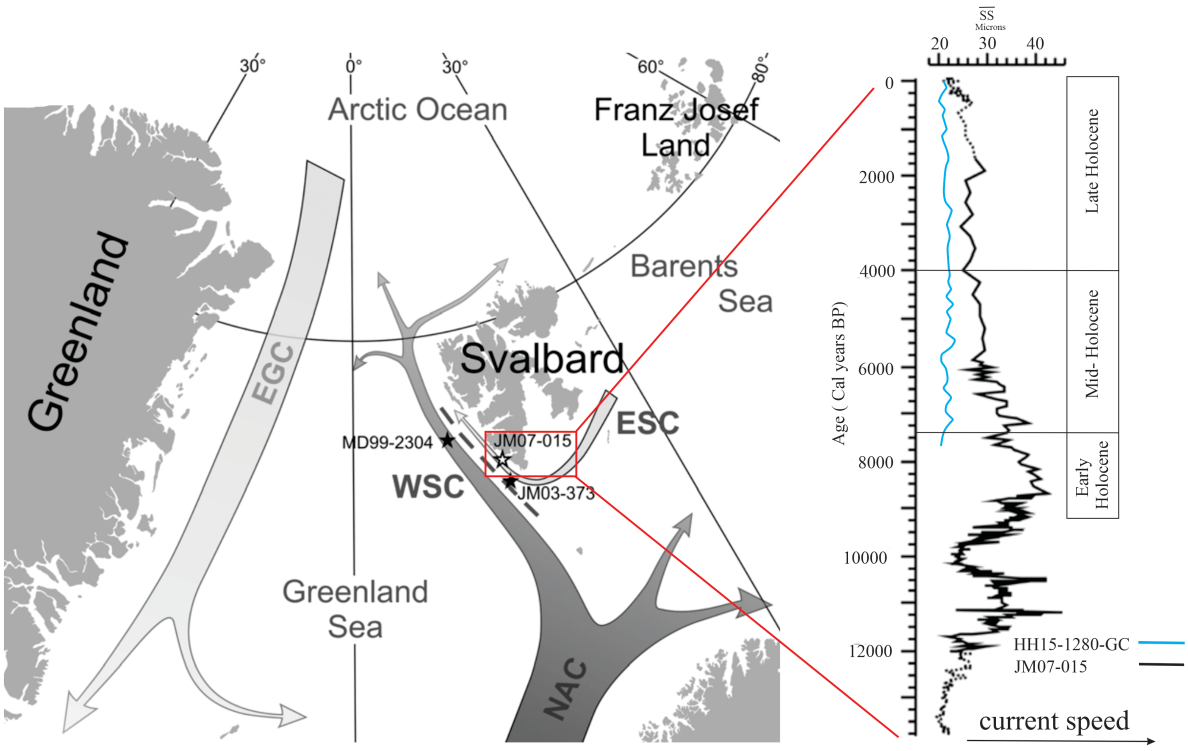

Figure 34: A comparison of sortable silt (SS) data from the first study in the Hinlopen Strait (blue line) with SS data from the south-west Spitsbergen region (Sternal et al., 2014) (black line).

6. Discussion and Correlation

7. Summary and Conclusions

The sediment core HH15-1280-GC retrieved in the Hinlopen Strait, northern Svalbard, has been investigated to reconstruct the climatic evolution and ocean circulation during the early-late Holocene covering the last 8000 years. Climatic changes occurring on the western and northern margins of Svalbard may affect the whole Artic, making it a particularly interesting area of study.

- The depositional environment during the Holocene was strongly dominated by rapid sediment rainout from the water column and occasional deposition of Ice-rafted debris (IRD) from icebergs or sea ice in a relatively weak ocean current regime in an ice-distal environment.

- At c. 7700 calibrated years Before Present (cal yr. BP) a rapid hydrographic shift is reflected in the foraminiferal fauna: Arctic Water (ArW) replaced the dominant influence of Atlantic Water (AW) possibly triggered by a weakened Atlantic Meridional Overturning Circulation (AMOC).

- The mid-Holocene is characterized by several cooling events, where inflow of ArW of the East Spitsbergen Current (ESC) influences the sea surface.

- The mid-Holocene (7300-4000 cal yr. BP) represents a transition period with generally relative stable environmental conditions. Increasing deposition of IRD indicates sea ice and icebergs arriving at the core site and is probably related to decrease in sea surface temperature. Planktic foraminiferal data show increasing abundances in this period. The dominant benthic species *Cassidulina neoteretis* and *Melonis barleeanus* which are linked to chilled AW and indicate continuous inflow of AW.

- At c. 6600 cal yr. BP, the advection of AW decreased rapidly. This was probably related to the intensification of the ESC, resulting increased inflow of Polar Water (PW) and subduction of AW under ArW as well as enhanced cooling and sea-ice delivery from the Arctic.

- A deterioration of the environment with decreased salinities due to reduced inflow of Atlantic Water and a stronger dominance of Arctic Waters, reflected by increased abundance of *E. excavatum* and a reduction of *C. reniforme*, characterized the late Holocene (c. 4000 cal yr. BP).

- The reconstruction of current strength based on the SS proxy suggests that during 5600-5100 cal yr. BP as well as 2800-2200 cal yr. BP, near-bottom currents were at their strongest. In contrast, the periods between 6600-5500 and 700-400 cal yr. BP are marked by the slowest currents.

- In the late Holocene climatic conditions became cooler. The dominant benthic species *I. helenae/norcrossi* indicate cooling of the bottom water. The decreasing trend in temperature continues during the late Holocene and the influence of Atlantic Water in the area diminished further.

- An extended sea ice cover probably caused a decoupling of atmospheric and hydrographic conditions during the late Holocene (c. 3200 to present): while glaciers probably expanded due to the decreased summer insolation and resulting colder atmospheric temperatures, bottom waters warmed, possibly as a result of the stronger water stratification.

- The data from Hinlopen Strait generally display regional changes that are correlative with studies from the Svalbard-Barents Sea area and eastern Nordic Seas. It suggests

that an east-west climatic gradient, similar to today, existed between eastern and western Svalbard, the eastern Nordic Seas and the northern Barents Sea in the early-mid Holocene.

8. References

8. References

1. Aagaard, K. & Carmack, E.C. 1989, 'The role of sea ice and other freshwater in the Arctic circulation', Journal of Geophysical Research: Oceans, vol. 94, no. C10, pp. 14485-14498.

2. Aagaard, K., Coachman, L.K. & Carmack, E. 1981, 'On the halocline of the Arctic Ocean', Deep Sea Research Part A. Oceanographic Research Papers, vol. 28, no. 6, pp. 529-545.

3. Aagaard, K., Foldvik, A. and Hillman, S.R., 1987. The West Spitsbergen Current: disposition and water mass transformation. Journal of Geophysical Research: Oceans, 92(C4), pp.3778-3784.

4. Alley, R.B. 2007, 'Wally was right: Predictive ability of the North Atlantic "conveyor belt" hypothesis for abrupt climate change', Annual Review of Earth and Planetary Sciences, vol. 35, pp. 241-272.

5. Alley, R.B., Mayewski, P.A., Sowers, T., Stuiver, M., Taylor, K.C. & Clark, P.U. 1997, 'Holocene climatic instability: A prominent, widespread event 8200 yr. ago', Geology, vol. 25, no. 6, pp. 483-486.

6. Alve, E., Korsun, S., Schönfeld, J., Dijkstra, N., Golikova, E., Hess, S., Husum, K. and Panieri, G., 2016. Foram-AMBI: A sensitivity index based on benthic foraminiferal faunas from North-East Atlantic and Arctic fjords, continental shelves and slopes. Marine Micropaleontology, 122, pp.1-12.

7. Andersen, C., Koç, N. and Moros, M., 2004. A highly unstable Holocene climate in the subpolar North Atlantic: evidence from diatoms. Quaternary Science Reviews, 23(20-22), pp.2155-2166.

8. Andersson, C., Risebrobakken, B., Jansen, E. and Dahl, S.O., 2003. Late Holocene surface ocean conditions of the Norwegian Sea (Vøring Plateau). Paleoceanography, 18(2).

9. Andreassen, K. and Winsborrow, M., 2009. Signature of ice streaming in Bjørnøyrenna, Polar North Atlantic, through the Pleistocene and implications for ice-stream dynamics. Annals of Glaciology, 50(52), pp.17-26.

10. Andreassen, K., Laberg, J.S. and Vorren, T.O., 2008. Seafloor geomorphology of the SW Barents Sea and its glaci-dynamic implications. Geomorphology, 97(1-2), pp.157-177.

11. Armstrong, H. and Brasier, M., 2013. Microfossils. John Wiley & Sons.

12. Armstrong, H., i Brasier, M. (2005). Microfossils, Second Edition, Blackwelll, pp.142-184.

13. Bakke, J., Lie, Ø., Nesje, A., Dahl, S.O. and Paasche, Ø., 2005. Utilizing physical sediment variability in glacier-fed lakes for continuous glacier reconstructions during the Holocene, northern Folgefonna, western Norway. The Holocene, 15(2), pp.161-176.

14. Barker, S., Greaves, M. and Elderfield, H. 2003, 'A study of cleaning procedures used for foraminiferal Mg/Ca palaeothermometry', Geochemistry, Geophysics, Geosystems, vol. 4, no. 9, 8407.

15. Bartels, M., Titschack, J., Fahl, K., Stein, R., Seidenkrantz, M.-S., Hillaire-Marcel, C. & Hebbeln, D. 2018, 'Wahlenbergfjord, eastern Svalbard: a glacier-surrounded fjord reflecting regional hydrographic variability during the Holocene', Boreas, vol. 47, no. 1, pp. 66-83.

16. Bauch, D., Erlenkeuser, H. & Spielhagen, R.F. 2001, A multiproxy reconstruction of the evolution of deep and surface waters in the subarctic Nordic seas over the last 30,000 yr., Quaternary Science Reviews, vol. 20, no. 4, pp. 659-678.

17. Bauch, H.A., Kassens, H., Naidina, O.D., Kunz-Pirrung, M. and Thiede, J., 2001. Composition and flux of Holocene sediments on the eastern Laptev Sea shelf, Arctic Siberia. Quaternary Research, 55(3), pp.344-351.

18. Bé, A.W., Hemleben, C., Anderson, O.R., Spindler, M., Hacunda, J. and Tuntivate-Choy, S., 1977. Laboratory and field observations of living planktonic foraminifera. Micropaleontology, pp.155-179.

19. Birks, C.J. and Koç, N., 2002. A high-resolution diatom record of late-Quaternary sea-surface temperatures and oceanographic conditions from the eastern Norwegian Sea. Boreas, 31(4), pp.323-344.

20. Bond, G., Broecker, W., Johnsen, S., McManus, J., Labeyrie, L., Jouzel, J. and Bonani, G., 1993. Correlations between climate records from North Atlantic sediments and Greenland ice. Nature, 365(6442), pp.143-147.

21. Bondevik, S., Mangerud, J., Birks, H.H., Gulliksen, S. and Reimer, P., 2006. Changes in North Atlantic radiocarbon reservoir ages during the Allerød and Younger Dryas. Science, 312(5779), pp.1514-1517.

22. Bowman, S.G.E. 1990, 'Radiocarbon Dating', Interpreting the Past: Radiocarbon Dating, University of California Press, pp. 1-64.

23. Calvo, E., Grimalt, J. and Jansen, E., 2002. High resolution U37K sea surface temperature reconstruction in the Norwegian Sea during the Holocene. Quaternary Science Reviews, 21(12-13), pp.1385-1394.

24. Caralp, M.H., 1989. Abundance of *Bulimina exilis* and *Melonis barleeanum*: relationship to the quality of marine organic matter. Geo-Marine Letters, 9, pp.37-43.

25. Carmack, E., Polyakov, I., Padman, L., Fer, I., Hunke, E., Hutchings, J., ... & Yulin, A. 2015, 'Toward quantifying the increasing role of oceanic heat in sea ice loss in the new Arctic', Bulletin of the American Meteorological Society, vol. 96, no. 12, pp. 2079-2105.

26. Cedhagen, T., 1991. Retention of chloroplasts and bathymetric distribution in the sublittoral foraminifera *Nonionellina labradorica*. Ophelia, 33(1), pp.17-30.

27. Clark, P.U., Dyke, A.S., Shakun, J.D., Carlson, A.E., Clark, J., Wohlfarth, B., Mitrovica, J.X., Hostetler, S.W. and McCabe, A.M., 2009. The last glacial maximum. science, 325(5941), pp.710-714.

28. Cokelet, E.D., Tervalon, N. and Bellingham, J.G., 2008. Hydrography of the West Spitsbergen current, Svalbard branch: autumn 2001. Journal of Geophysical Research: Oceans, 113(C1).

29. Corliss, B.H., 1985. Microhabitats of benthic foraminifera within deep-sea sediments. Nature, 314(6010), pp.435-438.

30. Corliss, B.H., 1991. Morphology and microhabitat preferences of benthic foraminifera from the northwest Atlantic Ocean. Marine Micropaleontology, 17(3-4), pp.195-236.

31. Cottier, F.R., Nilsen, F., Inall, M.E., Gerland, S., Tverberg, V. and Svendsen, H., 2007. Wintertime warming of an Arctic shelf in response to large-scale atmospheric circulation. Geophysical Research Letters, 34(10).

32. Cottier, F.R., Nilsen, F., Skogseth, R., Tverberg, V., Skarðhamar, J. and Svendsen, H., 2010. Arctic fjords: a review of the oceanographic environment and dominant physical processes. Geological Society, London, Special Publications, 344(1), pp.35-50.

33. Dowdeswell, J.A., Ottesen, D., Evans, J., Cofaigh, C.Ó. and Anderson, J.B., 2008. Submarine glacial landforms and rates of ice-stream collapse. Geology, 36(10), pp.819-822.

34. Duplessy, J.C., Cortijo, E., Ivanova, E., Khusid, T., Labeyrie, L., Levitan, M., Murdmaa, I., & Paterne, M. (2005). Paleoceanography of the Barents Sea during the Holocene. Paleoceanography, 20(4).

35. Duplessy, J.C., Ivanova, E., Murdmaa, I., Paterne, M. and Labeyrie, L., 2001. Holocene paleoceanography of the northern Barents Sea and variations of the northward heat transport by the Atlantic Ocean. Boreas, 30(1), pp.2-16.

36. Ebbesen, H., Hald, M. and Eplet, T.H., 2007. Lateglacial and early Holocene climatic oscillations on the western Svalbard margin, European Arctic. Quaternary Science Reviews, 26(15-16), pp.1999-2011.

37. Eglinton, T.I., Eglinton, G., Dupont, L., Sholkovitz, E.R., Montluçon, D., & Reddy, C.M. (1997). Composition, age, and provenance of organic matter in NW African dust over the Atlantic Ocean. Geochemistry, Geophysics, Geosystems, 3(8), 1050.

38. Eiriksson, J., Bartels-Jonsdottir, H.B., Cage, A.G., Gudmundsdottir, E.R., Klitgaard-Kristensen, D., Marret, F., Rodrigues, T., Abrantes, F., Austin, W.E., Jiang, H. and Knudsen, K.L., 2006. Variability of the North Atlantic Current during the last 2000 years based on shelf bottom water and sea surface temperatures along an open ocean/shallow marine transect in western Europe. The Holocene, 16(7), pp.1017-1029.

39. Fairbanks, R.G., 1989. A 17,000-year glacio-eustatic sea level record: influence of glacial melting rates on the Younger Dryas event and deep-ocean circulation. Nature, 342(6250), pp.637-642.

40. Falk-Petersen, S., Hop, H., Budgell, W.P., Hegseth, E.N., Korsnes, R., Løyning, T.B., Ørbæk, J.B., Kawamura, T. and Shirasawa, K., 2000. Physical and ecological processes in the marginal ice zone of the northern Barents Sea during the summer melt period. Journal of Marine Systems, 27(1-3), pp.131-159.

41. Faure, G. and Mensing, T.M., 2005. Principles and applications (p. 897). John Wiley & Sons, Inc.

42. Feyling-Hanssen, R.W., 1972. The foraminifer Elphidium excavatum (Terquem) and its variant forms. Micropaleontology, pp.337-354.

43. Gerland, S. and Renner, A.H., 2007. Sea-ice mass-balance monitoring in an Arctic fjord. Annals of Glaciology, 46, pp.435-442.

44. Giraudeau, J., Grelaud, M., Solignac, S., Andrews, J.T., Moros, M. and Jansen, E., 2010. Millennial-scale variability in Atlantic water advection to the Nordic Seas derived from Holocene coccolith concentration records. Quaternary Science Reviews, 29(9-10), pp.1276-1287.

45. Grauel, A.L., Goudeau, M.L.S., De Lange, G.J. and Bernasconi, S.M., 2013. Climate of the past 2500 years in the Gulf of Taranto, central Mediterranean Sea: a high-resolution climate

reconstruction based on δ18O and δ13C of Globigerinoides ruber (white). The Holocene, 23(10), pp.1440-1446.

46. Gustafsson, M. and Nordberg, K., 2001. Living (stained) benthic foraminiferal response to primary production and hydrography in the deepest part of the Gullmar Fjord, Swedish West Coast, with comparisons to Hoglund's 1927 material. The Journal of Foraminiferal Research, 31(1), pp.2-11.

47. Hald, M. and Korsun, S., 1997. Distribution of modern benthic foraminifera from fjords of Svalbard, European Arctic. The Journal of Foraminiferal Research, 27(2), pp.101-122.

48. Hald, M. and Steinsund, P.I., 1996. Benthic foraminifera and carbonate dissolution in the surface sediments of the Barents and Kara Seas. Berichte zur Polarforschung, 212, pp.285-307

49. Hald, M. and Vorren, T.O., 1987. Foraminiferal stratigraphy and environment of Late Weichselian deposits on the continental shelf off Troms, northern Norway. Marine Micropaleontology, 12, pp.129-160.

50. Hald, M. and Vorren, T.O., 1987. Stable isotope stratigraphy and paleoceanography during the last deglaciation on the continental shelf off Troms, northern Norway. Paleoceanography, 2(6), pp.583-599.

51. HALD, M. and ASPELI, R., 1997. Rapid climatic shifts of the northern Norwegian Sea during the last deglaciation and the Holocene. Boreas, 26(1), pp.15-28.

52. Hald, M. and Korsun, S., 1997. Distribution of modern benthic foraminifera from fjords of Svalbard, European Arctic. The Journal of Foraminiferal Research, 27(2), pp.101-122.

53. Hald, M., Andersson, C., Ebbesen, H., Jansen, E., Klitgaard-Kristensen, D., Risebrobakken, B., Salomonsen, G.R., Sarnthein, M., Sejrup, H.P. and Telford, R.J., 2007. Variations in

temperature and extent of Atlantic Water in the northern North Atlantic during the Holocene. Quaternary Science Reviews, 26(25-28), pp.3423-3440.

54. Hald, M., Ebbesen, H., Forwick, M., Godtliebsen, F., Khomenko, L., Korsun, S., Olsen, L.R. and Vorren, T.O., 2004. Holocene paleoceanography and glacial history of the West Spitsbergen area, Euro-Arctic margin. Quaternary Science Reviews, 23(20-22), pp.2075-2088.

55. Hald, M., Steinsund, P.I., Dokken, T., Korsun, S., Polyak, L. and Aspeli, R., 1994. Recent and Late Quaternary distribution of Elphidium excavatum f. clavatum in Arctic seas.

56. Hass, H.C., Kuhn, G., Forwick, M. and Vorren, T.O., 2008. The Medieval Warm Period and the Little Ice Age in marine sediments from Maxwell Bay, King George Island, West Antarctic Peninsula.

57. Heaton, T.J., Köhler, P., Butzin, M., Bard, E., Reimer, R.W., Austin, W.E., Ramsey, C.B., Grootes, P.M., Hughen, K.A., Kromer, B. and Reimer, P.J., 2020. Marine20—the marine radiocarbon age calibration curve (0–55,000 cal BP). Radiocarbon, 62(4), pp.779-820.

58. Helama, S., Jones, P.D. and Briffa, K.R., 2017. Dark Ages Cold Period: A literature review and directions for future research. The Holocene, 27(10), pp.1600-1606.

59. Hisdal, V., 1998. Svalbard: nature and history.

60. Holzhauser, H., Magny, M. and Zumbuühl, H.J., 2005. Glacier and lake-level variations in west-central Europe over the last 3500 years. The Holocene, 15(6), pp.789-801.

61. Hormes, A., Gjermundsen, E.F. and Rasmussen, T.L., 2013. From mountain top to the deep sea–Deglaciation in 4D of the northwestern Barents Sea ice sheet. Quaternary Science Reviews, 75, pp.78-99.

62. Humlum, O., Elberling, B., Hormes, A., Fjordheim, K., Hansen, O.H. and Heinemeier, J., 2005. Late-Holocene glacier growth in Svalbard, documented by subglacial relict vegetation and living soil microbes. The Holocene, 15(3), pp.396-407.

63. Jennings, A. E. and Helgadottir, G. (1994). Recent benthic foraminiferal assemblages in Disko Bugt, West Greenland. Journal of Foraminiferal Research, 24(2), 80-93.

64. Jennings, A.E., Weiner, N.J., Helgadottir, G. and Andrews, J.T., 2004. Modern foraminiferal faunas of the southwestern to northern Iceland shelf: oceanographic and environmental controls. The Journal of Foraminiferal Research, 34(3), pp.180-207.

65. Jennings, S., Warr, K.J. and Mackinson, S., 2002. Use of size-based production and stable isotope analyses to predict trophic transfer efficiencies and predator-prey body mass ratios in food webs. Marine Ecology Progress Series, 240, pp.11-20.

66. Johansen, S. and Hytteborn, H., 2001. A contribution to the discussion of biota dispersal with drift ice and driftwood in the North Atlantic. Journal of Biogeography, 28(1), pp.105-115.

67. Kinnard C, Zdanowicz C, Koerner R (2011) Reconstructed changes in Arctic Sea ice over the past 1,450 years. Nature 479(7374): 509-512.

68. Knudsen, K.L., Jiang, H., Jansen, E., Eirıksson, J., Heinemeier, J. and Seidenkrantz, M.S., 2004. Environmental changes off North Iceland during the deglaciation and the Holocene: foraminifera, diatoms and stable isotopes. Marine Micropaleontology, 50(3-4), pp.273-305.

69. Koç, N., Jansen, E. and Haflidason, H., 1993. Paleoceanographic reconstructions of surface ocean conditions in the Greenland, Iceland and Norwegian seas through the last 14 ka based on diatoms. Quaternary Science Reviews, 12(2), pp.115-140.

70. Koç, N., Jansen, E., & Haflidason, H. (2003). Paleoceanographic reconstructions of surface ocean conditions in the Greenland, Iceland and Norwegian seas through the last 14 ka based on diatoms. Quaternary Science Reviews, 22(5-7), 475-484.

71. Koç, N., Klitgaard-Kristensen, D., Hasle, K., Forsberg, C.F. and Solheim, A., 2002. Late glacial paleoceanography of Hinlopen Strait, northern Svalbard. Polar Research, 21(2), pp.307-314.

72. Korsun, S. and Hald, M., 1998. Modern benthic foraminifera off Novaya Zemlya tidewater glaciers, Russian Arctic. Arctic and Alpine Research, 30(1), pp.61-77.

73. Kristensen, D.K., Rasmussen, T.L. and Koç, N., 2013. Palaeoceanographic changes in the northern Barents Sea during the last 16 000 years–new constraints on the last deglaciation of the Svalbard–Barents Sea Ice Sheet. Boreas, 42(3), pp.798-813.

74. Kunz-Pirrung, M., Matthiessen, J. and de Vernal, A., 2001. Late Holocene dinoflagellate cysts as indicators for short-term climate variability in the eastern Laptev Sea (Arctic Ocean). Journal of Quaternary Science: Published for the Quaternary Research Association, 16(7), pp.711-716.

75. Łącka, M., Zajączkowski, M., Forwick, M. and Szczuciński, W., 2015. Late Weichselian and Holocene paleoceanography of Storfjordrenna, southern Svalbard. Climate of the Past, 11(3), pp.587-603.

76. Lekieffre, C., Geslin, E., Spangenberg, J. and Meibom, A., 2015. Feeding behavior of a benthic species (Ammonia tepida) under oxic and anoxic conditions: TEM-Nano SIMS correlation. In The Micropaleontological Society Foraminifera and Calcareous Nannofossil Groups Spring Meeting, June 2015, Plymouth University.

77. Lind, S. and Ingvaldsen, R.B., 2012. Variability and impacts of Atlantic Water entering the Barents Sea from the north. Deep Sea Research Part I: Oceanographic Research Papers, 62, pp.70-88.

78. Linke, P. and Lutze, G.F., 1993. Microhabitat preferences of benthic foraminifera—a static concept or a dynamic adaptation to optimize food acquisition? Marine micropaleontology, 20(3-4), pp.215-234.

79. Liu, Z., Otto-Bliesner, B.L., He, F., Brady, E.C., Tomas, R., Clark, P.U., Carlson, A.E., Lynch-Stieglitz, J., Curry, W., Brook, E. and Erickson, D., 2009. Transient simulation of last deglaciation with a new mechanism for Bølling-Allerød warming. science, 325(5938), pp.310-314.

80. Loubere, P., 1991. Deep-sea benthic foraminiferal assemblage response to a surface ocean productivity gradient: A test. Paleoceanography, 6(2), pp.193-204.

81. Lowe, D.J., 2015, May. Connecting and dating with tephras: principles, functioning, and application of tephrochronology in Quaternary research. In 12th Quaternary Techniques Short Course-Techniques of Paleoclimatic and Paleoenvironmental Reconstruction (pp. 1-30). National Isotope Centre, GNS Science.

82. Lubinski, D.J., Polyak, L. and Forman, S.L., 2001. Freshwater and Atlantic water inflows to the deep northern Barents and Kara seas since ca 13 14C ka: foraminifera and stable isotopes. Quaternary Science Reviews, 20(18), pp.1851-1879.

83. Lubinski, D.J., Korsun, S., Polyak, L., Forman, S.L., Lehman, S.J., Herlihy, F.A. and Miller, G.H., 1996. The last deglaciation of the Franz Victoria trough, northern Barents Sea. Boreas, 25(2), pp.89-100.

84. Mackensen, A. and Hald, M., 1988. Cassidulina teretis Tappan and C. laevigata d'Orbigny; their modern and late Quaternary distribution in northern seas. The Journal of Foraminiferal Research, 18(1), pp.16-24.

85. Mackensen, A., Hubberten, H.W., Bickert, T., Fischer, G. and Fütterer, D.K., 1993. The δ13C in benthic foraminiferal tests of Fontbotia wuellerstorfi (Schwager) relative to the δ13C of dissolved inorganic carbon in Southern Ocean deep water: implications for glacial ocean circulation models. Paleoceanography, 8(5), pp.587-610.

86. Mangerud, J. and Svendsen, J.I., 2018. The Holocene thermal maximum around Svalbard, Arctic North Atlantic; molluscs show early and exceptional warmth. The Holocene, 28(1), pp.65-83.

87. Mangerud, J., Astakhov, V. and Svendsen, J.I., 2002. The extent of the Barents–Kara ice sheet during the Last Glacial Maximum. Quaternary Science Reviews, 21(1-3), pp.111-119.

88. Mangerud, J., Bondevik, S., Gulliksen, S., Hufthammer, A. K., Kaland, P. E., Nesje, A., & Svendsen, J. I. (2004). Ice-dammed lakes and rerouting of the drainage of northern Eurasia during the Last Glaciation. Quaternary Science Reviews, 23(11-13), 1313-1332.

89. Mangerud, J., Bondevik, S., Gulliksen, S., Hufthammer, A.K. and Høisæter, T., 2006. Marine 14C reservoir ages for 19th century whales and molluscs from the North Atlantic. Quaternary Science Reviews, 25(23-24), pp.3228-3245.

90. Mann, M.E., Zhang, Z., Rutherford, S., Bradley, R.S., Hughes, M.K., Shindell, D., Ammann, C., Faluvegi, G. and Ni, F., 2009. Global signatures and dynamical origins of the Little Ice Age and Medieval Climate Anomaly. Science, 326(5957), pp.1256-1260.

91. Mayewski, P.A., Rohling, E.E., Stager, J.C., Karlén, W., Maasch, K.A., Meeker, L.D., Meyerson, E.A., Gasse, F., van Kreveld, S., Holmgren, K. and Lee-Thorp, J., 2004. Holocene climate variability. Quaternary research, 62(3), pp.243-255.

92. McCave, I.N., Hall, I.R. and Bianchi, G.G., 2006. Laser vs. settling velocity differences in silt grainsize measurements: estimation of paleocurrent vigour. Sedimentology, 53(4), pp.919-928.

93. McCave, I.N., Manighetti, B. and Robinson, S.G., 1995. Sortable silt and fine sediment size/composition slicing: parameters for paleocurrent speed and paleoceanography. Paleoceanography, 10(3), pp.593-610.

94. McCave, I.N. and Andrews, J.T., 2019. Distinguishing current effects in sediments delivered to the ocean by ice. I. Principles, methods and examples. Quaternary Science Reviews, 212, pp.92-107.

95. Menze, S., Ingvaldsen, R.B., Nikolopoulos, A., Hattermann, T., Albretsen, J. and Gjøsæter, H., 2020. Productive detours–Atlantic water inflow and acoustic backscatter in the major troughs along the Svalbard shelf. Progress in Oceanography, 188, p.102447.

96. Migeon, S., Weber, O., Faugeres, J.C. and Saint-Paul, J., 1998. SCOPIX: a new X-ray imaging system for core analysis. Geo-Marine Letters, 18, pp.251-255.

97. Miller, G.H., Geirsdóttir, Á., Zhong, Y., Larsen, D.J., Otto-Bliesner, B.L., Holland, M.M., Bailey, D.A., Refsnider, K.A., Lehman, S.J., Southon, J.R. and Anderson, C., 2012. Abrupt onset of the Little Ice Age triggered by volcanism and sustained by sea-ice/ocean feedbacks. Geophysical research letters, 39(2). Murray, J.W., 2001. The niche of benthic foraminifera, critical thresholds and proxies. Marine Micropaleontology, 41(1-2), pp.1-7.

98. Murray, J.W., 2001. The niche of benthic foraminifera, critical thresholds and proxies. Marine Micropaleontology, 41(1-2), pp.1-7.

99. Murray, J.W., 2006. Ecology and applications of benthic foraminifera. Cambridge university press.

100. Nesje, A., Bakke, J., Dahl, S.O., Lie, Ø. and Matthews, J.A., 2008. Norwegian mountain glaciers in the past, present and future. Global and Planetary Change, 60(1-2), pp.10-27.

101. Nilsen, F., Lunde, J.V. and Skogseth, R., Topographically Controlled Flow on the West Spitsbergen Shelf.

102. Oliver, K., Hoogakker, B., Crowhurst, S., Henderson, G., Rickaby, R., Edwards, N. and Elderfield, H., 2009. A synthesis of marine sediment core $\delta^{13}C$ data over the last 150 000 years. Climate of the Past Discussions, 5(6).

103. Ottesen, D., Dowdeswell, J.A. and Rise, L., 2005. Submarine landforms and the reconstruction of fast-flowing ice streams within a large Quaternary ice sheet: The 2500-km-long Norwegian-Svalbard margin (57–80 N). Geological Society of America Bulletin, 117(7-8), pp.1033-1050.

104. Piepjohn, K., von Gosen, W., Tessensohn, F., Reinhardt, L., McClelland, W.C., Dallmann, W., Gaedicke, C. and Harrison, J.C., 2015. Tectonic map of the Ellesmerian and

Eurekan deformation belts on Svalbard, north Greenland, and the Queen Elizabeth Islands (Canadian Arctic). arktos, 1, pp.1-7.

105. Polyak, L. and Mikhailov, V., 1996. Post-glacial environments of the southeastern Barents Sea: foraminiferal evidence. Geological Society, London, Special Publications, 111(1), pp.323-337.

106. Polyak, L. and Solheim, A., 1995. Late-and postglacial environments in the northern Barents Sea west of Franz Josef Land. Oceanographic Literature Review, 8(42), p.651.

107. Polyak, L., Alley, R.B., Andrews, J.T., Brigham-Grette, J., Cronin, T.M., Darby, D.A., Dyke, A.S., Fitzpatrick, J.J., Funder, S., Holland, M. and Jennings, A.E., 2010. History of sea ice in the Arctic. Quaternary Science Reviews, 29(15-16), pp.1757-1778.

108. Polyak, L., Curry, W.B., Darby, D.A., Bischof, J. and Cronin, T.M., 2004. Contrasting glacial/interglacial regimes in the western Arctic Ocean as exemplified by a sedimentary record from the Mendeleev Ridge. Palaeogeography, Palaeoclimatology, Paleoecology, 203(1-2), pp.73-93.

109. Polyak, L., Gataullin, V., Gainanov, V., Gladysh, V. and Goremykin, Y., 2002. Kara Sea expedition yields insight into extent of LGM ice sheet. Eos, Transactions American Geophysical Union, 83(46), pp.525-529.

110. Polyak, L., Korsun, S., Febo, L.A., Stanovoy, V., Khusid, T., Hald, M., Paulsen, B.E. and Lubinski, D.J., 2002. Benthic foraminiferal assemblages from the southern Kara Sea, a river-influenced Arctic marine environment. The Journal of Foraminiferal Research, 32(3), pp.252-273.

111. Polyak, L., Levitan, M., Khusid, T., Merklin, L. and Mukhina, V., 2002. Variations in the influence of riverine discharge on the Kara Sea during the last deglaciation and the Holocene. Global and Planetary Change, 32(4), pp.291-309.

112. Popp, B.N., Laws, E.A., Bidigare, R.R., Dore, J.E., Hanson, K.L. and Wakeham, S.G., 1998. Effect of phytoplankton cell geometry on carbon isotopic fractionation. Geochimica et Cosmochimica acta, 62(1), pp.69-77.

113. Rasmussen, T.L., Forwick, M. and Mackensen, A., 2012. Reconstruction of inflow of Atlantic Water to Isfjorden, Svalbard during the Holocene: Correlation to climate and seasonality. Marine Micropaleontology, 94, pp.80-90.

114. Rasmussen, T. L., Thomsen, E., Ślubowska, M. A., Jessen, S., Solheim, A., & Koç, N. (2014). Spatial and temporal distribution of Holocene temperature maxima in the northern Nordic seas: interplay of Atlantic-, Arctic- and polar water masses. Quaternary Science Reviews, 92, 280-291.

115. Rasmussen, T.L. and Thomsen, E., 2014. Brine formation in relation to climate changes and ice retreat during the last 15,000 years in Storfjorden, Svalbard, 76–78 N. Paleoceanography, 29(10), pp.911-929.

116. Rasmussen, T.L. and Thomsen, E., 2014. Brine formation in relation to climate changes and ice retreat during the last 15,000 years in Storfjorden, Svalbard, 76–78 N. Paleoceanography, 29(10), pp.911-929.

117. Rasmussen, T.L. and Thomsen, E., 2015. Palaeoceanographic development in Storfjorden, Svalbard, during the deglaciation and Holocene: evidence from benthic foraminiferal records. Boreas, 44(1), pp.24-44.

118. Rasmussen, T.L., Thomsen, E., Ślubowska, M.A., Jessen, S., Solheim, A. and Koç, N., 2007. Paleoceanographic evolution of the SW Svalbard margin (76 N) since 20,000 14C yr. BP. Quaternary Research, 67(1), pp.100-114.

119. Rathburn, A.E. and Corliss, B.H., 1994. The ecology of living (stained) deep-sea benthic foraminifera from the Sulu Sea. Paleoceanography, 9(1), pp.87-150.

120. Rau, G.H., Riebesell, U. and Wolf-Gladrow, D., 1996. A model of photosynthetic 13C fractionation by marine phytoplankton based on diffusive molecular CO2 uptake. Marine Ecology Progress Series, 133, pp.275-285.

121. Rebesco, M., Liu, Y., Camerlenghi, A., Winsborrow, M.C., Laberg, J., Caburlotto, A., Diviacco, P., Accettella, D., Sauli, C. and Wardell, N., 2010, December. Deglaciation of the Western Margin of the Barents Sea Ice Sheet-a Swath Bathymetric and Sub-Bottom Seismic Study from Eglacom Nice-Streams Data in the Kveithola Trough. In AGU Fall Meeting Abstracts (Vol. 2010, pp. C43C-0565).

122. Renssen, H., Seppä, H., Crosta, X., Goosse, H. and Roche, D.M., 2012. Global characterization of the Holocene thermal maximum. Quaternary Science Reviews, 48, pp.7-19.

123. Risebrobakken, B., Jansen, E., Andersson, C., Mjelde, E. and Hevrøy, K., 2003. A high-resolution study of Holocene paleoclimatic and paleoceanographic changes in the Nordic Seas. Paleoceanography, 18(1).

124. Risebrobakken, B., Dokken, T., Smedsrud, L.H., Andersson, C., Jansen, E., Moros, M. and Ivanova, E.V., 2011. Early Holocene temperature variability in the Nordic Seas: The role of oceanic heat advection versus changes in orbital forcing. Paleoceanography, 26(4).

125. Risebrobakken, B., Moros, M., Ivanova, E.V., Chistyakova, N. and Rosenberg, R., 2010. Climate and oceanographic variability in the SW Barents Sea during the Holocene. The Holocene, 20(4), pp.609-621.

126. Rosoff, D.B. and Corliss, B.H., 1992. An analysis of Recent deep-sea benthic foraminiferal morphotypes from the Norwegian and Greenland seas. Palaeogeography, Palaeoclimatology, Paleoecology, 91(1-2), pp.13-20.

127. Rudels, B., Korhonen, M., Schauer, U., Pisarev, S., Rabe, B. and Wisotzki, A., 2015. Circulation and transformation of Atlantic water in the Eurasian Basin and the contribution

of the Fram Strait inflow branch to the Arctic Ocean heat budget. Progress in Oceanography, 132, pp.128-152.

128. Saher, M., Kristensen, D.K., Hald, M., Pavlova, O. and Jørgensen, L.L., 2012. Changes in distribution of calcareous benthic foraminifera in the central Barents Sea between the periods 1965–1992 and 2005–2006. Global and Planetary Change, 98, pp.81-96.

129. Sakshaug, E. and Skjoldal, H.R., 1989. Life at the ice edge. Ambio (Sweden).

130. Sarnthein, M., Gebhardt, H., Kiefer, T., Kucera, M., Cook, M. and Erlenkeuser, H., 2004. Mid Holocene origin of the sea-surface salinity low in the subarctic North Pacific. Quaternary Science Reviews, 23(20-22), pp.2089-2099.

131. Sarnthein, M., Van Kreveld, S., Erlenkeuser, H., Grootes, P.M., Kucera, M., Pflaumann, U. and Schulz, M., 2003. Centennial-to-millennial-scale periodicities of Holocene climate and sediment injections off the western Barents shelf, 75 N. Boreas, 32(3), pp.447-461.

132. Schauer, U., Loeng, H., Rudels, B., Ozhigin, V.K. and Dieck, W., 2002. Atlantic water flow through the Barents and Kara Seas. Deep Sea Research Part I: Oceanographic Research Papers, 49(12), pp.2281-2298.

133. Sejrup, H.P., Birks, H.J.B., Kristensen, D.K. and Madsen, H., 2004. Benthonic foraminiferal distributions and quantitative transfer functions for the northwest European continental margin. Marine Micropaleontology, 53(1-2), pp.197-226.

134. Shackleton, N., 1967. Oxygen isotope analyses and Pleistocene temperatures re-assessed. Nature, 215(5096), pp.15-17.

135. Siddall, M., Rohling, E.J., Almogi-Labin, A., Hemleben, C., Meischner, D., Schmelzer, I. and Smeed, D.A., 2003. Sea-level fluctuations during the last glacial cycle. Nature, 423(6942), pp.853-858.

136. Skagseth, Ø., Furevik, T., Ingvaldsen, R., Loeng, H., Mork, K.A., Orvik, K.A. and Ozhigin, V., 2008. Volume and heat transports to the Arctic Ocean via the Norwegian and Barents Seas. Arctic–Subarctic Ocean fluxes: defining the role of the northern seas in climate, pp.45-64.

137. Skirbekk, K., Kristensen, D.K., Rasmussen, T.L., Koç, N. and Forwick, M., 2010. Holocene climate variations at the entrance to a warm Arctic fjord: evidence from Kongsfjorden trough, Svalbard. Geological Society, London, Special Publications, 344(1), pp.289-304.

138. Ślubowska-Woldengen, M., Koç, N., Rasmussen, T.L., Klitgaard-Kristensen, D., Hald, M. and Jennings, A.E., 2008. Time-slice reconstructions of ocean circulation changes on the continental shelf in the Nordic and Barents Seas during the last 16,000 cal yr BP. Quaternary Science Reviews, 27(15-16), pp.1476-1492.

139. Ślubowska-Woldengen, M., Rasmussen, T.L., Koç, N., Klitgaard-Kristensen, D., Nilsen, F. and Solheim, A., 2007. Advection of Atlantic Water to the western and northern Svalbard shelf since 17,500 cal yr. BP. Quaternary Science Reviews, 26(3-4), pp.463-478.

140. Ślubowska, M.A., Koç, N., Rasmussen, T.L. and Klitgaard-Kristensen, D., 2005. Changes in the flow of Atlantic water into the Arctic Ocean since the last deglaciation: evidence from the northern Svalbard continental margin, 80 N. Paleoceanography, 20(4).

141. Solignac, S., de Vernal, A. and Hillaire-Marcel, C., 2004. Holocene sea-surface conditions in the North Atlantic—contrasted trends and regimes in the western and eastern sectors (Labrador Sea vs. Iceland Basin). Quaternary Science Reviews, 23(3-4), pp.319-334.

142. Spielhagen, R.F. and Erlenkeuser, H., 1994. Stable oxygen and carbon isotopes in planktic foraminifers from Arctic Ocean surface sediments: Reflection of the low salinity surface water layer. Marine Geology, 119(3-4), pp.227-250.

143. Steinsund, P.I. and Hald, M., 1994. Recent calcium carbonate dissolution in the Barents Sea: Paleoceanographic applications. Marine geology, 117(1-4), pp.303-316.

144. Sternal, B., Szczuciński, W., Forwick, M., Zajączkowski, M., Lorenc, S. and Przytarska, J., 2014. Postglacial variability in near-bottom current speed on the continental shelf off south-west Spitsbergen. Journal of Quaternary Science, 29(8), pp.767-777.

145. Stuiver, M., Pearson, G.W. and Braziunas, T., 1986. Radiocarbon age calibration of marine samples back to 9000 cal yr. BP. Radiocarbon, 28(2B), pp.980-1021.

146. Svendsen, H., Beszczynska-Møller, A., Hagen, J.O., Lefauconnier, B., Tverberg, V., Gerland, S., Børre Ørbæk, J., Bischof, K., Papucci, C., Zajaczkowski, M. and Azzolini, R., 2002. The physical environment of Kongsfjorden–Krossfjorden, an Arctic fjord system in Svalbard. Polar research, 21(1), pp.133-166.

147. Svendsen, J. I., Alexanderson, H., Astakhov, V. I., Demidov, I., Dowdeswell, J. A., Funder, S., ... & Siegert, M. J. (2004). Late Quaternary ice sheet history of northern Eurasia. Quaternary Science Reviews, 23(11-13), 1229-1271.

148. Svendsen, J.I. and Mangerud, J., 1997. Holocene glacial and climatic variations on Spitsbergen, Svalbard. The Holocene, 7(1), pp.45-57.

149. Sztybor, K. and Rasmussen, T.L., 2017. Diagenetic disturbances of marine sedimentary records from methane-influenced environments in the Fram Strait as indications of variation in seep intensity during the last 35 000 years. Boreas, 46(2), pp.212-228.

150. Ternois, Y., Kawamura, K., Ohkouchi, N. and Keigwin, L., 2000. Alkenone sea surface temperature in the Okhotsk Sea for the last 15 kyr. Geochemical Journal, 34(4), pp.283-293.

151. Thomas, E., Booth, L., Maslin, M. and Shackleton, N.J., 1996. Northeastern Atlantic benthic foraminifera during the last 45 000 years: changes in productivity seen from the bottom up. Oceanographic Literature Review, 1(43), p.46.

152. Thornalley, D.J., Elderfield, H. and McCave, I.N., 2010. Intermediate and Deepwater paleoceanography of the northern North Atlantic over the past 21,000 years. Paleoceanography, 25(1).

153. Tverberg, V. and Nøst, O.A., 2009. Eddy overturning across a shelf edge front: Kongsfjorden, west Spitsbergen. Journal of Geophysical Research: Oceans, 114(C4).

154. Vinje, T.E., 1977. Sea ice conditions in the European sector of the marginal seas of the Arctic, 1966–1975. Arbok Nor Polarinst (1975), pp.163-174.

155. Vorren, T.O., Landvik, J.Y., Andreassen, K. and Laberg, J.S., 2011. Glacial history of the Barents Sea region. In Developments in Quaternary Sciences (Vol. 15, pp. 361-372). Elsevier.

156. Vorren, T.O., Vorren, K.D., ALM, T., Gulliksen, S. and Løvlie, R., 1988. The last deglaciation (20,000 to 11,000 BP) on Andoya, northern Norway. Boreas, 17(1), pp.41-77.

157. Walker, M., Johnsen, S., Rasmussen, S.O., Popp, T., Steffensen, J.P., Gibbard, P., Hoek, W., Lowe, J., Andrews, J., Björck, S. and Cwynar, L.C., 2009. Formal definition and dating of the GSSP (Global Stratotype Section and Point) for the base of the Holocene using the Greenland NGRIP ice core and selected auxiliary records. Journal of Quaternary Science: Published for the Quaternary Research Association, 24(1), pp.3-17.

158. Werner, K., Spielhagen, R.F., Bauch, D., Hass, H.C. and Kandiano, E., 2013. Atlantic Water advection versus sea-ice advances in the eastern Fram Strait during the last 9 ka: Multiproxy evidence for a two-phase Holocene. Paleoceanography, 28(2), pp.283-295.

159. Wollenburg, J.E. and Mackensen, A., 1998. Living benthic foraminifers from the central Arctic Ocean: faunal composition, standing stock and diversity. Marine Micropaleontology, 34(3-4), pp.153-185.a

160. Zajączkowski, M., Szczuciński, W., Plessen, B. and Jernas, P., 2010. Benthic foraminifera in Hornsund, Svalbard: Implications for paleoenvironmental reconstructions. Polish Polar Research, pp.349-375.

8. References

9. Appendix

Column1	Column2	Column3	Column4	Column5	Column6	Column7	Column8	Column9	Column10
Depth (cm)	Wet sediment weight	Dry sediment weight	Water weight	Water content %	Sediment Porosity	Wet Bulk Density	Dry Bulk Density	LSR	MAR
0,5	50,62	30,65	14,12	27,894113	0,359589477	1,289123182	0,929533705	70,27	65,31833346
10,5	58,4	36,5	22,33	38,23630137	0,568670894	1,487253928	0,918583034	70,27	64,54882981
20,5	58,87	36,07	11,33	19,24579582	0,288537449	1,499223266	1,210685818	70,27	85,0748924
30,5	81,16	47,54	45,42	55,96352883	1,156696463	2,066875493	0,910179031	70,27	63,95828049
40,5	57,87	35,74	26,68	46,10333506	0,679450938	1,47375659	0,794305651	70,27	55,8158581
50,5	50,17	31,19	26,64	53,09946183	0,678432271	1,277663178	0,599230906	70,27	42,10795579
60,5	39,34	23,53	9,63	24,47890188	0,245244098	1,001859067	0,756614969	70,27	53,16733389
70,5	50,03	29,71	22,98	45,93244054	0,585224234	1,274097843	0,688873609	70,27	48,4071485
80,5	45,74	27,05	7,26	15,87232182	0,184888074	1,164845799	0,979957725	70,27	68,86162936
90,5	66,24	38,48	40,7	61,44323671	1,036493748	1,686912675	0,650418927	67,08	43,63010161
100,5	43,05	25,54	19,38	45,0174216	0,493544197	1,096340439	0,602796241	67,08	40,43557185
110,5	39,74	23,67	10,6	26,67337695	0,269946775	1,012045738	0,742098964	67,08	49,77999847
120,5	51,08	29,14	23,83	46,6523101	0,606870909	1,300837854	0,693966944	67,08	46,55130262
130,5	46,21	27,25	13,74	29,73382385	0,34991214	1,176815137	0,826902997	67,08	55,46865307
140,5	54	32,47	23,31	43,16666667	0,593628237	1,37520055	0,781572313	67,08	52,42787073
150,5	50,74	30,69	22,9	45,13204572	0,5831869	1,292179184	0,708992284	67,08	47,55920238
160,5	47,4	27,84	17,45	36,81434599	0,444393511	1,207120483	0,762726972	67,08	51,16372527
170,5	49,38	29,95	16,58	33,5763467	0,422237502	1,257544503	0,835307001	67,08	56,03239361
180,5	56,46	32,8	14,94	26,46121148	0,380472152	1,437848575	1,057376423	67,08	70,92881045
190,5	68,38	41,52	33,99	49,70751682	0,865612346	1,741411363	0,875799017	67,08	58,74859806
200,5	56,43	34,39	26,78	47,4570264	0,681997606	1,437084575	0,755086969	67,08	50,65123386
210,5	50,59	29,65	15,44	30,51986559	0,393205491	1,288359182	0,895153691	67,08	60,04690962
220,5	57,87	35,15	24,38	42,12890963	0,620877582	1,47375659	0,852879008	67,08	57,21112384
230,5	55,97	33,49	17,73	31,67768447	0,451524181	1,425369903	0,973845723	67,08	65,32557109
240,5	64,31	38,24	32,12	49,94557612	0,817989661	1,637761988	0,819772328	67,08	54,99032776
250,5	53,87	32,19	23,62	43,84629664	0,601522907	1,371889882	0,770366975	67,08	51,67621667
260,5	50,64	30,25	21,65	42,75276461	0,551353554	1,289632516	0,738278962	67,08	49,52375277
270,5	47,76	28,99	7,91	16,56197655	0,201441414	1,216288487	1,014847073	67,08	68,07594163
280,5	62,97	39,85	20,71	32,88867715	0,527414878	1,603636641	1,076221764	67,08	72,19295592
290,5	66,8	42,26	28,86	43,20359281	0,734968294	1,701174014	0,96620572	67,08	64,81307969
300,5	61,48	37,94	22,35	36,35328562	0,569180228	1,565691293	0,996511065	67,08	66,84596226
310,5	61,92	39,13	18	29,06976744	0,458400183	1,576896631	1,118496447	67,08	75,02874169
320,5	71,05	43,92	29,04	40,87262491	0,739552296	1,80940739	1,069855095	67,08	71,76587975
330,5	66,54	42,01	31,61	47,50525999	0,805001655	1,694552678	0,889551022	67,08	59,67108259
340,5	56,19	34,93	19,99	35,57572522	0,50907887	1,430972572	0,921893702	67,08	61,84062954
350,5	58,79	36,2	20,93	35,60129274	0,533017547	1,497185932	0,964168386	67,08	64,67641531
360,5	60,64	37,86	19,53	32,20646438	0,497364199	1,544299284	1,046935085	67,08	70,22840553
370,5	66,44	41,11	32,79	49,35279952	0,835052334	1,69200601	0,856953676	67,08	57,48445259
380,5	53,16	33,65	15,44	29,04439428	0,393205491	1,353808542	0,960603051	67,08	64,43725265
390,5	60,07	37,72	16,95	28,21708007	0,431660173	1,529783279	1,098123106	67,08	73,66209794
400,5	67,71	43,12	24,74	36,53817752	0,630045585	1,72434869	1,094303104	67,08	73,40585224
410,5	67,53	42,97	28,08	41,58151932	0,715104286	1,719764688	1,004660402	67,08	67,39261976
420,5	61,63	39,45	19,26	31,25101412	0,490488196	1,569511294	1,079023098	67,08	72,38086943
430,5	66,48	42,37	25,05	37,68050542	0,637940255	1,693024677	1,055084422	67,08	70,77506303
440,5	61,98	41,43	22,65	36,54404647	0,576820231	1,578424631	1,001604401	67,08	67,1876232
450,5	60,86	39,33	23,59	38,76109103	0,600758907	1,549901953	0,949143046	67,08	63,66851555
460,5	57,24	37,27	15,63	27,30607966	0,398044159	1,457712583	1,059668424	67,08	71,08255787
470,5	64,79	41,61	18,55	28,63096157	0,472406856	1,649985993	1,177579138	67,08	78,99200856
480,5	71,95	46,24	34,68	48,20013899	0,883184353	1,8323274	0,949143046	67,08	63,66851555
490,5	58,31	37,27	19,43	33,32190019	0,494817531	1,484961927	0,990144396	67,08	66,41888609
500,5	58,67	38,88	8,41	14,33441282	0,214174752	1,494129931	1,279955179	67,08	85,85939338
510,5	67,54	50,26	17,28	25,58483861	0,440064176	1,720019355	1,279955179	67,08	85,85939338

Table 1: Sedimentological characterization data

Column11	Column12	Column13	Column14	Column15	Column16	Column17	Column18	Column19
63-100 residue weight	100-500 residue weight	>500 residue weight	%10-63	%<63	%63-100	%100-500	%>500	age
0,866	0,415	2,486	44,152	94,3	2,825448613	1,353996737	8,110929853	0
1,353	0,433	0,257	39,476	93,543	3,706849315	1,18630137	0,704109589	143
0,72	1,067	0,872	40,364	94,976	1,996118658	2,958136956	2,417521486	286
0,876	1,055	0,548	36,708	96,346	1,842658814	2,219183845	1,152713504	429
0,675	0,429	0,154	47,422	93,754	1,888640179	1,200335758	0,430889759	603,6525
0,873	0,338	0,0177	45,51	94,649	2,79897403	1,083680667	0,056748958	715
1,604	0,259	0,149	45,431	93,794	6,816829579	1,100722482	0,633234169	858
1,351	0,514	0,976	45,093	94,108	4,547290475	1,73005722	3,285089196	1009,419
2,0184	0,602	0,438	42,549	95,273	7,461737523	2,225508318	1,61922366	1144
2,785	0,625	0,058	42,015	94,49	7,237525988	1,624220374	0,150727651	1348,9025
0,408	0,302	0,075	41,268	93,431	1,597494127	1,182458888	0,293657009	1430
1,193	0,26	0,012	43,713	93,873	5,040135192	1,09843684	0,050697085	1647,0025
0,527	0,216	0,015	46,06	96,095	1,808510638	0,741249142	0,051475635	1796,0525
1,183	0,944	0,013	45,936	94,439	4,341284404	3,464220183	0,047706422	1859
0,77	0,259	0,288	42,716	94,624	2,371419772	0,797659378	0,88697259	2094,1525
1,548	0,313	0,059	40,339	94,644	5,04398827	1,019876181	0,192245031	2243,2025
0,991	0,792	0,014	42,776	92,666	3,559626437	2,844827586	0,050287356	2386
0,932	0,503	0,015	45,746	93,202	3,111853088	1,679465776	0,050083472	2529
0,686	0,191	0,032	52,883	92,942	2,091463415	0,582317073	0,097560976	2690
1,175	0,399	0,216	49,609	93,383	2,829961464	0,960982659	0,520231214	2839
0,634	0,547	0,019	51,75	94,163	1,843559174	1,590578657	0,055248619	2988
0,512	0,247	0,006	50,711	93,628	1,726812816	0,833052277	0,020236088	3137
0,879	0,529	0,022	51,45	93,666	2,500711238	1,504978663	0,062588905	3286
0,99	0,256	0,031	52,18	94,722	2,9561063	0,764407286	0,092564945	3435
0,803	0,546	0,105	45,1	94,278	2,099895397	1,427824268	0,27458159	3584
0,512	0,191	0,006	51,437	93,33	1,590556073	0,593351973	0,018639329	3733
0,715	0,134	0,021	49,311	92,965	2,363636364	0,442975207	0,069421488	3882
1,275	0,311	0,007	48,763	93,342	4,398068299	1,072783719	0,024146257	4031
1,278	0,278	1,848	44,949	93,994	3,207026349	0,69761606	4,637390213	4180
1,806	0,287	0,218	46,686	92,056	4,273544723	0,6791292	0,515854236	4329
0,646	0,217	0,003	46,44	95,359	1,702688455	0,57195572	0,007907222	4478
0,88	0,524	0,012	50,954	88,997	2,248913877	1,33912599	0,030667007	4628
1,236	0,582	0,018	41,431	94,406	2,81420765	1,325136612	0,040983607	4777
0,897	0,341	0,031	50,816	90,066	2,135205903	0,811711497	0,073791954	4926
0,498	0,219	0,313	49,79	92,629	1,42570856	0,626968222	0,89607787	5075
0,782	0,657	0,026	45,995	94,564	2,160220994	1,814917127	0,071823204	5224
0,771	0,448	0,019	50,926	85,546	2,036450079	1,18330692	0,050184892	5373
0,942	0,352	0,009	47,318	91,548	2,291413281	0,856239358	0,021892484	5522
0,692	0,209	0,014	42,367	95,812	2,056463596	0,621099554	0,041604755	5671
0,895	0,287	0,031	40,157	95,314	2,372746554	0,760869565	0,082184517	5820
1,301	0,707	0,025	41,966	94,3	3,01716141	1,63961039	0,057977737	5969
0,976	0,466	0,024	41,294	93,386	2,271352106	1,084477542	0,055852921	6118
1,319	0,531	0,014	42,426	94,237	3,34347275	1,346007605	0,035487959	6267
0,712	0,382	0,074	39,875	94,925	1,68043427	0,901581308	0,174651876	6362
1,296	0,976	1,817	51,875	91,238	3,128167994	2,355780835	4,385710838	6565
1,338	0,472	0,009	45,718	92,968	3,401983219	1,200101704	0,022883295	6714
1,897	0,42	0,009	45,722	92,267	5,089884626	1,126911725	0,024148108	6863
1,622	0,342	0,032	49,68	90,333	3,898101418	0,821917808	0,07690459	7012
1,345	0,398	0,048	48,454	92,523	2,908737024	0,860726644	0,103806228	7161
0,732	0,264	0,013	42,603	94,69	1,96404615	0,708344513	0,034880601	7310
1,785	0,869	0,076	40,914	93,197	4,591049383	2,235082305	0,195473251	7459
4,759	2,046	0,066	35,164	92,28	9,468762435	4,070831675	0,131317151	7554

Table 2: Grain size data

cm	IRD>500	IRD150-25	IRD250-50	Flux IRD >50	Flux IRD 250-5(	Flux IRD 150-2:
0,5	2,304	0,64	0,06	150,4934403	3,919100008	41,80373341
10,5	1,494	0,93	0,136	96,43595173	8,778640854	60,03041172
20,5	0,752	0,93	0,184	63,97631909	15,6537802	79,11964994
30,5	0,824	0,43	0,036	52,70162312	2,302498098	27,50206061
40,5	1,873	0,89	0,086	104,5431022	4,800163797	49,67611371
50,5	0,567	0,88	0,117	23,87521093	4,926630827	37,0550011
60,5	2,397	0,68	0,041	127,4420993	2,17986069	36,15378705
70,5	1,527	0,47	0,017	73,91771575	0,822921524	22,75135979
80,5	3,875	0,7	0,11	266,8388138	7,574779229	48,20314055
90,5	0,493	0,67	0,066	21,50964009	2,879586706	29,23216808
100,5	1,221	0,97	0,123	49,37183323	4,973575338	39,2225047
110,5	0,343	0,73	0,08	17,07453948	3,982399878	36,33939888
120,5	0,05	0,01	0	2,327565131	0	0,465513026
130,5	0,347	0,77	0,064	19,24762261	3,549993796	42,71086286
140,5	0,347	0,78	0,081	18,19247114	4,246657529	40,89373917
150,5	0,826	0,94	0,207	39,28390117	9,844754893	44,70565024
160,5	0,282	0,98	0,655	14,42817052	33,51224005	50,14045076
170,5	0,401	0,99	0,109	22,46898984	6,107530904	55,47206968
180,5	0,351	0,6	0,011	24,89601247	0,780216915	42,55728627
190,5	0,383	0,53	0,019	22,50071306	1,116223363	31,13675697
200,5	0,201	0,71	0,045	10,18089801	2,279305524	35,96237604
210,5	0,101	0,54	0,008	6,064737871	0,480375277	32,42533119
220,5	0,157	0,68	0,03	8,982146444	1,716333715	38,90356421
230,5	0,041	0,48	0,025	2,678348415	1,633139277	31,35627412
240,5	0,213	0,67	0,068	11,71293981	3,739342287	36,8435196
250,5	0,134	0,66	0,042	6,924613034	2,1704011	34,106303
260,5	0,099	1,19	0,149	4,902851524	7,379039163	58,9332658
270,5	0,156	0,65	0,112	10,61984689	7,624505463	44,24936206
280,5	0,196	0,5	0,064	14,14981936	4,620349179	36,09647796
290,5	0,122	0,89	0,084	7,907195722	5,444298694	57,68364092
300,5	0,14	0,53	0,026	9,358434716	1,737995019	35,42836
310,5	0,135	1,15	0,031	10,12888013	2,325890992	86,28305295
320,5	0,029	0,5	0,23	2,081210513	16,50615234	35,88293987
330,5	0,124	1,71	0,161	7,399214241	9,607044297	102,0375512
340,5	0,279	1,01	0,177	17,25353564	10,94579143	62,45903583
350,5	0	0,59	0,06	0	3,880584919	38,15908503
360,5	0,144	2,57	0,581	10,1128904	40,80270361	180,4870022
370,5	0,094	0,93	0,171	5,403538544	9,829841394	53,46054091
380,5	0,119	0,67	0,091	7,668033066	5,863789992	43,17295928
390,5	0,18	0,76	0,137	13,25917763	10,09170742	55,98319444
400,5	0,089	1	0,137	6,53312085	10,05660176	73,40585224
410,5	0,091	0,82	0,059	6,132728398	3,976164566	55,2619482
420,5	0,034	0,53	0,023	2,460949561	1,664759997	38,3618608
430,5	0,091	0,48	0,087	6,440530736	6,157430484	33,97203025
440,5	0,215	0,39	0,002	14,44533899	0,134375246	26,20317305
450,5	0,135	1,03	0,218	8,595249599	13,87973639	65,57857101
460,5	0,036	0,86	0,04	2,558972083	2,843302315	61,13099977
470,5	0,031	0,88	0,027	2,448752265	2,132784231	69,51296753
480,5	0,055	0,65	0,007	3,501768355	0,445679609	41,38453511
490,5	0,214	0,63	0,066	14,21364162	4,383646482	41,84389824
500,5	0,103	0,85	0,036	8,843517519	3,090938162	72,98048438
510,5	0,373	1,77	0,072	32,02555373	6,181876324	151,9711263

Table 3: IRD and flux of IRD data

Column1	Column2	Column3	Column4	Column5	Column6
Age	Depth	C13	dO18	dO18 correcti	BWT
0	0,5	-2,07	4	4	1,9
603,6525	20		4,13		1,9
1009,419	40	-2,09	4,07	4,13	1,81
1348,9025	70	-2,31	3,89	4,07	2,06
1647,0025	90	-2,19	4,01	3,89	2,78
1796,0525	110	-2,27	4	4,01	2,36
2094,1525	120	-2,23	4,17	4	1,9
2243,2025	140	-2,17	4,09	4,17	1,74
2690,3525	150	-2,17	4,07	4,09	1,97
2839,4025	180	-3,68	4,06	4,07	2,06
2988,4525	190	-2,19	3,99	4,06	2,11
3137,5025	200	-2,05	4,28	3,99	2,43
3286,5525	210	-2,16	4,056	4,28	1,12
3435,6025	220	-1,96	4,186	4,056	2,15
3584,6525	230	-2,7	4,206	4,186	1,67
3733,7025	240	-2,41	4,096	4,206	1,61
3882,7225	250	-2,51	4,155	4,096	1,97
4031,8025	260	-2,14	4,254	4,155	1,88
4180,8525	270	-2,05	4,2	4,254	1,29
4329,9025	280	-2,06	4,17	4,2	1,61
4478,9525	290	-1,74	4,05	4,17	1,74
4628,0025	300	-2,25	4,143	4,05	2,15
4777,0525	310	-1,77	5,372	4,143	1,85
5075,1525	320	-1,54	4,15		1,85
5224,2025	340	-1,55	4,13	4,15	1,88
5373,2525	350	-1,67	3,982	4,13	1,81
5671,3525	360	-1,92	4,05	3,982	2,5
5820,4025	380	-1,97	4,091	4,05	2,15
5969,4525	390	-2,32	4,041	4,091	1,97
6118,5025	400	-1,93	4,12	4,041	2,22
6267,5525	410	-2,14	4,23	4,12	1,85
6362,5	420	-2,48	4,27	4,23	1,4
6565,6525	430	-2,16	4,14	4,27	1,22
6714,7025	440	-2,33	4,1	4,14	1,85
6863,7525	450	-2,24	4,05	4,1	1,94
7012,8025	460	-2,08	4,1	4,05	2,15
7161,8525	470	-2,37	4,13	4,1	1,91
7310,9025	480	-2,43	4,01	4,13	1,81
7554,9	490	-2,34	4,16	4,01	2,36
7703	510	-1,92		4,16	1,61

Table 4: $\delta^{18}O$ data and $\delta^{18}O$ values after ice volume corrected, bottom water temperature (BWT), and $\delta^{13}C$ values.

Column1	Column2	Column3	Column4	Column5	Column6	Column7	Column8	Column9	Column10	Column11	Column12
Age	Depth cm	IRD 240	IRD 240 3pt	IRD516	%<63	%10-63	SS%	SSmean	3 pt ma	Correl 5	Correl 7
0	0,5	0,06	0,098	0	94,3	44,152	46,821	21,089	21,089	0,628900663	0,59433208
150,339	10,5	0,136	0,19	0	93,543	39,476	42,201	21,965	21,16733333	0,553273231	0,626223452
293,519	20,5	0,184	0,178	0	94,976	40,364	42,499	20,448	20,724	0,954605713	0,871824746
436,699	30,5	0,036	0,153	0	96,346	36,708	38,1	19,759	20,60566667	0,85692678	0,773070087
579,879	40,5	0,086	0,1195	0	93,754	47,422	50,582	21,61	20,72966667	0,624321146	-0,042061048
723,059	50,5	0,117	0,122	0	94,649	45,51	48,083	20,82	21,30766667	0,29535854	-0,068936644
866,239	60,5	0,041	0,0875	0	93,794	45,431	48,437	21,493	21,45966667	0,103894048	0,14628045
1009,419	70,5	0,017	0,084	0	94,108	45,093	47,916	22,066	21,37566667	0,372242538	0,128852599
1152,599	80,5	0,11	0,0965	0	95,273	42,549	44,66	20,568	21,41233333	0,254967985	0,095152403
1348,9025	90,5	0,066	0,1495	0	94,49	42,015	44,465	21,603	21,51666667	-0,386253678	0,171259635
1497,9525	100,5	0,123	0,1345	0	93,431	41,268	44,169	22,379	22,188	-0,352158465	0,101479838
1647,0025	110,5	0,08	0,1015	0	93,873	43,713	46,565	22,582	22,232	0,404617805	0,422710453
1796,0525	120,5	0	0,072	0	96,095	46,06	47,432	21,735	21,93066667	0,651040753	0,945730881
1945,1025	130,5	0,064	0,0725	0	94,439	45,936	48,641	21,475	21,518	0,773039101	0,952746902
2094,1525	140,5	0,081	0,176	0	94,624	42,716	45,143	21,344	21,328	0,967545681	0,893991978
2243,2025	150,5	0,207	0,4715	0	94,644	40,339	42,621	21,165	21,21433333	0,968293204	0,889172281
2392,2525	160,5	0,655	0,4855	0	92,666	42,776	46,162	21,134	21,39333333	0,867046639	0,874451497
2541,3025	170,5	0,109	0,3875	0	93,202	45,746	49,082	21,881	22,20566667	0,725317135	0,623757677
2690,3525	180,5	0,011	0,0695	0	92,942	52,883	56,898	23,602	22,81633333	0,446427968	0,416157753
2839,4025	190,5	0,019	0,0375	0	93,383	49,609	53,124	22,966	22,894	-0,757109684	0,106340544
2988,4525	200,5	0,045	0,036	0	94,163	51,75	54,957	22,114	22,61266667	0,148707997	0,165563908
3137,5025	210,5	0,008	0,0415	0	93,628	50,711	54,162	22,758	22,54666667	0,416173462	0,194796723
3286,5525	220,5	0,03	0,0315	0	93,666	51,45	54,929	22,768	22,584	0,383076006	0,223631778
3435,6025	230,5	0,025	0,0615	0	94,722	52,18	55,087	22,226	22,43633333	0,070317024	-0,031894412
3584,6525	240,5	0,068	0,0675	0	94,278	45,1	47,832	22,315	22,37433333	0,525743258	0,40604448
3733,7025	250,5	0,042	0,1295	0	93,33	51,437	55,112	22,582	22,506	-0,040641465	0,677278881
3882,7525	260,5	0,149	0,1515	0	92,965	49,311	53,042	22,621	22,739	0,517066496	0,844488837
4031,8025	270,5	0,112	0,1625	0	93,342	48,763	52,24	23,014	22,70366667	0,871183615	0,858157734
4180,8525	280,5	0,064	0,13	0	93,994	44,949	47,821	22,476	22,94833333	0,89359018	0,80447181
4329,9025	290,5	0,084	0,087	0	92,056	46,686	50,715	23,355	22,51666667	0,856889453	0,816565748
4478,9525	300,5	0,026	0,0705	0	95,359	46,44	48,7	21,716	23,087	0,876069748	0,91486374
4628,0025	310,5	0,031	0,1435	0	88,997	50,954	57,254	24,19	22,56733333	0,880068841	0,889860831
4777,0525	320,5	0,23	0,211	0,0001	94,406	41,431	43,886	21,796	23,07533333	0,905190984	0,898510988
4926,1025	330,5	0,161	0,284	0	90,066	50,816	56,421	23,24	22,526	0,876778859	0,955129199
5075,1525	340,5	0,177	0,199	0	92,629	49,79	53,753	22,542	22,517	0,954178553	0,95409083
5224,2025	350,5	0,06	0,409	0	94,564	45,995	48,639	21,769	22,97966667	0,976233815	0,906425355
5373,2525	360,5	0,581	0,406	0	85,546	50,926	59,53	24,628	23,23366667	0,974912076	0,899033469
5522,3025	370,5	0,171	0,4215	0	91,548	47,318	51,687	23,304	22,76433333	0,819566015	0,80416938
5671,3525	380,5	0,091	0,1995	0	95,812	42,367	44,218	20,361	21,395	0,560262598	0,805233991
5820,4025	390,5	0,137	0,1825	0	95,314	40,157	42,132	20,52	20,91	0,737925119	0,837587806
5969,4525	400,5	0,137	0,1665	0	94,3	41,966	46,821	21,849	21,57266667	0,878547048	0,777707413
6118,5025	410,5	0,059	0,1095	0	93,386	41,294	44,218	22,349	22,114	0,833466942	0,821747498
6267,5525	420,5	0,023	0,0845	0	94,237	42,426	45,02	22,144	21,81466667	0,888123786	0,82139263
6416,6025	430,5	0,087	0,056	0	94,925	39,875	42,006	20,951	22,18533333	0,92266084	0,897838457
6565,6525	440,5	0,002	0,1535	0	91,238	51,875	56,857	23,461	22,08733333	0,858238441	0,927719568
6714,7025	450,5	0,218	0,13	0	92,968	45,718	49,176	21,85	22,358	0,88976702	0,869135398
6863,7525	460,5	0,04	0,1425	0	92,267	45,722	49,554	21,763	22,54466667	0,910158971	0,8697761
7012,8025	470,5	0,027	0,037	0	90,333	49,68	54,761	24,021	22,57266667	0,877274603	0,879136039
7161,8525	480,5	0,007	0,05	0	92,523	48,454	52,369	21,934	22,287	0,947160442	0,899299188
7310,9025	490,5	0,066	0,0545	0	94,69	42,603	44,992	20,906	21,188	0,852987372	0,852987372
7459,9525	500,5	0,036	0,087	0	93,197	40,914	43,9	20,724	20,72333333		
7609,0025	510,5	0,072	0,054	0	92,28	35,164	38,123	20,54	20,54		
							correl SS-SS	0,81953761			
		0,101307692		1,92308E-06	93,48578846	45,46130769	48,72144231	22,00905769			
		IRD240		IRD516	%<63	%10-63	SS%	SSMean			

Table 5: The sortable silt parameters data.